An integrated micro bi-directional dosing system for single cell analysis on-chip
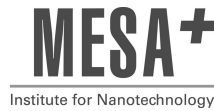
Jurjen Emmelkamp

Promotiecommissie

Voorzitter:	prof. dr. ir. A.J. Mouthaan	Universiteit Twente, EWI
Secretaris:	prof. dr. ir. A.J. Mouthaan	Universiteit Twente, EWI
Promotor:	prof. dr. ir. A. van den Berg	Universiteit Twente, EWI
Assistent promotor:	dr. E. T. Carlen	Universiteit Twente, EWI
Leden:	prof. dr. ir. S.M.H. Andersson-Svahn	KTH, RIT, Stockholm
	prof. dr. M.C. Elwenspoek	Universiteit Twente, EWI
	prof dr. ir. J.G.E. Gardeniers	Universiteit Twente, TNW
	dr. A.B. Fuchs	CEA, Biopuces, Grenoble
	dr. ir. A. Bossche	TU Delft, EI

Cover design: Steven Emmelkamp

An integrated micro bi-directional dosing system for single cell analysis on-chip

PROEFSCHRIFT

ter verkrijging van
de graad van doctor aan de Universiteit Twente,
op gezag van de rector magnificus,
prof. dr. W.H.M. Zijm,
volgens het besluit van het College voor Promoties
in het openbaar te verdedigen
op vrijdag 4 mei 2007 om 16.45 uur

door

Jurjen Emmelkamp

geboren op 21 juli 1975

te Drachten

Dit proefschrift is goedgekeurd door

de promotor: prof. dr. ir. A. van den Berg
de assistent promotor: Dr. ir. E.T. Carlen

Contents

Chapter 1

Introduction

This chapter gives an impression of the relevance of the work, described in this thesis, in the scientific field of biological cell research. More specifically, it emphasizes the importance and benefits of on-chip single-cell microinjection. Thereafter, the aims of the project are discussed and the outline of this thesis is given.

1.0.1 Scientific context

Research on single cells on chip is becoming increasingly popular. Electroporation of single trapped cells [1], viability research [2; 3], fluorescence based microfluidic cell sorters [4; 5], cell detection of non-labeled cells based on autofluorescence [6] or cell impedance [7], and cell manipulation [8] show the scientific interest in single cell research on chip. Currently, drug delivery is moving to smaller dimensions and increased sophistication, as demonstrated in implantable and closed-loop glucose-sensitive delivery systems [9].

The precise dosing of small volumes of solutions into a single cell or group of cells has applications ranging from in vitro cell fertilization to delivery of molecular moieties for pharmacological drug screening. These substances can be delivered to a cell and subsequent cell behavior is monitored. Substances that can be injected include, but are not limited to, RNA, DNA, antibodies, proteins, kinases and ions [10; 11; 12; 13]. Many non-viral techniques exist for intracellular delivery of substances to eukaryotic and prokaryotic cells, typically categorized as mechanical, electrical, or chemical [14]. Mechanical techniques include microinjection, pressure and particle bombardment. The most common electrical method is electroporation, using both high or low voltages. Chemical techniques include fusion [15], using DEAE-dextran, calcium phosphate, artificial lipids, proteins, dendimers, and other polymers including controlled-release polymers. Comparing the three categories of intracellular delivery based on toxicity effects to the cell and delivery efficiency, microinjection is reported as having the highest delivery efficiency and lowest toxicity effects [16]. Microin-

jection is not commonly used for studying large numbers of cells in a population because the process is slow, therefore, electroporation is commonly used for cell studies dealing with large amounts of cells. However, for studying single cells microinjection is clearly the best technique and is often used by cell biologists, sometimes referred to as "stab"microinjections, to manipulate the environment of a single cell [17].

Common to all microinjection systems is a pumping system, fluidic interconnects, and the injection tip that interfaces directly with the cell membrane and delivers the sample to the cytoplasm. Commercial systems are available and consist of integrated macroscale components and most commonly of a pulled glass pipette which penetrates the cell membrane. The PLI-100 Pico-Injector (Warner Instruments, Hamden, CT, USA) delivers volumes ranging from femtoliters for small cells to microliters for large egg cells, while simultaneously holding a cell. The sample injection is done using either pressure injection or iontophoresis. The FemtoJet express microinjector (Eppendorf AG, Hamburg, Germany) can inject liquids in the volume range from femtoliters to microliters using an external pressure source. Although these systems provide a basic capability for single cell dosing, there are clear advantages to integrating the pump, fluidic interconnects and injection tip on a single substrate using conventional microfabrication technology. The microfabricated dosing systems can significantly reduce the amount of sample reagents required for experimentation, which is extremely important when working with small amounts of proteins. Additionally, the lab-on-chip (LOC) technology has become commonplace and can easily be integrated with pumps and injection tips on a planar surface. Since the dimensions of the microfabricated systems are comparable to cellular dimensions this means that precise control and placement of single cells is possible.

The application of microsystem technology to cell biology research is intriguing and emerging as an important multidisciplinary research field to study many fundamental problems. The small, on the scale of microns, device dimensions of microsystems are ideally suited to interface with eukaryotic or prokaryotic cells. Scaling device dimensions down to the sub-micro, or even in the nanometer range, make it possible to probe, manipulate and measure properties of single cells. This multidisciplinary approach to biological research will be important for many branches of science and medical research.

1.0.2   Project description

In 2002 Prof. A. van den Berg received the Simon Stevin Master award from the Dutch Technology Foundation STW ('Stichting Technische Wetenschappen') for his research on Lab-on-a-Chip systems. This award was used to set up a new project for research for using nanochannels for performing Single Cell ANalysis (SCAN): NanoSCAN. The NanoSCAN project is done within the framework of

STW under project number TMM 6016.

The ultimate goal of this NanoSCAN-project is to develop an automated integrated micro bi-directional dosing system, or automated IMBID-system, suitable to transport various substances into or from single viable mammalian cells by means of an integrated hollow nanoneedle. Interaction between the dosing system and the researched cell should be minimized, which means that influence of the IMBID system on the cell has to be minimal and viability has to be maintained. Furthermore, the chemical compounds of the dosed sample should not be influenced by the dosing system.

To maintain cell viability, the dosing system should allow low pump rates and dosing volumes, and the needles should give low indentation depths of the cell membrane before penetration. We estimated that dosing volumes of 5% of the cell's volume, which equals approximately 25 fL for 10 μm diameter cells (V = 500 fL), maintains cell viability, as microinjection volumes of 30 fL for nuclei of human vascular smooth muscle cells are reported [18]. Furthermore, the indentation depth should be limited to 1 μm to minimize cell mortality.

This project mainly focuses on the development of a working IMBID system, operated by hand. Upstream of an automated IMBID system, sorting of cells on-chip is a near necessity. As the dosing system must be suitable for biochemical research, unwanted chemical interference of the dosing system on the researched cells should be avoided. Therefore, the use of non-labeled cells would be an added advantage, and the investigation of on-chip detection of cells based on their autofluorescence is a sub-goal in this project.

1.0.3 Outline

Chapter 2 describes a survey for achieving an IMBID system. The separate components of this system, nanoneedles, microfluidic network and micropump, are discussed. During this survey we come to a suggestion of which technique should be used for all three main aspects to achieve a working IMBID-system for intracellular mass transport.

Chapter 3 presents the theoretical aspects of electrochemical pumping in nanochannels. Due to extremely low currents and to the very small channel dimensions, charging capacitances, high capillary pressures and very limited diffusion are highly affecting the behavior of the electrochemical hydrogen bubble. The effect of hydraulic resistance on bubble growth in the nanochannel is briefly described.

Chapter 4 describes the design and fabrication of the IMBID system. The complete dosing system consists of an integrated free-hanging planar nanoneedle for fluid delivery, which directly is integrated with a small nanochannel network. The nanochannels contain the electrolyte and sample material used for actuation and dosing. In the micropump, electrodes are located at specific loca-

tions in the nanochannels, and ensure proper actuation and dosing operations by means of electrochemical generation of hydrogen gas.

Chapter 5 describes the characterization of the fabricated electrochemical femtoliter dosing system. After a short introduction the experimental set-up is described and data processing techniques explained. In the following sections the bubble nucleation position and time are compared to the theoretical expectations. The bubble growth experiments are divided into two parts: i) dc-measurements where constant bubble growth is characterized and, ii) pulsed bubble growth used for dosing small sample volumes. Dosing of volumes down to 16 fL are presented. For sample retraction an electrochemical back-reaction is used and described in the next section. The last experimental section demonstrates the concept of electrochemical sample dosing from the nanochannels to an external reservoir through the integrated nanoneedle tip.

Chapter 6 presents cell membrane penetration experiments, which have been performed with hollow nanoneedles integrated in a femtoliter dosing system and K562-cells. Successful penetration has been achieved, with low estimated indentation depth, necessary for low cell damage. Preliminary results based on optical inspection have not indicated severe cell damage within 30 minutes after penetration. Nanoneedle integrity was confirmed during all cell penetration experiments. Based on reported literature and preliminary results we expect to maintain cell viability.

Chapter 7 demonstrates the possibility of using the autofluorescence signal of the cells as a sorting criterion. The ultimate goal of the NanoSCAN-project is to develop an automated chip for single cell analysis. In this automated IMBID system detection and sorting of certain cells on chip is a sub-goal.

Finally, Chapter 8 gives a short summary of the results and conclusions of the preceding chapters. This summation will be completed by reflections given on the future of an integrated micro bi-directional dosing system, and important recommendations to achieve this future prospective.

Bibliography

[1] A. Valero, R. Luttge, J.W. van Nieuwkasteele, H. Andersson, and A. van den Berg. Flow-through microfluidic chip for cell transfection by electropermeabilization. In *μTAS2005*, pages 1395–1397, 2005.

[2] F. Wolbers, P. ter Braak, S. le Gac, H. Andersson, I. Vermes, and A. van den Berg. Viability study of hl60 cells in contact with commonly used microchip materials. *Electrophoresis*, 27:5073–5080, 2006.

[3] A. Valero, F. Merino, F. Wolbers, R. Luttge, I. Vermes, and A. van den Berg. Apoptotic cell death dynamics of hl60 cells studied using a microfluidic cell trap device. *Lab on a Chip*, 5:49–55, 2005.

[4] V. Studer, R. Jameson, E. Pellereau, A. Pepin, and Y. Chen. A microfluidic mammalian cell sorter based on fluorescence detection. *Microelectronic Engineering*, 73-4:852–857, 2004.

[5] D. Huh, Y. Kamotani, J.B. Grotberg, and S. Takayama. Microfluidics for flow cytometric analysis of cells and particles. *Physiological Measurement*, 26:R73–R98, 2005.

[6] J. Emmelkamp, F. Wolbers, H. Andersson, R.S. DaCosta, B.C. Wilson, I. Vermes, and A. van den Berg. The potential of autofluorescence for the detection of single living cells for label-free cell sorting in microfluidic systems. *Electrophoresis*, 25:3740–3745, 2004.

[7] S. Gawad, L. Schild, and P. Renaud. Micromachined impedance spectroscopy flow cytometer for cell analysis and particle sizing. *Lab on a Chip*, 1:76–82, 2001.

[8] A.B. Fuchs, A. Romani, D. Freida, G. Medoro, M. Abonnenc, L. Altomare, I. Chartier, D. Guergour, C. Villiers, P.N. Marche, M. Tartagni, R. Guerrieri, F. Chatelain, and N. Manaresi. Electronic sorting and recovery of single live cells from microlitre sized samples. *Lab on a Chip*, 6:121–126, 2006.

[9] S. Sershen and J. West. Implantable, polymeric systems for modulated drug delivery. *Advanced Drug Delivery Reviews*, 54:1225–1235, 2002.

[10] N.J. Lamb, C. Gauthier-Rouviere, and A. Fernandez. Microinjection strategies for the study of mitogenic signaling in mammalian cells. *Frontiers in Bioscience: a journal and virtual library*, 1:d19–29, 1996.

[11] M. Saito, Y. Mukai, T. Komazaki, K.-B. Oh, Y. Nishizawa, M. Tomiyama, N. Shibuya, and H. Matsuoka. Expression of rice chitinase gene triggered by the direct injection of ca2+. *Journal of Biotechnology*, 105:41–49, 2003.

[12] M. Puchi, K. Quinones, C. Concha, C. Iribarren, P. Bustos, V. Morin, A.M. Genevière, and M. Imschenetzky. Microinjection of an antibody against the cysteine-protease involved in male chromatin remodeling blocks the development of sea urchin embryos at the initial cell cycle. *Journal of Cellular Biochemistry*, 98:335–342, 2006.

[13] P. Kallio and J. Kuncová-Kallio. Capillary pressure microinjection of living adherent cells: Challenges in automation. *Journal of Micromechatronics*, 3:189–220, 2006.

[14] V.P. Torchilin. Recent approaches to intracellular delivery of drugs and dna and organelle targeting. *Annual Review of Biomedical Engineering*, 8:343–375, 2006.

[15] M. Furusawa, T. Nishimura, M. Yamaizumi, and Y. Okada. Injection of foreign substances into single cells by cell fusion. *Nature*, 249:449–450, 1974.

[16] D. Luo and W.M. Waltzman. Enhancement of transfection by physical concentration of dna at the cell surface. *Nature Biotechnology*, 18:893–895, 2000.

[17] I. Laffafian and M.B. Hallett. Lipid-assisted microinjection: Introducing material into the cytosol and membranes of small cells. *Biophysical journal*, 75:2558–2563, 1998.

[18] P.R. Nelson and K.C. Kent. Microinjection of dna into the nuclei of human vascular smooth muscle cells. *Journal of Surgical Research*, 106:202–208, 2002.

Chapter 2

Survey of dosing systems

This chapter presents a survey for achieving an integrated micro bi-directional dosing system, or IMBID-system, for intracellular mass transport, by means of on-chip microinjection and extraction. Until today, no IMBID-system for intracellular mass transport has been reported. In this survey we focus on the three main aspects of such a system: the hollow cell membrane penetration needle, the microfluidic network and the bi-directional dosing system for femtoliter displacements. During this survey we come to a suggestion of which technique should be used for all three main aspects to achieve a working IMBID-system for intracellular mass transport.

2.1 Introduction

In the former chapter it was shown that there is a large interest in biochemical research on single cells, and, due to developments in Lab-on-a-Chip (LOC) technology, LOC systems appeared to be very interesting for biochemists. Microinjections, injections directly into a single cell, have been performed since the 1970's [1], and led to the *in vitro* fertilization in 1978 [2], where a sperm cell is introduced to an egg cell. To our knowledge, no on-chip system is available to perform accurate microinjection, or microextraction. We expect though, that there is a huge interest in an integrated micro bi-directional dosing system, or IMBID-system, for biochemical single cell research. IMBID systems for transdermal invasive drug delivery applications have been fabricated [3], see Figure 2.1. Furthermore, experimental fully integrated devices for on-chip single cell microinjection have been fabricated, see Figure 2.2, where femtoliter droplet injections have been achieved, though not bi-directional, i.e. injection and extraction of fluid samples and thus not characterized as an IMBID system, and with a very large variation of disposed volumes [4].

The problems with an IMBID-system for intracellular mass transport are the nano- to micrometer dimensions required and the very small volumes to be dosed, in the lower femtoliter range. Conventional microfluidic systems typically meet flows and volumes in the nL/min—µL/min or pL—µL range, respectively. Furthermore, to achieve hollow needles with dimensions suitable to penetrate the cell membrane of an average sized cell of 8—10 µm in diameter, working with nanometer or sub-micrometer dimensions becomes necessary. These small dimensions generate challenging require-

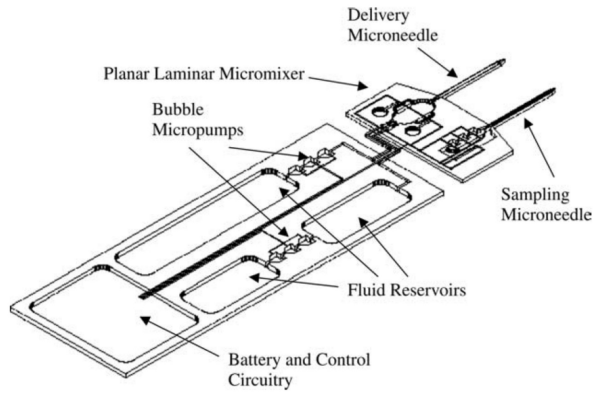ments of an IMBID-system, especially for the dosing system used.
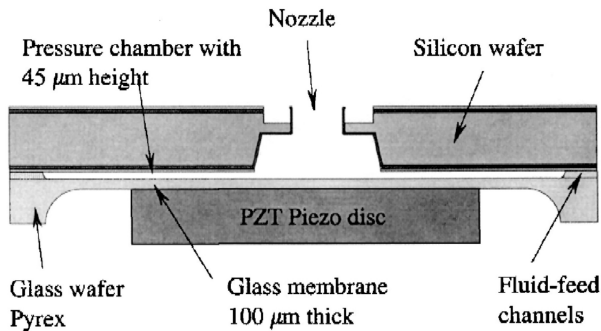

Figure 2.1: Presented by Zahn et al. [3].

Figure 2.2: Schematic cross-sectional view (not at scale) of a micromachined injector with a micron scale ring-shaped nozzle. The length of the nozzle channel is 25 µm. Image and caption taken from Luginbuhl et al. [4].

An IMBID-system should meet the following requirements to be successful:

1. Maintain cell viability

2. Small needle tips to reduce indentation depth to avoid applying stress to the cells

3. Strong needles

4. Precise control of dosed volumes, in both ways, and lower than 25 fL

5. Low power, to avoid elevated temperatures to the cells

6. Low, or no, dead volume, to increase accuracy

7. No moving parts, if possible, to avoid wear

8. Possibility for closed-loop control

9. Easy to fabricate

10. Easily integrated into microfluidic channels

In this list of requirements, we see that requirements 1 to 3 are dealing with the injection/extraction needles, requirements 4 to 8 are important for the dosing system and the last two requirements are used for both the needles and dosing system. As no IMBID-systems for intracellular mass transport have been reported yet, we focus on the literature published dealing with needles, dosing systems and nanochannels, and discuss what is needed to achieve an integrated microinjection/extraction system.

2.2 Injection needles

The first time needles, or micropipettes, were used for intracellular mass transport was for fertilization in the 1970's, where a male sperm cell was injected into a female egg cell to achieve fertilization [2]. The egg cells used in this important study were approximately 10 times larger than average mammalian cells which have sizes ranging from approximately 5 μm to 30 μm. The needles, pulled glass capillaries, had diameters on the order of tens of microns, far too large for average sized cells.

Since the first demonstration of needle injections into cells, many micro- and nano-needles have been reported using different fabrication methods, including both top-down or bottom-up fabrication technologies, and realized in different materials. The most conventional hollow microneedles are pulled glass micropipettes, such as those commercially available from Sutter (Sutter Instrument Company, Novato, CA, USA) which are suitable for patch-clamping [5] or microinjection [6]. Recently solid and hollow microneedles were reported by McAllister *et al.* [7]. They made solid and hollow microneedles in metal, biodegradable polymer, polyglycolic acid, and silicon by various techniques. Standing silicon microneedles for transdermal liquid transfer are produced with chemical wet-etching and reactive ion etching (RIE) by Gardeniers *et al.* [8], see Figure 2.3. Other transdermal liquid transfer silicon based needles, based on the mosquito's needles, are the planar microneedles made by Oka *et al.* [9]. Brinkmann *et al.* made planar silicon based needles with a slit, for capillary slot-based electrospray [10]. Carbon nanotubes, with diameters of a few nm are used in neural research for measuring electrical signals directly from the brain or nerve tissues [11]. A drawback of the carbon nanotubes is that they can not be easily integrated with an microfluidic network.
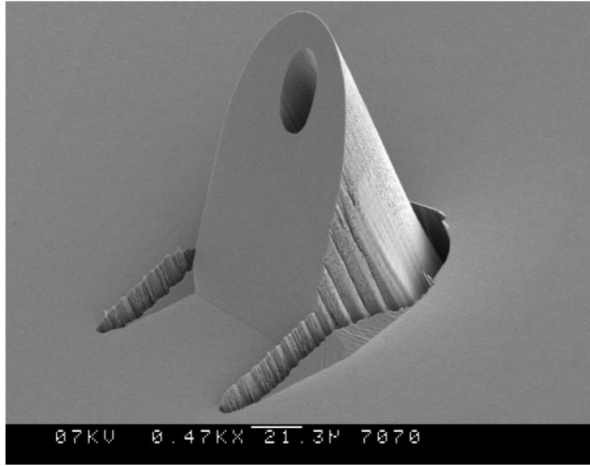
Figure 2.3: *SEM picture of a micromachined hollow microneedle for transdermal drug delivery. Adapted from Gardeniers et al. [8].*

In the specific field of micromachined microneedles for cell membrane penetration, several devices have been reported. Wong *et al.* have produced micromachined micropipettes and single-cell traps for drug injection, but these are not suitable for chip integration [12]. Others are suitable for chip integration, like microneedles for cell membrane penetration. These needles are not suitable for injection, as the needles are not hollow [13]. Another disadvantage of these polymer, metal and silicon needles is their large size ($\sim$10 — 100 μm), which makes them unsuitable for single cell analysis, as the desirable dimension for cell membrane penetration is $\sim$1 μm [14]. A very gentle way for intracellular mass transport was presented by Laffafian, where he used lipid-assisted microinjection [15]. Instead of penetrating the cell membrane and introducing stresses to the cell, he used an micropipette with lipid at the tip. These lipids merged with the cell membrane and an opening was created. For an automated system, the aligning of the cells to the needle is very delicate, making this system less suitable for an IMBID system.

Two types of micro- and nanoneedles have been made that are suitable for single cell analysis: solid AFM-tip needles and hollow liquid transfer needles. These solid needles on AFM-tips are used for cell membrane penetration force measurements [14; 16] or voltammetry [17]. Standing hollow silicon based microneedles inside small wells have been produced by Cabodevila *et al.* [18] and Guenat *et al.* [19]. The length of the needles produced by Cabodevila are limited by the depth of the wells, whereas structures reported by Guenat could extend above the surface, thus increasing the length. Another technique has been introduced by Wong *et al.* [20], where they describe sharpened fused silica microcapillary tubing fabricated by wet-chemical etching. With their etching process it is possible to make cell injection needles and cell trap devices. Prinz *et al.* [21] introduced a bottom-up fabrication approach where an InGaAs/GaAs heterofilm scrolls and forms a microtube, which have been used to successfully penetrate onion cell membranes.
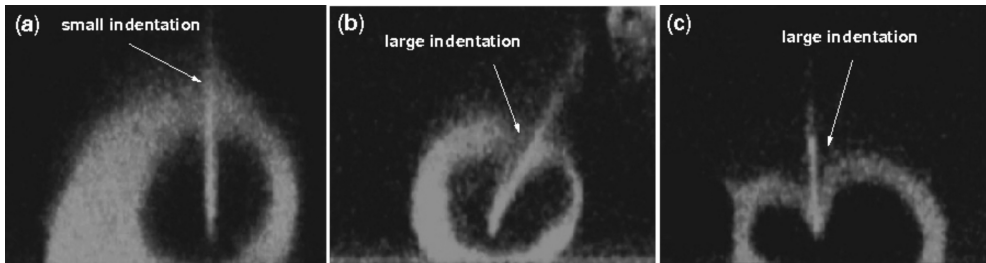
Figure 2.4: *Examples of cell membrane indentation (a) successful pene-tration of the membrane showing minimal indentation (b) no penetration with large indentation, and (c) very large indentation depth. Adapted from Obataya et al. [16].*
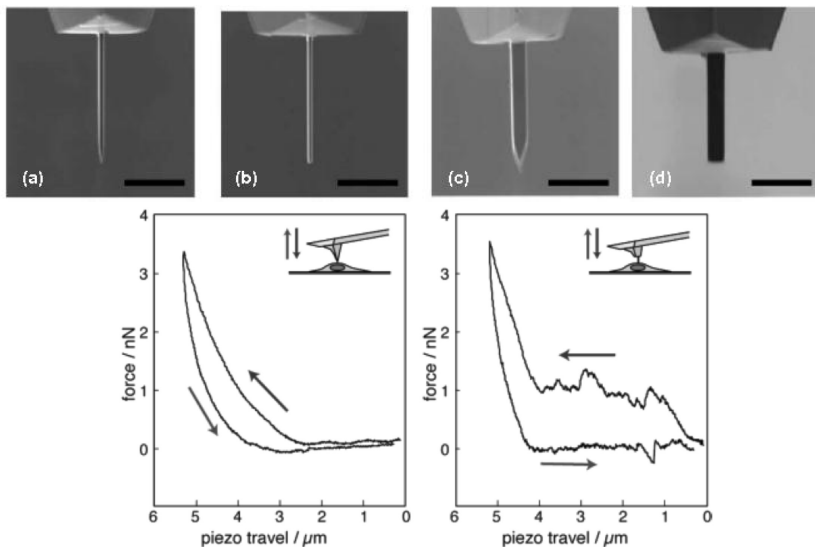
Figure 2.5: *Top: Examples of SEM images of modified AFM tips (a) and (b) needle diameters 200 nm (c) and (d) needle diameters 800 nm. Scale bar: 3 μm. Adapted from Obataya et al. [14]. Bottom: Examples of cell measured penetration forces. Adapted from Obataya et al. [16].*

The most important aspect of using needles to inject samples to living cells is to maintain cell viability before, during and after the injection procedure. It has been re-ported that mechanical stress causes various changes in cell activity [22; 16]. It is sug-gested that a distance of indentation before penetration less than 1 μm causes low me-chanical stress in average sized cells (see Figure 2.4) and, because of that, low changes in cell activity [16]. Figure 2.5 shows comparisons between a successful cell membrane penetration with a nanoneedle in part (a) and no penetration leading to large cell wall

indentation and possible cell damage in parts (b) and (c).

Nanoneedles were modified from conventional AFM tips using focused ion beam (FIB) machining. Figure 2.5 (a)—(d) show nanoneedles ranging in diameter from 200 nm to 800 nm. Obataya *et al.* investigated the required penetration force and measured the indentation depth [14]. The lower image in Figure 2.5 shows AFM traces examples of the penetration forces. The best results, based on lowest penetration force and indentation depth, were achieved with 200 nm diameter cylinder silicon nanoneedles with a measured force of 0.65 nN, a penetration probability of 92% and an indentation depth of 610 nm.

Based on the reported results and shapes by Obataya *et al.* [14], we assume that cylindrical needles, with a radial frontal area, cause large stress in the cell membrane at positions where the corner of the needle tip is in contact. This results in rupture of the membrane locally, followed by penetration, with lower indentation depth and penetration force than with prism needles. Therefore, we expect easy cell membrane penetration with small needles with radial front sides. Han *et al.* showed cell membrane penetration with nanoneedles upto 600 nm diameter attached to AFM tips without leakage or cell death after 150 minutes [23]. To achieve hollow nanoneedles with dimensions small enough to maintain cell viability, it is clear that nanoneedles integrated with nanochannels are important to achieve an integrated dosing system.

2.2.1   Nanochannels

Generally, one speaks about nanochannels if at least one dimension of the channel, the width or the height, is in the 1–100 nm range. When one dimension is in this range, one speaks about 1D-nanochannels, with both dimensions in this range one calls it 2D-nanochannels. Different types of nanochannels have been described in a recent review paper by Perry [24]. In this paper, Perry describes three different fabrication methods for silicon based nanochannels:

1. Bulk nanomachining and wafer bonding

2. Nanoimprint lithography

3. Surface nanomachining

A fourth fabrication method mentioned by Perry is *buried channel technology*, but the produced channels were still in the micrometer range.

The most popular fabrication method appears to be *bulk nanomachining and wafer bonding*, where micrometer wide and nanometer deep trenches are etched in glass [25; 26; 27] or a silicon bottom wafer [27; 28; 29] using conventional photolithography and RIE or wet-etching. After etching the bottom wafer, it is bonded to a glass or silicon top wafer by anodic bonding. A very new method in this bulk etching is introduced by Kwon *et al.* [30], where he produces nanometer wide and micrometer deep trenches in silicon by using a special optical lithography step called NSOL. NSOL is an optical lithography using an ultraviolet or visible laser as the light source, and a near-field scanning optical microscope as an photoresist imprint tool. The imprinting gives the structures in the photoresist. RIE and anisotropic wet-etching in a silicon <110>-wafer is then used to etch trenches in the silicon below the photoresist imprintings. These trenches could be covered with a bonded wafer to produce micrometer deep nanochannels.

Another technique is *nanoimprint lithography*(NIL) [31; 32; 33]. NIL uses a polymer film stamped with a mold, usually an etched silicon wafer. This structured polymer film can be placed on a silicon based substrate to produce nanochannels on top of the silicon based substrate. Usually the width and the height of the channel are in the same order of magnitude, as for very narrow channels stiction of the channel walls becomes a problem due to the flexibility of the polymer.
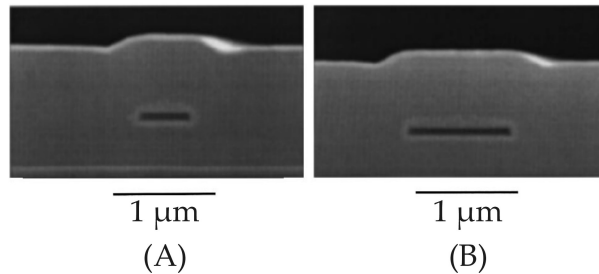

$\overline{\text{1 μm}}$ $\overline{\text{1 μm}}$

(A)   (B)

Figure 2.6: *Scanning electron micrographs of the cross section of a nano-channel produced using the sacrificial layer technique, or surface nanomachining. (A) 0.5 μm wide and 100 nm high, (B) 1 μm wide and 100 nm high. Images taken from Stern et al. [34].*

The third technique known as *surface nanomachining* combines small dimensions with stiff walls. With this technique, introduced by Stern in 1997 [34], a sacrificial layer is used. This sacrificial layer is structured in the shape of the designed fluidic network, and structured on top of a silicon nitride or oxide ground layer. Over the sacrificial layer a silicon nitride or oxide capping layer is deposited. The sacrificial material is removed using wet-chemical etching, with a very good selectivity between the sacrificial material and the silicon nitride or oxide. Stern used a 100 nm thick strip of amorphous silicon as sacrificial layer, and etched using a TMAH-water solution. Scanning electron micrographs of the cross section of produced nanochannels are shown in Figure 2.6. Other sacrificial layers can be poly-silicon or an easy removable metal. This technique leaves nanochannels with thinner and stiffer walls than is possible with the nanoimprint technology. The different nanochannels produced in this way differ from each other in the way the sacrificial strip is created. 1d-confined nanochannels, with the height of the channel in the nanometer range, are produced with thin sacrificial strip produced with conventional photolithography and RIE or wet-etching [34; 35]. Tas *et al.* introduced two ways to produce 2d-confined nanochannels [36]. The first way is using a nanowire of sacrificial material at the side wall of a step, the second is based on etching of a sacrificial strip separating the substrate and the capping layer. During drying of the structure the capping layer is pulled down by the capillary forces of the remaining liquid, and once brought in contact with the substrate, adheres permanently forming a nanochannel. A last way to produce 2d-confined nanochannels is described by Han *et al.*, where the sacrificial material between two layers of silicon nitride is wet-etched partly before the silicon oxide capping layer is deposited [37]. This method always gives two nanochannels running parallel to each other, which can be a problem when more complex networks are necessary.

The 1d-confined nanochannels fabricated using surface nanomachining are very suitable for integration with the nanoneedles, since the two silicon nitride or silicon oxide layers can be structured as planar nanoneedles, where the substrate underneath is removed using selective chemical wet-etching or reactive ion etching.

2.3   Micropumps

In the last years several review articles have been published about micropumps [38; 39; 40; 41; 42], or about microvalves [43], which have a large technical overlap with micropumps. For microfluidic networks, pumping small amount of liquids is of great importance. Depending on functionality, pump rate and volume dispensing of the microfluidic chip one of several different pumping techniques can be used. These microfluidic pumping techniques on chip can be classified following numerous systems. Krutzch and Cooper proposed a very useful classification system [38], which has been used by Laser and Santiago in an extensive review of micropumps published in 2004 [40].

Fitting the requirements for an femtoliter dosing system, given in the introduction, with the classification system, shown in Figure 2.7, we evaluate the different pumping techniques with the following requirements, which are applicable for the micropump, stated in the introduction:

1. Precise control of dosed volumes, in both ways, and lower than 25 fL

2. Low power, to avoid elevated temperatures to the cells

3. Low, or no, dead volume

4. No moving parts, if possible

5. Possibility for closed-loop control

6. Easy to fabricate

7. Easily integrated into microfluidic channels

Requirement 1 states that the dosing volumes must be accurately controllable, and have volumes smaller than 25 fL. According to the review articles, none of the conventional micropumps meets these small volumes. Therefore, a micropump has to be chosen that can be down scaled until it is able to pump precise volumes in the fL range, and actuation dimensions are in the order of single μm.

To fabricate and integrate moving parts that can meet the requirements of these small dimensions is extremely difficult, when using diaphragm based reciprocating displacement micropumps. Luginbuhl *et al.* reported a femtoliter injector for DNA mass spectrometry based on a axial piezoelectric driven micropump [4]. Although this system was able to dose small droplets with volumes around 4 fL, the size distribution of the ejected droplets ranged from 0 to 50 fL. Therefore, this system can not meet the requirement of accuracy, due to the large dead volume in the system, as shown in Figure 2.2.

Since micropumps with moving mechanical parts and large dead volumes are not suitable, only the aperiodic displacement and dynamic micropumps might be useful. If we continue with our search for a suitable micropump for an IMBID-system, the

displacement

reciprocating

diaphragm
drivers
  -piezoelectric
    -lateral
    -axial
  -thermopneumatic
  -electrostatic
  -pneumatic
valves
  -flap
  -fixed-geometry
    -nozzle-diffuser
    -Tesla
chamber
  -single
  -multiple/series (peristaltic)
  -multiple/parallel

piston

rotary

aperiodic
 -pneumatic
 -phase change
   -thermal
   -electrochemical
 -electrowetting/thermocapillary

dynamic

centrifugal

electrohydrodynamic
 -injection
 -induction
 -conduction

electroosmotic
 -porous
 -micromachined

magnetohydrodynamic
 -DC
 -AC

acoustic streaming/ultrasonic

miscellaneous special effect
 -jet
 -gas lift
 -hydraulic ram

Figure 2.7: *Classification of pumps and micropumps; taken from Laser and Santiago [40], after Krutzch and Cooper [38]. Unshaded boxes are pump categories reviewed by Laser and Santiago of which operational micropumps have been reported.*

highly controllable volume displacement suggests the need of a closed-loop system. With such a closed-loop system, the dosed volume has to be measurable during the pumping process. As the dynamic micropumps do not have possibilities to monitor the dosed volume accurately in real-time on chip, these micropumps are not suitable either, leaving the aperiodic reciprocating micropumps. Two-phase systems can be integrated in a closed-loop system, where impedance spectrometry is used for real-time measuring of the gas/liquid ratio in a reservoir [44], or in a channel [45].

All aperiodic displacement micropumps are two-phase systems, divided in three

Figure 2.8: *Longitudinal cross section of the pneumatic bubble pump. (A) The channel is filled by capillary forces, (B) Injected gas will move toward the higher channel part, because there the capillary counter pressure is lowest, (C) gas will leave the channel at the hydrophobic openings in the channel, (D) when the gas pressure drops, the microchannel will refill by capillary forces. Images and caption taken from Tas et al. [35].*
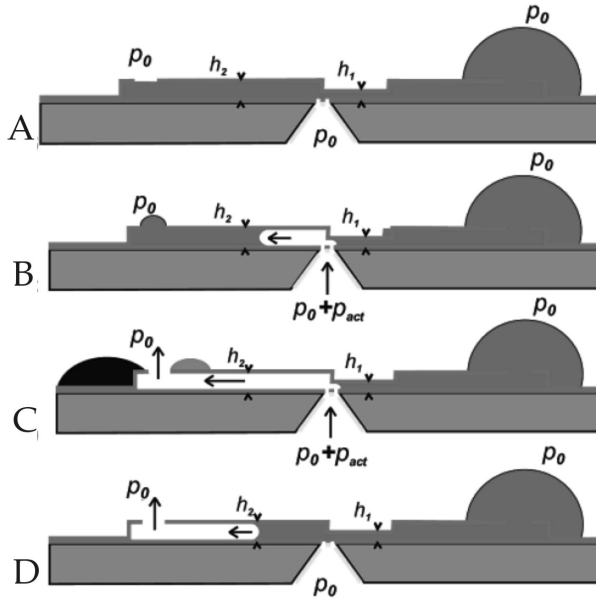
classes: pneumatic, phase change and electrowetting micropumps. Pneumatic micropumps require an external pressure source. Due to the large dead volume involved due to the interconnects, this method is not practical, unless it is used as a bubble pump proposed by Tas *et al.* [35], shown in Figure 2.8. In this system Tas *et al.* use pneumatic micropumping to deliver discrete volumes, which are independent of the back pressure. The advantage this pneumatic bubble pump is that no closed-loop system is necessary for perfect volume control, in spite of the back pressure. The pumped volumes consists of discrete volumes of 40 pL. Down sizing this pump to achieve discrete volumes of 5 fL (approximately 1% of the cell volume) requires dimensions that can not be produced using conventional contact lithography. Therefore, discrete volume delivery is not suitable, including electrowetting mechanisms, since they have the intrinsic property of discrete volume delivery.

The phase change micropumps fulfill the requirements for the micropump needed for an IMBID-system. Since phase change micropumps form only a small class in the wide technical field of micropumps, it has not been covered thoroughly in the existing review articles. Therefore, we review in the following the developments in this class of micropumps.

2.3.1 Phase change micropumps

The phase change from the liquid phase to the gas phase (liquid gas phase change, LGPC) gives a huge molar volume increase. For instance, the molar volumes of liquid water and water vapor at the boiling point under 1 bar of pressure are 18.79 mL and 30.52 L, respectively [46], a volumetric increase of more than 1600-fold. The large volume increase can be used to perform mechanical work and is therefore useful for pumping applications. Typically, the LGPC is used for actuation and pumping applications in the form of thermal boiling or electrochemical reactions at solid electrodes. Most of these chemical actuated phase change pumps are electrochemical, where electrical energy is converted directly into chemical energy by redox reactions. Figure 2.9 shows schematics of the thermal and electrochemical phase change micropumps, where the bubble actuation takes place in a large reservoir at the end of a microchannel.
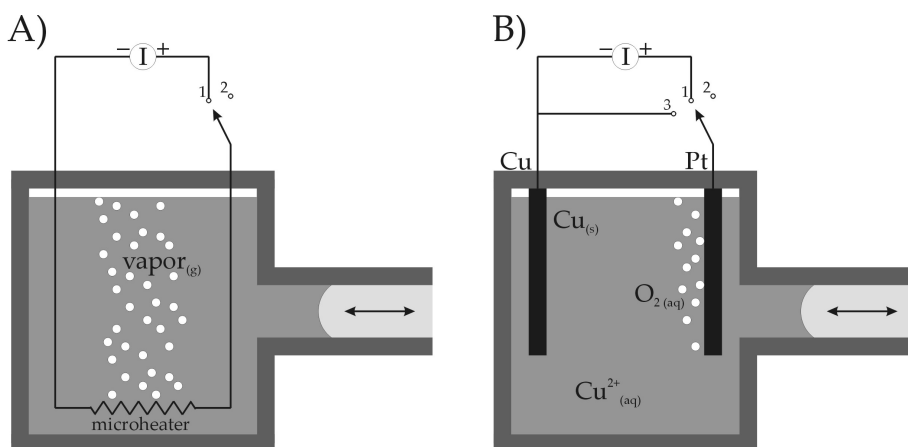
Figure 2.9: *Schematic of two types of phase change micropumps: a thermal activated bubble pump (A), and an electrochemical activated bubble pump (B). In both systems gas is generated inside a closed cavity, and liquid is pushed into a channel due to volume expansion by the bubbles. The thermal bubble pump has a microheater in or in close approximately of the liquid, that makes vapor bubbles by local boiling, or can be controlled by the applied current. The electrochemical micropump has two working electrodes, and gas bubbles are produced at one or both electrodes. In this case copper and platinum electrodes are used in a copper sulphate electrolyte, producing oxygen gas at the anode and $Cu^{2+}_{(aq)}$-ions at the cathode. The depicted electrochemical micropump is a schematic of the first electrochemical microactuator, presented by Neagu et al. [47].*

The direct energy conversion of electrical energy into chemical energy for the electrochemical micropump is in contrast with the thermal micropump, where electrical energy is converted into thermal energy, which is then converted into chemical energy. Because of this, electrochemical micropumping is easier to control and predict than thermal micropumping. On the other hand, electrochemical micropumps require a special

Table 2.1: *Specifications of several on-chip phase change micropumps. In the upper half of the table the thermal micropumps are shown, the lower half contains the electrochemical micropumps. e.chem.=electrochemical, cont./dos.=continuous and dosing*

year	author	actuation	system	rate (no back pressure)	step volume	max press.	comments
1987	Asai et al. [48]	thermal	cont./dos.	1.5 µL/min	0.25 nL		ink-jet printer model
1998	Jun, Kim [49]	thermal	continuous	220—505 pL/min	3.6—4.2pL	950 Pa	peristaltic, w/o chambers
2001	Geng et al. [50]	thermal	continuous	150 µL/min	0—0.25 µL	320 Pa	difference bubble nucleation-collapsing cites
2001	Song, Zhao [51]	thermal	continuous	0—360 µL/min	1—18µL	0.85 kPa	peristaltic, w/o chambers
2002	Tsai, Lin [52]	thermal	continuous	0—5 µL/min	0.2 nL	377 Pa	nozzle/diffuser
2004	Zahn et al. [3]	thermal	continuous	2.0 nL/min	0.17 nL	3.9 kPa	for microneedle drug delivery
2005	Yin, Prosperetti [53]	thermal	continuous	1—14 µL/min	0.4—1.23 nL		difference bubble nucleation-collapsing cites
2005	Song, Lichtenberg [54]	thermal	dosing	-0.34/-0.17/ 0.17/0.34 µL/min	0.1 µL		long relaxation times
2006	Cheng, Chien [55]	thermal	cont./dos.	~2 µL/min	400 pL		motorcycle's fuel atomizer
2006	Yoo et al. [56]	thermal	continuous	0—64 nL/min	0.1—0.4 nL		nozzle/diffuser, with vapor valves
1999	Böhm et al. [57]	e.chem.	dosing	0—1.9 µL/min	25 nL		first electrochemical bubble dosing system
2000	Böhm et al. [44]	e.chem.	dosing	-1.4—1.9 10^3 nL/min	5 nL		closed-loop dosing system
2000	Böhm et al. [58]	e.chem.	dosing			135 MPa	maximum pressure generation
2002	Suzuki, Yoneyama [59]	e.chem.	dosing	-4—5 nL/min			dosing system integrated with reference electrodes
2003	Suzuki, Yoneyama [60]	e.chem.	dosing	-0.27—0.84 µL/min			dosing system integrated with electrochemical bubble valves
2003	Furdui et al. [61]	e.chem.	dosing	0.05—1.4 µL/min			based on Böhm et al. [57]
2003	Munyan et al. [62]	e.chem.	dosing	8—13 µL/min		10.6 kPa	large glass/PDMS chip
2004	Liu et al. [63]	e.chem.	dosing	0—1000 µL/min			integrated in DNA chip
2004	Xie et al. [64]	e.chem.	dosing	40—190 nL/min		0.55 MPa	electrospray chip
2004	Ateya et al. [65]	e.chem.	continuous	10—24 nL/min	0.03 nL	9 kPa	peristaltic, chambers
2006	Liu et al. [66]	e.chem.	dosing				integrated in DNA chip

Table 2.2: *General properties of thermal and electrochemical micropumps.*

	thermal actuated	electrochemically actuated
fabrication	easy	easy
power consumption	high	low
gas volume increment	less controllable due to indirect relation electrical current—gas production	highly controllable due to direct relation electrical current—gas production
gas volume stability	low due to cooling and condensation	high when gases can not come in contact with counter electrode
gas volume decrement	fast and hard to control, by cooling down and condensation	fast and easy to control when back-reaction used
popular working field	continuous pumping	dosing
max. pressures reported	low (∼1 kPa)	high (135 MPa)
pressure/flow relation	strong	weak
advantage	no special pump medium necessary	high level of control
disadvantage	poor controllability	electrolyte and pumped medium have to be separated

electrolyte. Due to the chemical end products, this is usually not useful as the pumped medium. Therefore, it needs to be separated, requiring long narrow channels or membranes to prevent diffusion and mixing.

Several phase change micropumps have been reported, thermally as well as electrochemically. The specifications of these phase change micropumps are listed in Table 2.1. Comparing the two different systems shows that, due to the intrinsic different bubble behavior, thermal micropumps are generally used for continuous pumping, this in contrast with the electrochemical micropumps, mainly used for dosing systems. In continuous pumping, the accent is on the generated flow, whereas dosing systems focuses on dosed volume. Due to fast vapor bubble nucleation by heating, and fast collapsing of the vapor bubble after the microheater has been switched off, the thermal micropumps can achieve high actuation frequencies, which is useful for continuous pumping. Since the bubble volume of thermal micropumps is harder to control, due to the indirect conversion of electrical energy to chemical energy, these type of micropumps are less suitable for precise volume dosing. Furthermore, for bi-directional pumping, controlled gas volume reduction is required. Thermal systems have gas volume reduction caused by cooling down and condensation of the vapor, giving control problems. Furthermore, when scaling down to μm dimensions, focusing of the heat for precise bubble control becomes problematic, due to the relatively very fast heat conduction at micrometer scale. On the other hand, in electrochemical micropumps, thermal influences can be neglected. Therefore, the gas volume is in direct relation with the amount of gas in the bubble, controlled by the applied current. Since hydrogen has low solubility in water, the relation between gas production/reduction and bubble volume is strong, and high pressures can be achieved, making electrochemical phase change micropumps highly suitable for an IMBID-system. The general properties of the thermal and electrochemical micropumps are listed in Table 2.2.

2.3.2 Developments in electrochemical pumping

Neagu *et al.* were the first to see the possibility of electrochemical actuation for microfluidic networks [47; 67; 68]. In 1996 they published *An electrochemical microactuator: Principle and first results* [47], only a few years after the first results of the vapor bubble actuators [69; 70], followed by an electrochemical active valve [67]. These actuators still had mechanical parts, as the produced gas bubbles acted on a flexible membrane. Stanczyk *et al.* continued to work on membrane based electrochemical microactuators started by Neagu *et al.* [71].
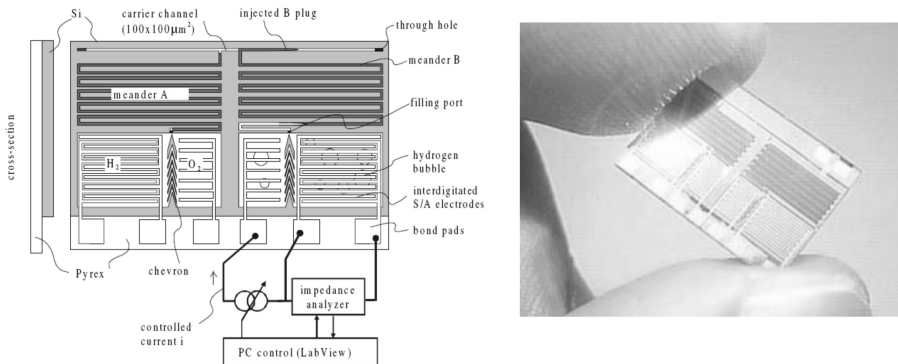

Figure 2.10: *Left: Proposed dosing system, geometry and electrical connections. Right: Photograph of a realized micromachined dual dosing system. Images and captions taken from Bohm et al. [44].*

Although Neagu *et al.* focused on membrane based valve systems as the primary use of the electrochemical actuation, it appeared that, due to the very controlled gas formation, this actuation principle was very promising for microfluidic dosing systems. The idea of electrochemical actuation for dosing systems was adapted by Böhm *et al.* during their development of an on-chip calibration system for lactate sensors [57; 44; 72]. Figure 2.10 shows a schematic of the dosing system. Böhm *et al.* used a closed-loop system to control the volume of produced gas, and therefore the dosing volume. The cathode and anode were placed in separate chambers to prevent generated gas reacting back at the counter electrode, resulting in a very stable dosing system. The electrical connection between the gas producing electrodes was achieved by placing a so called "chevron"system between the chambers. The cathode consisted of two interdigitated electrodes, enabling real time measuring of the gas production volume, using an AC-signal. The dosed volumes could be kept within a range of about 5 nL, by adopting closed-loop control based on the measured cell resistance. Fluidic control was improved further by the application of a negative neutralizing pulse to remove dissolved gas from the supersaturated regions near the electrodes. A disadvantage of the presented dosing system could be the long reaction and relaxation times, in the order of 20 s and 60 s, respectively. The concept of Böhm *et al.* of having two individually operating dosing systems for calibration purposes was adapted by Furdui *et al.* to isolate rare cells in blood [61].
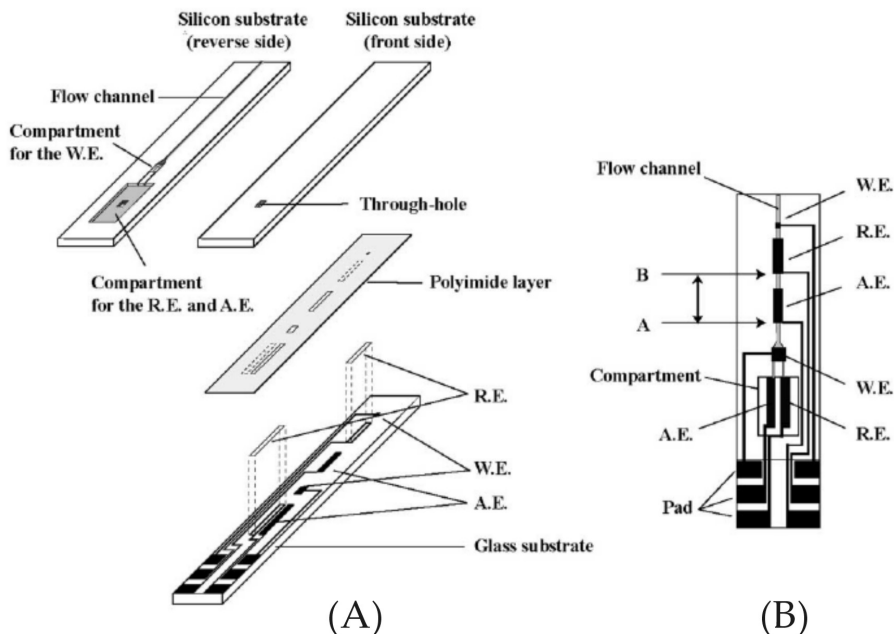
Figure 2.11: *Microsystem with the dosing mechanism and the sensing electrodes: (A) construction of the system; (B) top-view of the completed system. Images taken from Suzuki and Yoneyama [59].*
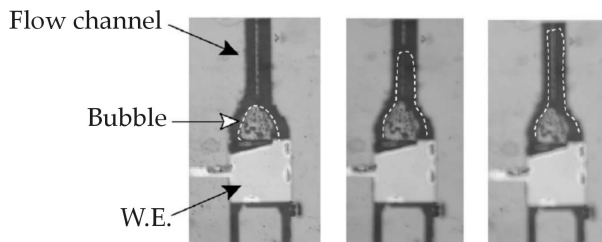
Figure 2.12: *Microscope photographs showing the growth of a hydrogen bubble at the working electrode of the micropump. The status of the bubble is shown from left to right at 10, 15 and 20 s, respectively, after applying −1.2 V to the working electrode. Images taken from Suzuki and Yoneyama [59].*

After the innovative work of Neagu *et al.* and Böhm *et al.*, Suzuki and Yoneyama presented a complete electrochemical dosing system with integrated electrochemical reference electrodes, see Figure 2.11 for a layout of the system [59]. The basic idea of this system is similar to the proposed system of Böhm *et al.*, though, Suzuki and Yoneyama used a three-electrode configuration (Pt working electrodes, Pt auxiliary electrodes and

Ag/AgCl reference electrodes), and only hydrogen gas was generated at the working electrode. Due to the larger surface area of the auxiliary electrode, oxygen bubble formation could be prevented. In contrast with the system of Böhm *et al.*, gas bubble production was performed inside a small cavity, from where bubble growth continued into the microchannel, see Figure 2.12. As a result of this, with comparable flow rates, the controllability of the system increased and the reaction times were reduced to less than 10 s. Controlled bubble growth and shrinkage rates of 2 nL/s were achieved, using a working electrode with an active area of 600 µm × 600 µm inside a cavity of 700 µm × 700 µm × 190 µm (length×width×depth), channel dimension was 9.2 mm × 300 µm × 190 µm, respectively. In 2003, Suzuki and Yoneyama presented an integrated microfluidic system with electrochemically actuated dosing systems and valves, based on the system presented in 2002 [60]. This new system was used for mixing two fluids, both actuated by an on-chip electrochemical dosing system.
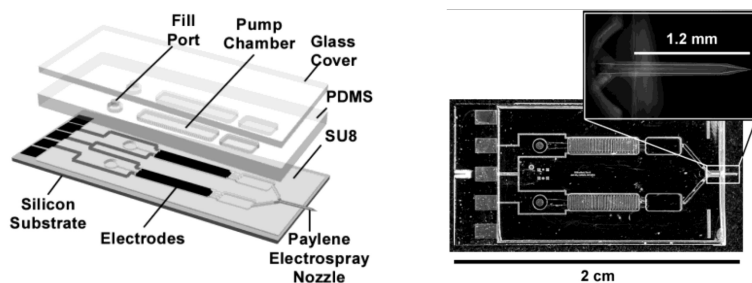

Figure 2.13: *Exploded view (left) and top view (right) of the produced electrochemical dosing chip for electrospray use, by Xie et al. [64].*

The practical use of an electrochemical dosing system was illustrated further by Xie *et al.*, who integrated two electrochemical dosing systems with an electrospray nozzle, see Figure 2.13 [64]. The flow rates varied from 40 nL/min to 190 nL/min and the total dispensing volume was 1.6 µL. The pumping efficiencies, i.e. the ratio between the ideal flow rate, based on applied current, and the observed flow rate, were low, 0.22 and 0.40, respectively.

Liu *et al.* showed even more practical use of the electrochemical dosing systems in fully integrated biochips. In 2004 they published a plastic biochip with three integrated electrochemical dosing systems and one thermopneumatic air dosing system for sample preparation, polymerase chain reaction amplification, and DNA microarray detection, see Figure 2.14 [63]. The electrochemical dosing systems were used to dose in the mL range, where the thermopneumatic air dosing system was used for dosing in the µL range. This biochip was followed in 2006 by a fully integrated miniature device for automated gene expression DNA microarray processing, actuated by five plastic electrochemical dosing systems with stainless steel electrodes [66].

Due to the slower kinetics-limited deflation of electrochemical bubbles compared to temperature-limited thermal vapor bubbles, continuous flow pumping was less obvious for electrochemically actuated system than it was for thermally actuated systems [73]. In 2002, Hua *et al.* showed that by generating bubbles electrochemically directly inside
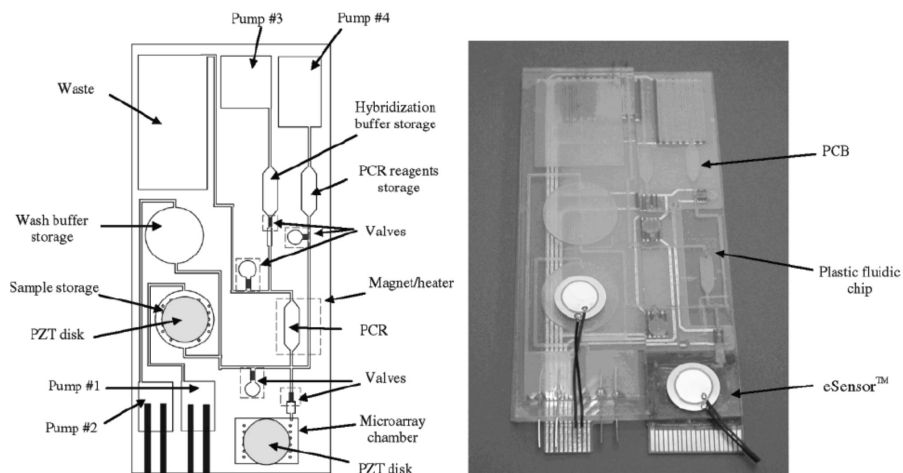
Figure 2.14: Left: Schematic of the plastic microfluidic chip by Liu et al. Pumps 1—3 are electrochemical dosing systems, and pump 4 is a thermopneumatic air dosing system. Right: Photograph of the integrated device that consists of a plastic microfluidic chip, a printed circuit board (PCB), and a Motorola eSensor microarray chip. Images taken from Liu et al. [63].
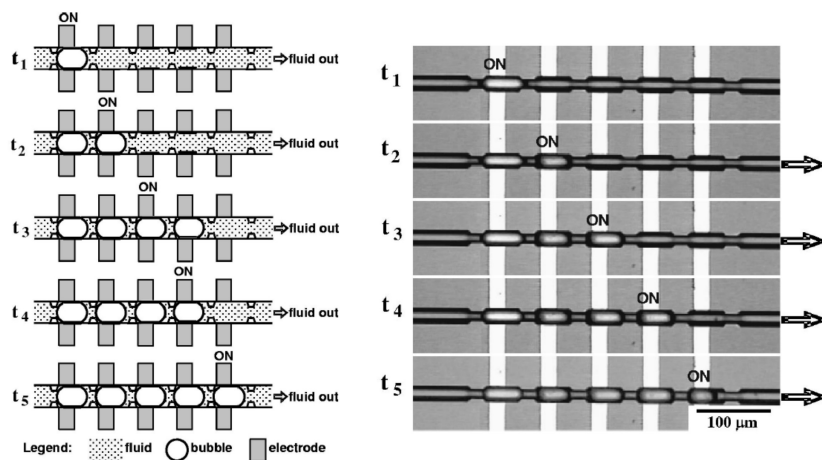
Figure 2.15: Left: Schematic illustrating the pumping of fluid using a sequential electrochemical bubble pump. The successive voltage pulses to generate bubbles were applied in a time sequence t_1 through t_5. Right: Optical micrographs showing successive generation of five bubbles in the channel using a sequence of voltage pulses. The arrows indicate flow direction. Images and descriptions by Ateya et al. [65].

Figure 2.16: *(B_{1-6}) Microscope photographs showing bubble inflation and deflation. The flow direction through the microchannel is indicated by an arrow. The times between the successive photographs is ~50 ms. (C_{1-6}) Fluorescent microscopy images corresponding to B_{1-6} showing valve closing and opening. In C_{1-6}, the interaction between the bubble and the flow was visualized using polystyrene fluorescent microspheres as t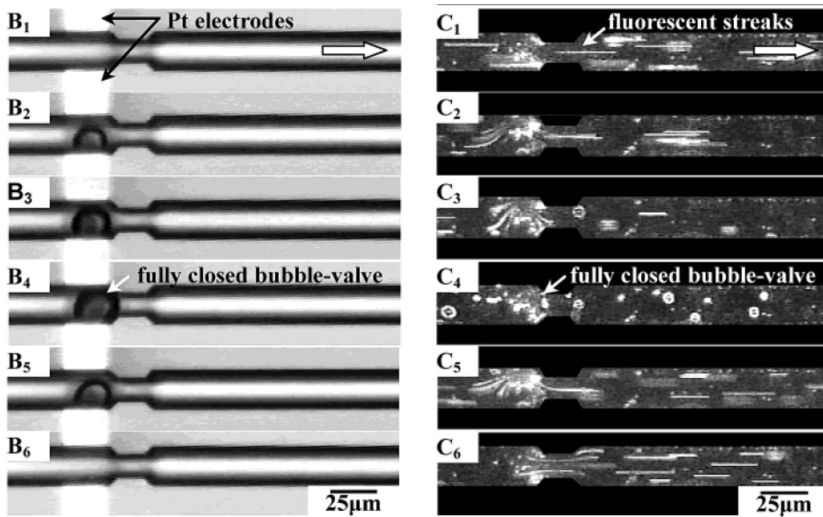racers of flow. Top electrode is anode, bottom electrode is cathode; electrolyte is 1.0 M NaCl. Adapted from Hua et al. [73].*

the small microchannels, the effective deflation rates were increased. Making use of the difference in capillary pressures, induced by narrowing of the microchannel from 25 μm to 15 μm, the bubble acted as a valve, able to block and unblock the channel in ~150 ms and ~100 ms, approximately, and able to resist inlet pressures of 5 kPa [73].

By positioning multiple valve structures in series, a continuous peristaltic micropump was fabricated by Hua's co-worker Ateya *et al.*, in 2004 [65], shown in Figure 2.15. Optimized pump rates of 24 nL/min (flow velocity: 640 μm/s, channel cross section: 25 μm × 25 μm) were achieved using five valve structures in series. An advantage of this valve structured electrochemical actuated bubble pump is the high back pressure it can operate on, up to 10 kPa, whereas the vapor bubble pumps could achieve a 800 Pa pressure head [74; 49]. Furthermore, the pump rate is much less influenced by the back pressure, due to the valve structure and high control over the electrochemical reaction, and therefore, no closed-loop system is necessary. However, this is a discrete system, where the volume steps are limited by the volumes of the individual chambers. Achieving small chambers with volumes of approximately 5 fL will be problematic.

Using the original valve structure by Hua *et al.* [73], as shown in Figure 2.16, the bubble can be grown inside the channel, to achieve no dead volume, and be directed in one way, as is the case when using conventional reservoirs. Due to the small gas/liquid interfaces, the gas diffusion into the liquid will be low, giving stable bubble volumes.

Gas volume reduction can be achieved by applying an inversed current. This system can be easily integrated with an impedance based gas volume sensors, for closed-loop integration [45].

2.4   Conclusions and Outlook

In the survey of an integrated micro bi-directional dosing system (IMBID system), we divided the system in three parts: the needle, the fluidic network and the pump. Due to the small sizes of a normal mammalian cell, developing such a system gives intriguing challenges, including sub-micron sized hollow needle tips with integrated nanochannels, and highly controllable micropumps capable of dosing in the femtoliter range.

For the needles we suggest using planar silicon nitride or oxide needles, integrated with 1d-confined nanochannels, fabricated using the sacrificial layer technique. Other techniques for nanochannel integration in needle tips will lead to difficulties or problems concerning fabrication, integration and needle tip diameters. Easy integration of the nanochannel in the needle is possible since the encapsulation layers of the nanochannel can be used as needle material when it is shaped with reactive ion etching and chemical wet-etching. Since large indentation depths cause high stress in the cell membrane, and therefore it is related to cell viability, these should be avoided. Therefore, design and fabrication of the needle tip is difficult, which has to have dimensions and penetration properties so it penetrates without causing large indentation depths.

Finding an easy integratable and accurate micropump system that is able to dose volume samples lower than 25 fL, bi-directionally, is a difficult task, as no reported micropump system is able to achieve this challenging task. Because of requirements dealing with precise control, including closed-loop systems if necessary, good down scaling possibilities and easy integration and fabrication, bubble based electrochemical phase-change micropumps are possible solutions. Due to the lack of literature review articles on these micropumps, the developments in these micropumps have been reviewed in this chapter. This shows that a capillary valve structure can be used for in-channel bubble evolution, resulting in pumping. We expect that, due to the good down-scaling properties of this kind of pumping, that bi-directional pumping in the femtoliter range can be achieved. This micropump can be easily integrated with the microfluidic network of nanochannels, needed for the hollow needles, giving high accuracy in pumping due to no dead-volume.

Therefore, we suggest integrating planar silicon nitride or silicon oxide submicro-needles with 1d-confined nanochannels and electrochemically actuated micropumps for an IMBID-system for intracellular mass transport.

Bibliography

[1] M. Furusawa, T. Nishimura, M. Yamaizumi, and Y. Okada. Injection of foreign substances into single cells by cell fusion. *Nature*, 249:449–450, 1974.

[2] P.C. Steptoe and R.G. Edwards. Birth after the reimplantation of a human embryo. *Lancet*, 2:366, 1978.

[3] J.D. Zahn, A. Deshmukh, A.P. Pisano, and D. Liepmann. Continuous on-chip micropumping for microneedle enhanced drug delivery. *Biomedical Microdevices*, 6:183–190, 2004.

[4] Ph. Luginbuhl, P.-F. Indermuhle, M.-A. Grétillat, F. Willemin, N.F. de Rooij, D. Gerber, G. Gervasio, J.-L. Vuilleumier, D. Twerenbold, M. Düggelin, D. Mathys, and R. Guggenheim. Femtoliter injector for dna mass spectrometry. *Sensors&Actuators B*, 63:167–177, 2000.

[5] T. Sordel, S. Garnier-Raveaud, F. Sauter, C. Pudda, F. Marcel, M. De Waard, C. Arnoult, M. Vivaudou, F. Chatelain, and N. Picollet d'Hahan. Hour glass SiO_2 coating increases the performance of planar patch-clamping. *Journal of Biotechnology*, 125:142–154, 2006.

[6] S.W. de Laat, P.T. van der Saag, W. Leurink, and S.K. Brahma. A device for micro-injection of nanolitre quantities without precalibration. *Experimental Cell Research*, 84:367–373, 1974.

[7] D.V. McAllister, P.M. Wang, S.P. Davies, J.H. Park, P.J. Canatella, M.G. Allen, and M.R. Prausnitz. Microfabricated needles for transdermal delivery of macromolecules and nanoparticles: fabrication methods and transport studies. *PNAS*, 100:13755–13760, 2003.

[8] J.G.E. Gardeniers, R. Luttge, J.W. Berenschot, M.J. de Boer, Y. Yeshurun, M. Hefetz, R. van 't Oever, and A. van de Berg. Silicon micromachined hollow microneedles for transdermal liquid transfer. *Journal of Microelectromechanical systems*, 12:855–862, 2003.

[9] K. Oka, S. Aoyagi, Y. Arai, Y. Isono, G. Hashiguchi, and H. Fujita. Fabrication of a micro needle for a trace blood test. *Sensors&Actuators A*, 97-98:478–485, 2002.

[10] M. Brinkmann, R. Blossey, S. Arscott, C. Druon, P. Tabourier, S. le Gac, and C. Rolando. Microfluidic design rules for capillary slot-based electrospray sources. *Applied Physics Letters*, 85:2140–2142, 2004.

[11] D. Pantarotto, J.P. Briand, M. Prato, and A. Bianco. Translocation of bioactive peptides across cell membranes by carbon nanotubes. *ChemComm*, pages 16–17, 2004.

[12] P.K. Wong, U. Ulmanella, and C.M. Ho. Fabrication of microsurgical tools for single-cell intracytoplasmic injection. In *MEMS2003 conference proceedings*, pages 359–362, 2003.

[13] T. Ichiki, Y. Sugiyama, S. Kase, and Y. Horiike. Surface micromachined hollow microneedle array integrated on a microfluidic chip. In *µTAS2003 conference proceedings*, pages 1025–1028, 2003.

[14] I. Obataya, C. Nakamura, S.W. Han, N. Nakamura, and J. Miyake. Mechanical sensing of the penetration of various nanoneedles into a living cell using atomic force microscopy. *Biosensors and Bioelectronics*, 20:1652–1655, 2005.

[15] I. Laffafian and M.B. Hallett. Lipid-assisted microinjection: Introducing material into the cytosol and membranes of small cells. *Biophysical journal*, 75:2558–2563, 1998.

[16] I. Obataya, C. Nakamura, S.W. Han, N. Nakamura, and J. Miyake. Nanoscale operation of a living cell using an atomic force microscope with a nanoneedle. *Nano Letters*, 5:27–30, 2005.

[17] R.J. Fasching, S.J. Bai, T. Fabian, and F.B. Prinz. Nanoscale electrochemical probes for single cell analysis. *Microelectronic Engineering*, 83:1638–1641, 2006.

[18] G. Cabodevila, B. Lepioufle, and H. Fujita. Arrayed micro needles for mechanical gene insertion. In *Biomedical Applications of Micro- and Nanoengineering*, pages 90–97, 2002.

[19] O.T. Guenat, S. Generelli, M. Dadras, L. Berdondini, N.F. de Rooij, and M. Koudelka-Hep. Generic technological platform for microfabricating silicon nitride micro- and nanopipette arrays. *Journal of Micromechanics and Microengineering*, 15:2372–2378, 2005.

[20] P.K. Wong, U. Ulmanella, and C.M. Ho. Fabrication process of microsurgical tools for single-cell trapping and intracytoplasmic injection. *Journal of Microelectromechanical systems*, 13:940–946, 2004.

[21] A.V. Prinz, V.Ya. Prinz, and V.A. Seleznev. Semiconductor micro- and nanoneedles for microinjections and ink-jet printing. *Microelectronic Engineering*, 67-68:782–788, 2003.

[22] R.M. Hochmuth. Micropipette aspiration of living cells. *Journal of Biomechanics*, 33:15–22, 2000.

[23] S.W. Han, C. Nakamura, I. Obataya, N. Nakamura, and J. Miyake. Gene expression using an ultrathin needle enabling accurate displacement and low invasiveness. *Biochemical and Biophysical Research Communications*, 332:633–639, 2005.

[24] J.L. Perry and S.G. Kandlikar. Review of fabrication of nanochannels for single phase liquid flow. *Microfluidics & Nanofluidics*, 2:185–193, 2006.

[25] J. Haneveld, H.V. Jansen, J.W. Berenschot, N.R. Tas, and M. Elwenspoek. Wet anisotropic etching for fluidic 1D nanochannels. *Journal of Micromechanics and Microengineering*, 13:S62–S66, 2003.

[26] V.G. Kutchoukov, F. Laugere, W. van der Vlist, L. Pakula, Y. Garini, and A. Bossche. Fabrication of nanofluidic devices using glass-to-glass anodic bonding. *Sensors&Actuators A*, 114:521–527, 2004.

[27] P. Mao and J. Han. Fabrication and characterization of 20 nm planar nanofluidic channels by glass-glass and glass-silicon bonding. *Lab on a Chip*, 5:837–844, 2005.

[28] P.M. Sinha, G. Valco, S. Sharma, X. Liu, and M. Ferrari. Nanoengineered device for drug delivery application. *Nanotechnology*, 15:S585–S589, 2004.

[29] T.S. Hug, N.F. de Rooij, and U. Staufer. Fabrication and electroosmotic flow measurements in micro- and nanofluidic channels. *Microfluidics & Nanofluidics*, 2:117–124, 2006.

[30] S.J. Kwon, Y.M. Jeong, and S.H. Jeong. Fabrication of high-aspect-ratio silicon nanostructures using near-field scanning optical lithography and silicon anisotropic wet-etching process. *Applied Physics A*, 86:11–18, 2007.

[31] S.H. Zaidi and S.R.J. Brueck. Interferometric lithography for nanoscale fabricating. In *Proceedings of SPIE, San Jose, vol. 3618*, pages 2–8, 1999.

[32] J.J. Dumond, H.Y. Low, and I. Rodriguez. Isolated, sealed nanofluidic channels formed by combinatorial-mould nanoimprint lithography. *Nanotechnology*, 17:1975–1980, 2006.

[33] P. Kim, H.E. Jeong, A. Khademhosseini, and K.Y. Suh. Fabrication of non-biofouling polyethylene glycol micro- and nanochannels by ultraviolet-assisted irreversible sealing. *Lab on a Chip*, 6:1432–1437, 2006.

[34] M.B. Stern, M.W. Geis, and J.E. Curtin. Nanochannel fabrication for chemical sensors. *Journal of Vacuum Science & Technology B*, 15:2887–2891, 1997.

[35] N.R. Tas, J.W. Berenschot, T.S.J. Lammerink, M. Elwenspoek, and A. van den Berg. Nanofluidic bubble pump using surface tension directed gas injection. *Analytical Chemistry*, 74:2224–2227, 2002.

[36] N.R. Tas, J.W. Berenschot, P. Mela, H.V. Jansen, M. Elwenspoek, and A. van den Berg. 2D-confined nanochannels fabricated by conventional micromachining. *Nano Letters*, 2:1031–1032, 2002.

[37] A. Han, G. Mondin, N.G. Hegelbach, N.F. de Rooij, and U. Staufer. Filling kinetics of liquids in nanochannels as narrow as 27 nm by capillary force. *Journal of Colloid and Interface Science*, 293:151–157, 2006.

[38] W.C. Krutzch and P. Cooper. *Pump Handbook*, chapter Introduction: classification and selection of pumps. McGraw-Hill, 2001.

[39] N.-T. Nguyen, X. Huang, and T.K. Chuan. MEMS-micropumps: A review. *Journal of Fluids Engineering*, 124:384–392, 2002.

[40] D.J. Laser and J.G. Santiago. A review of micropumps. *Journal of Micromechanics and Microengineering*, 14:R35–R64, 2004.

[41] V. Singhal, S.V. Garimella, and A. Raman. Microscale pumping technologies for microchannel cooling systems. *Applied Mechanics Reviews*, 57:191–221, 2004.

[42] P. Woias. Micropumps–past, progress and future prospects. *Sensors&Actuators B*, 105:28–38, 2005.

[43] K.W. Oh and C.H. Ahn. A review of microvalves. *Journal of Micromechanics and Microengineering*, 16:R13–R39, 2006.

[44] S. Böhm, B. Timmer, W. Olthuis, and P. Bergveld. A closed-loop controlled electrochemically actuated micro-dosing system. *Journal of Micromechanics and Microengineering*, 10:498–504, 2000.

[45] D.A. Ateya, A.A. Shah, and S.Z. Hua. Impedance-based response of an electrolytic gas bubble to pressure in microfluidic channels. *Sensors&Actuators A*, 122:235–241, 2005.

[46] D.R. Lide. *Handbook of Chemistry and Physics*. CRC, 74 edition, 1993-1994.

[47] C.R. Neagu, J.G.E. Gardeniers, M. Elwenspoek, and J.J. Kelly. An electrochemical microactuator: principle and first results. *Journal of Microelectromechanical systems*, 5:2–9, 1996.

[48] A. Asai, T. Hara, and I. Endo. One-dimensional model of bubble growth and liquid flow in bubble jet printers. *Japanese Journal of Applied Physics*, 26:1794–1801, 1987.

[49] T.K. Jun and C.-J. Kim. Valveless pumping using traversing vapor bubbles in microchannels. *Japanese Journal of Applied Physics*, 83:5658–5664, 1998.

[50] X. Geng, H.N. Oguz, and A. Prosperetti. Bubble-based micropump for electrically conducting liquids. *Journal of Micromechanics and Microengineering*, 11:270–276, 2001.

[51] Y.J. Song and T.S. Zhao. Modelling and test of a thermally-driven phase-change nonmechanical micropump. *Journal of Micromechanics and Microengineering*, 11:713–719, 2001.

[52] J.-H. Tsai and L. Lin. A thermal-bubble-actuated micronozzle-diffuser pump. *Journal of Microelectromechanical systems*, 11:665–671, 2002.

[53] Z. Yin and A. Prosperetti. 'blinking bubble' micropump with microfabricated heaters. *Journal of Micromechanics and Microengineering*, 15:1683–1691, 2005.

[54] W.H. Song and J. Lichtenberg. Thermo-pneumatic, single-stroke micropump. *Journal of Micromechanics and Microengineering*, 15:1425–1432, 2005.

[55] H.-P. Cheng and C.-P. Chien. Ejection interaction of two adjacent micropumps. *Journal of Fluids Engineering*, 128:742–750, 2006.

[56] J.-C. Yoo, M.-C. Moon, C.J. Kang, D. Jeon, and Y.-S. Kim. Dynamic characteristics of the micro-fluidic systems actuated by thermopneumatic-method. *Japanese Journal of Applied Physics*, 45:519–522, 2006.

[57] S. Böhm, W. Olthuis, and P. Bergveld. An integrated micromachined electrochemical pump and dosing system. *Journal of Biomedical Microdevices*, 1:2:121–130, 1999.

[58] S. Böhm, H. van der Linden, A. van den Berg, W. Olthuis, and P. Bergveld. High pressure gas-liquid mixtures generated in a micro-electrolysis cell. In *μTAS2000 conference proceedings*, pages 611–614, 2000.

[59] H. Suzuki and R. Yoneyama. A reversible electrochemical nanosyringe pump and some considerations to realize low-power consumption. *Sensors&Actuators B*, 86:242–250, 2002.

[60] H. Suzuki and R. Yoneyama. Integrated microfluidic system with electrochemically actuated on-chip pumps and valves. *Sensors&Actuators B*, 96:38–45, 2003.

[61] V.I. Furdui, J.K. Kariuki, and D.J. Harrison. Microfabricated electrolysis pump system for isolating rare cells in blood. *Journal of Micromechanics and Microengineering*, 13:S164–S170, 2003.

[62] J.W. Munyan, H.V. Fuentes, M. Draper, R.T. Kelly, and A.T. Woolley. Electrically actuated, pressure-driven microfluidic pumps. *Lab on a Chip*, 3:217–220, 2003.

[63] R.H. Liu, J. Yang, R. Lenigk, J. Bonanno, and P. Grodzinski. Self-contained, fully integrated biochip for sample preparation, polymerase chain reaction amplification, and dna microarray detection. *Analytical Chemistry*, 76:1824–1831, 2004.

[64] J. Xie, Y. Miao, J. Shih, Q. He, J. Liu, Y.-C. Tai, and T.D. Lee. An electrochemical pumping system for on-chip gradient generation. *Analytical Chemistry*, 76:3756–3763, 2004.

[65] D.A. Ateya, A.A. Shah, and S.Z. Hua. An electrolytically actuated micropump. *Review of Scientific Instruments*, 75:915–920, 2004.

[66] R.H. Liu, T. Nguyen, K. Schwarzkopf, H.S. Fuji, A. Petrova, T. Siuda, K. Peyvan, M. Bizak, D. Danley, and A. McShea. Fully integrated miniature device for automated gene expression dna microarray processing. *Analytical Chemistry*, 78:1980–1986, 2006.

[67] C.R. Neagu, J.G.E. Gardeniers, M. Elwenspoek, and J.J. Kelly. An electrochemical active valve. *Electrochimica Acta*, 42:3367–3373, 1997.

[68] C. Neagu, H. Jansen, H. Gardeniers, and M. Elwenspoek. The electrolysis of water: an actuation principle for MEMS with a big opportunity. *Mechatronics*, 10:571–581, 2000.

[69] J. Ji, L.J. Chaney, M. Kaviany, P.L. Bergstrom, and K.D. White. Microactuation based on thermally-driven phase-change. In *Transducers '91*, pages 1037–1040, 1991.

[70] P.J. Bergstrom, J. Ji, Y.-N. Liu, M. Kaviany, and K.D. Wise. Thermally dirven phase-change microactuation. *Journal of Microelectromechanical systems*, 4:10–17, 1995.

[71] T. Stanczyk, B. Ilic, P.J. Hesketh, and J.G. Boyd. A microfabricated electrochemical actuator for large displacements. *Journal of Microelectromechanical systems*, 9:314–320, 2000.

[72] J. Emmelkamp. Een microdoseersysteem voor μTAS toepassingen. Master's thesis, Hogeschool Enschede, 1999.

[73] S.Z. Hua, F. Sachs, D.X. Yang, and H.D. Chopra. Microfluidic actuation using electrochemically generated bubbles. *Analytical Chemistry*, 74:6392–6396, 2002.

[74] T.K. Jun and C.-J. Kim. Microscale pumping with traversing bubbles in microchannels. In *Solid-State sensor and actuator workshop '96*, pages 144–147, 1996.

Chapter 3

Electrochemical pumping in nanochannels

This chapter presents the theoretical aspects of electrochemical pumping in nanochannels. Scaling the aqueous solutions to nanoscale dimensions has a huge impact on the electrochemical pumping process due to the low electrical currents required for electrolysis and bubble formation. Additionally, the dimensions of nanochannels also strongly affect capillary forces, gas diffusion, and hydraulic resistance. The chapter is organized with an introduction to electrolysis and charging of the electrical double layers of anode and cathode, and its effect on the electrochemical pumping. Capillary forces in nanochannels are described subsequently, followed by the gas bubble formation and gas diffusion from the electrode into the nanochannel. The effect of hydraulic resistance on bubble growth in the nanochannel is briefly described.

3.1 Electrolysis

Electrolysis was first described by Michael Faraday in his article *On Electrical Deposition*, 1834 [1], where he describes the process of water dissociation into hydrogen and oxygen gas by applying an electrical current, which he named *Electrolysis*. The electrolysis process is shown in Figure 3.1. If two noble metal electrodes are used in pure water oxygen will be formed at the anode, hydrogen at the cathode, as shown in the half reactions in equations 3.1 and 3.3 [2; 3; 4]:

$$cathode : 4e^- + 4H_2O_{(l)} \rightleftharpoons 2H_{2(aq)} + 4OH^- \tag{3.1}$$

$$E_{H_2} = 0.000 - 0.0591pH - 0.0295log(p_{H_2}) \tag{3.2}$$

$$anode : 2H_2O_{(l)} \rightleftharpoons O_{2(aq)} + 4H^+ + 4e^- \tag{3.3}$$

$$E_{O_2} = 1.228 - 0.0591pH + 0.0147log(p_{O_2}) \tag{3.4}$$

where E is the required electrical half potential for the reaction to take place and p_{H_2} and p_{O_2} the partial pressures of hydrogen and oxygen, respectively. E is dependent on the pH and the partial pressure of the produced gases.
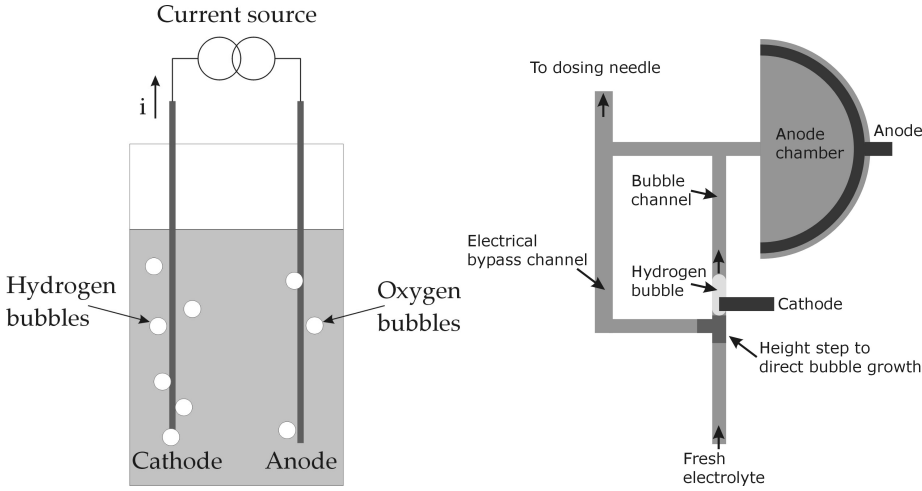
Figure 3.1: Left: Principle of bulk electrolysis. Right: Schematic of the proposed femtodosing system.

When electrolysis is performed in microfluidic systems, the distances between the electrodes is very small, ranging from several µm to mm. Since the applied potentials are relatively large (few volts), the H^+ and OH^- ions migrate in about a second to the counter electrode. Furthermore, the applied current densities are relatively small. The fast migration times and small current densities prevent large pH differences in the electrolyte, in contrast with conventional electrolysis. On the other hand, due to the capillary pressures the partial pressures of the produced gases can be much higher than in conventional systems, causing an increase in $E°$.

Section 3.2 demonstrates that in principle only an electrical current i can exist if both half reactions take place. As a consequence the minimal applied potential U over the electrodes is 1.23 V at the start of the electrolysis process with pH 7 for pure water, through the whole system and the partial pressure is still negligible. During the electrolysis process, as the pH shifts at both electrodes in opposite directions, and the partial pressures of the gases increase, $E°$ will increase, and therefore the applied voltage U will increase too.

Normally, salt is added to the electrolyte to reduce the electrical resistance of the electrolyte, see section 3.2. If the redox potentials of the salt ions are less than the redox potentials of water stated in equations 3.1 and 3.3, then the supplied electrical current i will be used first for reducing the salts. In the case of potassium nitrate KNO_3 the redox reactions of dissolved KNO_3, used throughout this manuscript, at the electrodes are shown in equations 3.5 and 3.6. Both reactions occur at the cathode and the potentials are higher than the potential stated in equation 3.1, so dissolved KNO_3 does not take part in the reaction [2].

$$K^+ + e^- \rightarrow K \quad E° = -2.93V \tag{3.5}$$

$$2NO_3^- + 2H_2O + 2e^- \rightarrow N_2O_4 + 4OH^- \quad E° = -0.85V \tag{3.6}$$
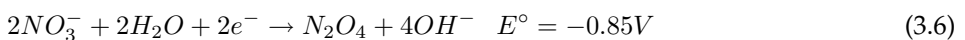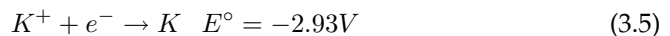
During the electrolysis process the hydrogen and oxygen reaction products are still in the dissolved phase. When the electrolyte becomes supersaturated by hydrogen or oxygen, gas bubbles can evolve. Gas bubbles formed at both electrodes results in a more complex pumping system, due to the parallel actuation. This can be avoided by choosing the electrolyte and electrode in such a way that only gas is produced at one electrode, where at the other electrode the material dissolves or grows [5]. Another way, chosen in this thesis, is to avoid the generation of bubbles by keeping the gas concentrations below the required level of supersaturation. Since oxygen is produced at a lower rate and has higher solubility than hydrogen, oxygen production can easily be avoided by sufficient enlargement of the anode and anode chamber. The volumetric increase that results from these gas bubbles is used as the hydraulic driving force for the dosing system. A schematic of the proposed femtoliter dosing system is shown in the right in Figure 3.1. The total rate of gas production q [mol/s] produced by electrolysis can be derived from equations 3.1 and 3.3 for a constant current i [A] [6]:

$$q = \frac{i}{nF} = \frac{i}{2F} \tag{3.7}$$

where F is Faraday's constant (96,485 C/mol) and n is the stoichiometric number of electrons consumed in the electrode reaction (2 for forming H_2 and 4 for forming O_2).

In the dosing system presented in this thesis only hydrogen bubbles are used for hydraulic actuation thus the cathode is the working electrode. Although oxygen is formed at the anode, it is not used for actuation, and therefore the gas production rate q is shown at the right of equation 3.7.

Normally, when electrolysis takes place in a bulk chamber as shown in Figure 3.1 the pressure in the bulk is close to atmospheric pressure. Gas bubbles evolve easily at the rate v [m^{3}s^{-1}] and the produced hydrogen bubbles can be estimated by multiplying equation 3.7 with the standard ideal molar gas volume (25 °C and atmospheric pressure) V_m (24.5 10^{-3} m^{3}mol^{-1}) [7]:

$$v = \frac{1}{2}\frac{i}{F}V_m \tag{3.8}$$

Since capillary forces inside nanochannels can reach pressures above 10 bar [8; 9], they can not be neglected and will be discussed in more detail in section 3.3. Adding the capillary pressure p_{cap} [bar] to equation 3.8 gives:

$$v = \frac{1}{2}\frac{i}{F}V_m\frac{p_{atm}}{p_{atm} + p_{cap}} \tag{3.9}$$

where p_{atm} is the atmospheric pressure.

If current pulses of amplitude i [A] and a duration of Δt [s] are applied instead of a continuous current the dosed volume ΔV during the current pulses becomes:

$$\Delta V = \frac{1}{2}\frac{i}{F}V_m\frac{p_{atm}}{p_{atm} + p_{cap}}\Delta t \tag{3.10}$$

In section 3.3 it will be shown that nanochannels with a height of 160 nm and silicon nitride walls, used in this thesis, gives capillary pressures of 7.9 bar when using pure water as liquid. Using equation 3.10 it can be calculated that the required current i is in the order of nA if the dosed volumes are in the order of 10 fL and the pulse durations are in the order of seconds. For example, a dosed volume of $\Delta V = 10$ fL and $\Delta t = 1$ s in a 160 nm tall nanochannel with capillary pressures of 7.9 bar gives:

$$i = \frac{2F\Delta V(p_{atm} + p_{cap})}{\Delta t V_m} = \frac{2 \times 96.485 \times 10 \cdot 10^{-18} \times (1 + 7.9)}{1 \times 24.5 \cdot 10^{-3}} \approx 0.7 nA \qquad (3.11)$$

This very small current i has some effects on the electrical system, which is discussed in section 3.2.

The electrical current is assumed positive for production of hydrogen gas in equations 3.1 and 3.3 where the reaction goes from left to right. A negative current reduces the amount of gas, assuming a sufficient amount of gas exists. Equations 3.9 and 3.10 can, therefore, also be used to calculate negative rate and volume decreases.

3.2   Electric model

While investigating the electrolysis process, Faraday introduced the terms electrode, electrolyte, electrolysis, anode, cathode, anion and cation in 1834. Although it has been known since the time of Volta (1793) that direct current passes through an electrode/electrolyte interface, the capacitive nature of the interface was first described by Varley (1871). Wien (1896) stated that the interface included both capacitive and resistive components. However, it was Warburg (1899) who developed the concept that the interface can be represented by a series circuit consisting of a resistance and a capacitance [10].

An electric model is now developed which consists of several effects affecting the device's operation. First, we describe the non-faradaic pathway, where the double layer capacitance is considered. After, the faradaic pathway is described with the commonly used Warburg model. In addition, a parasitic capacitance, due to the large area between the electrodes and substrate separated by a thin dielectric, is described. Finally, a model of the entire electrochemical cell is presented and an example of electrode charging time and hydrogen production is shown.

3.2.1   Double layer capacitance

The electrode/electrolyte interface according to the classical Helmholtz approach is shown in Figure 3.2, on the right. The double layer consists of two layers: the Stern, or Helmholtz, layer and the diffuse layer. The Helmholtz layer can be divided into two more layers as described by the Gouy-Chapman-Stern model [3], see the left picture in Figure 3.2. The counter ions in the Helmholtz layer are thought to be *specifically* adsorbed to the electrode surface and shield the surface charge. The locus of the electrical centers of the *specifically* absorbed ions is called the inner Helmholtz plane (IHP), which is at distance x_1 and is determined by the radius of the adsorbed ions. Dissolved ions can only approach the metal electrode to a distance x_2, normally thought to be around 10 Å. The locus of centers of these nearest dissolved ions is called the outer Helmholtz

plane (OHP). These dissolved ions are held in position by purely electrostatic forces, and thus are mobile and called *non-specifically* adsorbed. Due to the combination of diffusion and the electrostatic forces these ions are exponentially distributed from the OHP inwards the bulk solution. The thickness of the diffuse layer depends on the ionic strength of the electrolyte and the potential over the solution [11].
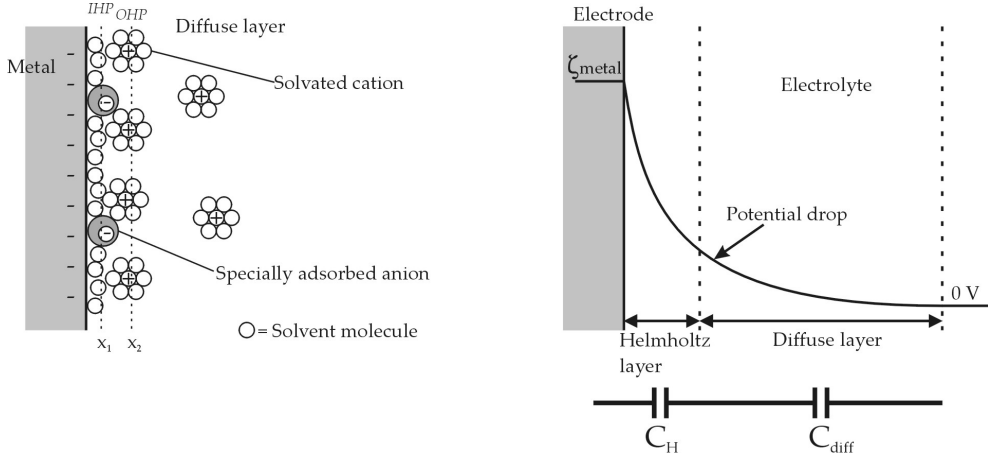

Figure 3.2: *Left: the inner (IHP) and outer (OHP) Helmholtz planes and the diffuse layer, as described by the Gouy-Chapman-Stern model, Right: electrical double layer model at metal electrodes [3].*

In the Gouy-Chapman-Stern model two capacitances can be associated with this double layer. The capacitance in the Helmholtz layer is called the Helmholtz capacitance C_H. C_H typically has a value of 10-40 µF [3]. Obviously, the diffuse layer has a capacitance called diffuse capacitance C_{diff}. C_{diff} strongly depends on the applied potential and the ionic strength of the solution, but normally C_{diff} is much larger than C_H. The total capacitance of the double layer C_{dl} is the sum of two serial capacitances C_H and C_{diff}:

$$\frac{1}{C_{dl}} = \frac{1}{C_H} + \frac{1}{C_{diff}} \tag{3.12}$$

The composite capacitance C_{dl} shows a complex behavior and is governed by the smaller of the two components. At larger electrolyte concentrations C_{diff} becomes so large that it no longer contributes to C_{dl} and one sees only the constant capacitance of C_H. So, according to the Gouy-Chapman-Stern model a characteristic feature of metal/aqueous electrolyte interfaces is their high capacity, which ranges between 10 and 40 µF/cm^2, where 20 µF/cm^2 for common values [3; 12].

The pathway through the double layer capacitance in the electrode/electrolyte interface is generally called the non-faradaic pathway. Another pathway, the faradaic pathway, is discussed in the next section.

3.2.2 Warburg model and Faradaic resistance

According to the Warburg model [13], for low current density, the faradaic pathway of the electrode/electrolyte interface can be represented by a series circuit consisting of resistances and capacitance: C_w, R_w and R_{sol}. C_w and R_w represent the Warburg capacitance and resistance and R_{sol} the electrical resistance of the solution, see Figure 3.3. In this model R_w and polarization reactance, $X_w = 1/j\omega C_w$, both decrease as $1/\sqrt{f}$ with increasing frequency f. This model predicts an ever-increasing impedance as the frequency approaches 0 Hz, which is, of course, the case for dc-systems like the described system. However, such an equivalent circuit predicts an infinite impedance once C_w is
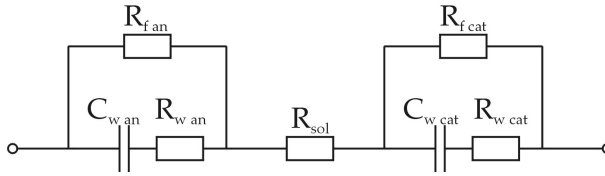

Figure 3.3: *Electrical Warburg model of the electrode/electrolyte/electrode interface, where 'an' and 'cat' represent the anode and cathode, respectively [10].*

charged for direct current, a situation that is not consistent with experimental evidence when electrolysis takes place and current follows a direct pathway through the electrode/electrolyte interface. Once the potential over an electrode/electrolyte interface has exceeded the required electrochemical half-potential, one can provide a path for direct current by placing a resistance in parallel with the Warburg series capacitance and resistance. The resistive element that represents the ability of the electrode/electrolyte interface to pass direct current is known as a faradaic resistance [10; 14].

According to Mayer *et al.* [10] the zero current Faradaic resistance equals 30.3 kΩ for a 0.1 cm^2 platinum electrode in 0.9% NaCl solution at room temperature. For systems with very small electrodes the Faradaic resistance (R_f) becomes very large, up to 6.06 GΩ for electrodes of 50 μm^2. R_f appears to be current density dependent, where the resistance is increasing with increasing current density [10], indicating that the influence of the faradaic pathway is decreasing during charging of the electrical double layer. As the Warburg impedance has an infinitely high value for dc-current when C_w is fully charged, we can take the Warburg pathway out of our electrical model and R_f is the only resistance in the electrode/electrolyte interface. Therefore, one can state that, when applying a dc-current and the double layer capacitance is fully charged, all the current at the electrode/electrolyte interface is used for the electrolysis reaction.

3.2.3 Parasitic capacitance

The direct capacitive coupling between the electrode wires and the silicon substrate is represented by the parasitic conductance C_{par} and can be calculated using the surface area of the metal/substrate interface, the thickness of the SiN isolation layer and the permittivity of the PECVD SiN isolation layer, and is equal to [15]:

$$C_{par} = \frac{\epsilon_0 \epsilon_{r,SiN} A_{par}}{d_{par}} \tag{3.13}$$

where ϵ_0 is the permittivity in vacuum, $\epsilon_{r,SiN} \approx 7.0$ [16] is the relative permittivity of silicon nitride, A_{par} is the area between the conducting metal of the electrodes, electrode wiring, electrode connection pads and the substrate, and d_{par} is the thickness of the silicon nitride (SiN) isolation layer. As there are two electrodes in the system, both C_{par}'s can be placed in series. As the C_{par}'s of the cathode and anode are comparable, the replacing C_{par} of the whole system can be seen as a capacitor with a d of two times the SiN layer thickness. Therefore, C_{par} is placed in the electrical model in parallel with the other components, shown in Figure 3.2. When using small currents and large electrode wire areas, the capacitance can become big and have a large effect on the charging time of the double layer, as will be shown in Section 3.2.6.

3.2.4 Cell constant

As electrons in a metal result in electrical conductivity, so do ions in an electrolyte solution. This conductivity is expressed by the specific conductivity of an electrolyte, κ_{sol} [S/m]. It depends on both the concentration and the mobility of the dissolved ions. The equivalent conductivity of an electrolyte can be calculated by adding the product of the concentrations, C_i [mol/m³], and ion conductivities, λ_i [Sm²/mol], of all the individual types of ions, see equation 3.14:

$$\kappa_{sol} = \sum C_i \lambda_i \tag{3.14}$$

The solution resistance is inversely proportional to the conductivity and expressed as :

$$R_{sol} = \frac{1}{\kappa_{sol}} K_{cell} \tag{3.15}$$

$$K_{cell} = \frac{d_{cell}}{A_{cell}} \tag{3.16}$$

where K_{cell} is the cell constant, d_{cell} the distance through the electrolyte and A_{cell} the cross-sectional area of the electrolyte in the channel [3; 15].

When K_{cell} reaches very high values, as is the case for long nanochannels, R_{sol} goes to very high values. These high values cause a large potential difference over the solution when currents through the solution are applied. When the solution is placed in a electrode/electrolyte/electrode system, it causes an increased potential over the two double layers. This increased potential will cause C_{par} to be charged to a higher potential difference, and increased charging times will be the result.

As the ions will migrate due to the dc potential, resulting from the applied dc current, the ion distribution will become less homogeneous after time, and therefore the κ_{sol} decreases and R_{sol} increases in time. When the electrolysis starts new ions are formed, which can decrease R_{sol}.

3.2.5   Cell capacitance

The direct capacitive coupling between the two electrodes is represented by the cell capacitance C_{cell} and can be calculated using the cell constant (equations 3.15 and 3.16) and the permittivity of the solution, and is equal to

$$C_{cell} = \frac{\epsilon_0 \epsilon_{r,sol} A_{cell}}{d_{cell}} \qquad\qquad (3.17)$$

where $\epsilon_{r,sol} \approx \epsilon_{r,water} = 80$ [17], A_{cell} is the functional area of the electrodes facing each other and d_{cell} is the distance between the electrodes. As C_{par} and C_{cell} are placed parallel of each other, and comparing C_{par} with C_{cell}, we can state that $A_{cell} \ll A_{par}$ and $d_{cell} \gg d_{par}$, and therefore we can neglect the effect of C_{cell} with respect to C_{par}.

3.2.6   Electric model

The electric model is shown in Figure 3.4. In the model of the electrolysis system both electrode/electrolyte interfaces are depicted as the double layer capacity C_{dl} parallel with the faradaic resistance R_{far}. The double layer capacitance C_{dl} is represented as C_w in the Warbug model. The faradaic resistance is placed to make a direct electrode/electrolyte pathway possible. This pathway only exists when the potential over C_{dl} exceeds the required E° of the electrochemical half-reaction and electrolysis can occur. These electrode/electrolyte interfaces are in series with the resistance of the electrolyte R_{sol}. The parasitic capacity C_{par} placed parallel to the other components. All the other resistances and capacitances are neglected, i.e. the wire resistances, the electrode/electrode cell capacitance and the Warburg impedance R_w as they are expected to have negligible influence on the system. The capacitance between the electrical wires
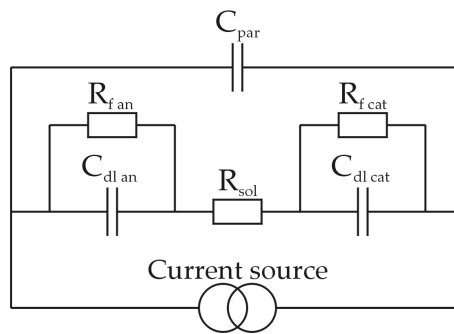

***Figure 3.4:** Electrical model of the electrode/electrolyte interface.*

and the silicon bulk material in the wafer is not taken into account as this is very small and has a very short RC-time constant. Also the wire resistances are negligible because they are much smaller than R_{sol}.

Example: influence of charging time on hydrogen production

Consider the dosing system in Figure 3.1 (right) with channel cross-sectional area of 1.6×10^{-12} m^2 and length of 600 µm with an electrolyte with 0.1 M KNO$_3$. The model shown in Figure 3.4 is used to estimate the charging time of the electrodes. The faradaic resistances $R_{f\ an}$ and $R_{f\ cat}$ are ignored during the charging process.

The charging time of C_{dl} is calculated in the following example. Assume an electrical current of 2 nA, a cathode area of 50×10^{-12} m^2 (5×10 µm^2), an anode area of 6×10^{-9} m^2 (bigger to suppress oxygen bubble formation) and C_{dl} = 20 µF/cm^2. The capacitance of the cathode to be charged for hydrogen evolution is 10 pF, and for the anode this number is 1.2 nF for oxygen evolution.

Electrolysis at one electrode starts when the potential over C_{dl} is more than E°, neglecting the overpotential effect, and current can flow. When using an electrolyte with pH=7 and without any dissolved hydrogen and oxygen, the potential at the cathode equals -0.414 V (Equation 3.1), and for the anode this potential equals 0.814 V (Equation 3.3). Without any dissolved oxygen and hydrogen, and with equal pH at both electrodes, the potential between both electrodes remains 1.228 V. For reasons mentioned earlier we neglect the pH differences in the electrolyte and state that the whole electrolyte has a neutral pH 7. For the partial gas pressure we assume that the capillary pressure equals 4 bar, and thus the partial hydrogen pressure equals the capillary pressure plus the atmospheric pressure, giving a pressure of 5 bar. The partial oxygen pressure is much smaller and will be neglected. We find that Ean at the anode equals 0.81 V and E_{cat} at the cathode equals -0.58 V, giving a total value for E = 1.39 V.

At the start of the electrolysis process, when no bubble has been formed and blocking the bubble channel, the electrical by-pass channel and the bubble channel connect the two electrodes, resulting in a total cross-sectional are of 3.2×10^{-12} m^2. Using equations 3.14, 3.15 and 3.16 gives $R_{sol} \approx 141$ MΩ. Using $U_{sol} = i \times R_{sol}$ gives U_{sol} = 0.28 V.

With C_{par} = 0.6 nF, $C_{dl\ an}$ = 1.2 nF, $C_{dl\ cat}$ = 10 pF and a charging current i = 2 nA, we estimate charging times of 0.18 s to start hydrogen production and 0.90 s to start oxygen production.[1]

The required additional time before all applied current is used for hydrogen can be calculated using the RC-time τ of a very simple RC-circuit, with R_{sol} and C_{par} parallel. This extra time is approximately $5 \times \tau \approx 0.42$ s ($> 99\%$ of all applied current is used for hydrogen production), resulting in a total time of ~1.32 s. Concluding, the hydrogen production starts after 0.18 s, but it takes till 1.32 s before all applied current is used for

---

[1]First, the parasitic capacitance C_{par} is estimated, using an electrode/SiN interface area A_{par} of 10^{-5} m^2 and a d_{par} of two times SiN layer thickness of 500 nm, as 0.6 nF. If R_{sol} does not change because of migration of the K$^+$ and NO$_3^-$ ions, the required charging times before electrolysis can take place are estimated using $U = Q/C$ and $Q = i\Delta t$ [18]. Before hydrogen can be produced, the potential over the double layer at the cathode needs to overcome -0.58 V, requiring a charge of 5.8 pC. Since $C_{dl\ an}$ and $C_{dl\ cat}$ are placed in series, the potential over $C_{dl\ an}$ equals 5.8 pC/1.2 nF = 0.0048 V, the potential over $C_{dl\ res}$ therefore equals 0.585 V. Because $C_{par} \gg C_{dl\ res}$, the large value of R_{sol}, one can state that $U_{par} \gg U_{sol}$ and $U_{par} \approx U_{dl\ res}$ = 0.585 V, therefore, $Q_{par} \approx 0.353$ nC. Since $Q = i \times \Delta t = Q_{par} + Q_{dl\ res}$, then $\Delta t \approx= 0.18$ s. Finally, the required time before hydrogen production starts will be around 0.18 s. As the anode has not reached the required electrochemical half-potential, oxygen production has not started yet. Similar, the time required to achieve oxygen production can be calculated, and equals 0.90 s.

hydrogen production. For these calculations a lot of assumptions have been made, that can lead to large differences compared to measured values.

3.3 Capillary forces

As mentioned earlier capillary forces are of great importance when working with nano-channels. Capillary forces drive the liquid into the channel, causing a pressure in the liquid, the capillary pressure. When a watery liquid is in a channel with hydrophilic walls, such as silicon nitride, the liquid is attracted by the wall due to physical and chemical forces at the liquid/solid interface. The capillary force can be calculated using the Young-Laplace equation, which relates the pressure drop across a liquid meniscus to its curvature [9]:

$$p_{cap} = p_L - p_V = \gamma \left(\frac{1}{r_1} + \frac{1}{r_2} \right) \tag{3.18}$$

where p_{cap} is the pressure difference between the liquid side (at p_L) and the vapor side (at p_V) of the meniscus, γ is the surface tension of the liquid, and r_1 and r_2 are the radii of curvature of any two normal sections of the meniscus perpendicular to one another [9; 19].

In nanofluidic systems the curvatures taken are usually in the direction of the channel height (r_h) and the direction of the channel width (r_w). The meniscus curvature is related to channel dimensions height (h) and width (w):

$$r_h = \frac{h}{2cos\theta} \tag{3.19}$$

$$r_w = \frac{w}{2cos\theta} \tag{3.20}$$

where θ is the contact angle of the liquid at the channel wall, see Figure 3.5.

In flat nanofluidic channels the width is much larger compared to the height, $r_w \gg r_h$, thus the portion of the capillary pressure caused by the channel width is much less than the capillary pressure caused by the channel height. Often, in such cases the influence of the channel width on the capillary pressure is neglected and combining equations 3.18 and 3.19 gives:

$$p_{cap} = \frac{2\gamma cos\Theta}{r} \tag{3.21}$$

When bubbles exist in filled nanochannels the pressure inside the bubbles can be either atmospheric pressure, when the channel is not completely filled (i.e. drying), or atmospheric pressure added with the capillary pressure, when the capillary is completely filled and the meniscus of the liquid/gas interface outside of the channel is significantly large so the pressure rise caused by the curved meniscus is negligible, see Figure 3.6. Negative pressures, as shown in the top channel in Figure 3.6, down to -17 ± 10 bar have been demonstrated by Tas et al. [9].

From equation 3.21 it is clear that the capillary pressure can be altered by decreasing the surface tension by adding a detergent, or by altering the channel height.
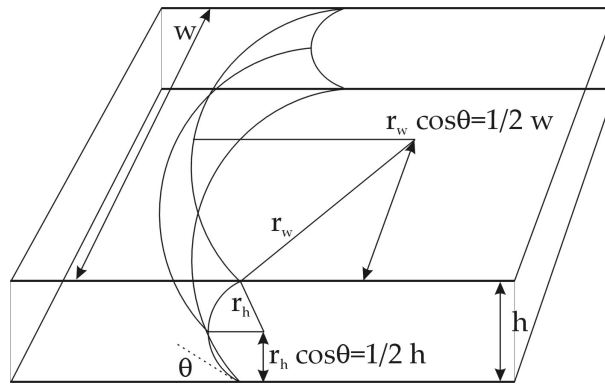
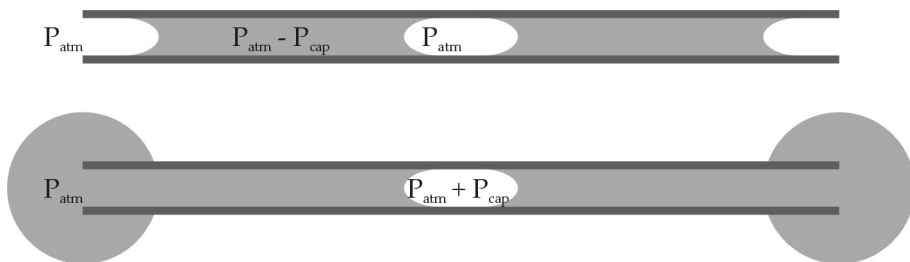**Figure 3.5:** *Bubble radius related to channel height and contact angle.*

Figure 3.6: *Bubble pressure inside nanochannels in a drying channel (top) and a completely filled channel (bottom).*

3.4   Gas bubble formation

The femtoliter dosing system uses gas bubble growth inside a nanochannel as the driving force for dosing liquids. The gas bubble functions as a piston pushing the liquid through the nanochannel. Before a gas bubble evolution can be used the gas bubble should meet three requirements:

1. Controlled nucleation;

2. Controlled evolution;

3. Minimal leakage along the bubble sides.

3.4.1   Gas bubble nucleation

Bubble nucleation is the process of 'birth' of a bubble. Gas is produced by electrolysis at the electrode surface. Before nucleation can take place locally, the electrolyte needs to be saturated with gas. At the cathode, the working electrode of the dosing system, hydrogen is formed. As shown in section 3.1, the production of hydrogen is directly

proportional to the applied current. So, at the electrode surface the production concentration of hydrogen as a function of the electrode area is directly proportional to the current density. Produced gas will diffuse away from the electrode due to the hydrogen concentration gradient. If the production exceeds the loss because of the diffusion, at a certain moment local saturation of the electrolyte with hydrogen will occur. Because of the capillary pressure inside the channel the saturation level will be much higher than in conventional bulk solutions, where the bubbles need to overcome atmospheric pressure.

Furthermore, equation 3.18 shows that for bubbles smaller than the channel height, the pressure inside the bubble will be even higher than the capillary pressure plus the atmospheric pressure. As a result the needed hydrogen concentration has to exceed the saturation level: supersaturation is needed. Two different forms of nucleation can occur:

- Homogeneous nucleation

- Heterogeneous nucleation

According to homogeneous nucleation theory, nucleation results from the expansion of a spherical void inside the liquid with a radius R subjected to a negative pressure p [20; 21], which will not be the case in our system. Therefore, heterogeneous nucleation theory will be used. Heterogeneous nucleation takes place at the solid/liquid interface in the channel, so at the channel wall, electrodes or free flowing solid particles. The nuclei are assumed to be stabilized in small crevices allowing a modification of the interface curvature [22; 23]. A larger interface curvature gives a lower internal pressure, and thus is energetically favorable. For a given gas concentration, the stabilization depends on the wetting properties of the liquid on the solid surface and the geometry of the crevices [20]. As the crevices reduce the energy needed for forming the meniscus of the bubble the heterogeneous nucleation is much easier and more stable to achieve. It is assumed that the nucleation precess is heterogeneous in case of electrolysis, as the gases are produced at the electrode surface.

Crevices, or nucleation points, can be natural (little scratches/imperfections), or artificial (ditches/holes/transitions), to control the nucleation. In nanochannels, the dimensions of the structures are nanometer scale and are assumed to be small enough for acting as nucleation points. Figure 3.7 show two possible nucleation points for electrolysis in nanochannels: natural scratches at the electrode surface and the transition between channel wall and electrode.
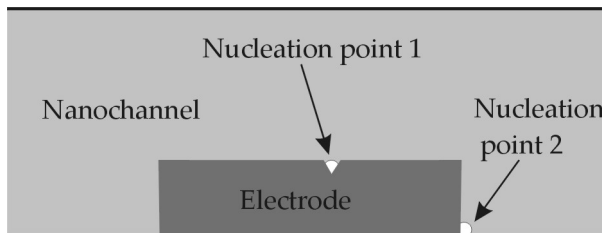

Figure 3.7: *Natural (point 1) and artificial (point 2) nucleation points at the electrode.*

Before nucleation takes place the liquid must become supersaturated, due to the high energy level needed for bubble formation. In heterogeneous nucleation the liquid will usually be less supersaturated than in cases of homogeneous nucleation. Shibata reported that the concentration of molecular hydrogen on the platinum electrode, as revealed by measurement of the decay curve of the concentration overpotential of hydrogen molecules, was found to be 0.116 mol/L at the current density of 300 mA/cm^2, corresponding to a degree of supersaturation of 160-fold [24]. Supersaturation of hydrogen in bulk produced by platinum electrodes has been investigated further by Vogt and shows that supersaturation increases with increasing current density [25; 26]. Kikuchi et al. studied the concentration of hydrogen in nanobubbles formed by electrolysis in different solutions, where he shows that supersaturation is depending on the ionic strength of the solution [27]. Also the correlation between electrode surface roughness, current density and supersaturation has been reported by Kikuchi [28] and Shibata [29]. Depending on the electrode surface supersaturation levels of hydrogen of 165-fold (a smooth surface), 120-fold (platinized surface) and 23-fold (mechanically ground) have been reported. For oxygen supersaturation levels of 70-fold have been reported [30].

Although supersaturation levels can be very high and reproducible by controlling solution, surface roughness and current density, it is very difficult to predict. Therefore, bubble nucleation is also difficult to predict.

3.4.2   Gas bubble evolution

In nanochannels the bubble evolution after nucleation has three stages:

1. 3-dimensional stage

2. 2-dimensional stage

3. 1-dimensional stage

Once the nucleation has taken place the bubble can evolve as in bulk till the diameter of the bubble will be equal to the channel height. This first stage we call the 3-dimensional or 3-d stage, as the bubble grows in three dimensions. The pressure inside the bubble is very high, but decreases exponentially with increasing size. This stage looks very similar to conventional bubble evolution, but diffusion processes will differ more and more from conventional theory of electrolysis in bulk when the bubble size is increasing. The diffusion in nanochannels will be discussed in section 3.5. This stage is the shortest stage during evolution.

In the 2-d stage the bubble can expand only in the direction of channel width and channel length. Since the pressure inside the bubble is controlled mainly by the smallest bubble radius, the channel height (see equation 3.18), the bubble pressure will decrease exponentially until half of its original pressure for infinite width. Most area of the bubble is in contact with the top and bottom channel walls, thus diffusion through the bubble meniscus will increase less than in 3-d bubble growth as the relative diffusion area (in relation to the bubble volume) gets smaller.

The last stage, and by far most important stage in electrolysis in nanochannels is the 1-d stage. In this stage the bubble has blocked the channel and can expand only in the direction of the channel. The pressure inside the bubble remains approximately constant, or even increases due to hydraulic resistance of the liquid pushed through the

nanochannel caused by the piston effect of the bubble. The diffusion of gas out of the bubble into the liquid will stay approximately constant as the diffusion area is limited to the cross sectional area of the nanochannel. So, in contrast with bubbles in bulk solution, the volume of the bubble in a nanochannel will decrease very slow after stopping the gas production.

The three stages have been plotted in Figure 3.8 using equations 3.18, 3.19 and 3.20. It is clear that the pressure drop over the bubble meniscus in bulk continues to decrease exponentially with increasing volume, and that the pressure drop in the 2-d stage and 1-d stage are similar as the channel height is the limiting factor. The graph is calculated with a channel height of 160 nm, a channel width of 2 μm, a contact angle of 0 ° assuming a very hydrophilic surface, and a surface tension of that of water [0.073 N/m] [2].
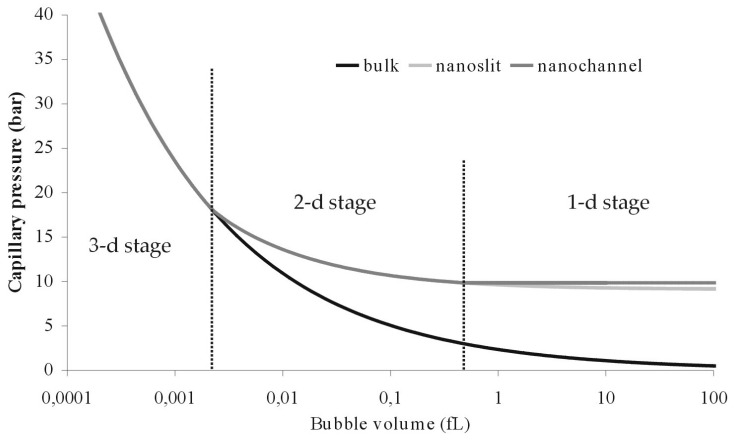

Figure 3.8: *Plot of the internal bubble pressure during the three stages of bubble evolution inside a nanochannel. The development of the pressure drop over the bubble meniscus of a bubble inside a nanochannel is compared to that of bubbles inside a nanoslit and bulk. In this calculation the channel height is 160 nm, channel width is 2 μm, contact angle is 0 ° and surface tension is 0.073 N/m (surface tension of water) [2] Though we use wider channels in this thesis, 2 μm wide channels are chosen to show the difference between 2-d and 1-d stage better. Equations 3.18, 3.19 and 3.20 have been used for the calculation.*

It is clear that the existence of very small bubbles, in the nanometer range, requires a large internal pressure. One would expect that such small bubbles can not exist under normal circumstances and will dissolve. Though, heterogeneous nanobubbles do exist. Why these nanobubbles do not dissolve is not fully understood [20].

3.5   Gas diffusion

Gas diffusion plays an important role in the femtoliter dosing system. Gas concentration gradients will occur within the liquid phase before nucleation as well as between the liquid and the gas phase after nucleation. Therefore, two different diffusion systems will occur during bubble formation. These two systems, diffusion before and after nucleation are discussed in this section.

3.5.1   Gas diffusion before nucleation

During electrolysis dissolved gas is produced at the electrode surface, and therefore the concentration of dissolved gas at the electrode surface is higher than elsewhere in the channel and the gas will diffuse from the electrode into the channel (before a bubble has been formed) or into the channel and toward the bubble meniscus (after nucleation of the bubble). Figure 3.9 schematically shows the diffusion at an electrode before nucleation. Some theoretical basis is necessary to understand the bubble behavior during and after electrolysis and to control the bubble size.
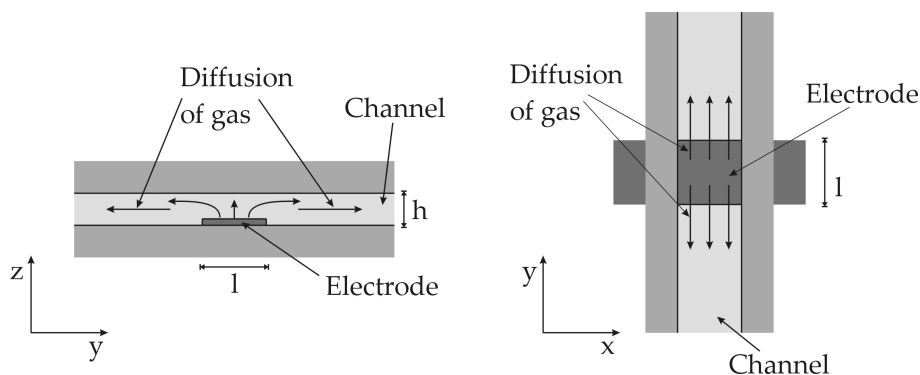

Figure 3.9: *Schematic top view of the diffusion at an electrode inside a nanochannel before bubble nucleation.*

Solving the diffusion in three dimensions is very complex. Some simplifying assumptions have to be made to calculate the concentration (c) [mol/m³]. We assume the current from the electrode into the electrolyte is uniformly distributed over the electrode surface. The plane electrodes produce gas at a constant rate due to a constant current density ($J = \frac{i}{A}$). No convection is considered. The nanochannel has a very limited height and negligible to the channel width and length. Therefore, the diffusion in z-direction (perpendicular to the electrode surface) is extremely fast and the diffusion length $\sqrt{2Dt} \gg h$ (channel height), then the concentration of dissolved hydrogen is assumed to be constant in z-direction above the electrode. Therefore, the concentration gradient in z-direction is neglected. Since hydrogen is formed at the electrode, the hydrogen concentration above the electrode increases and a concentration gradient in y-direction (i.e. in the direction of the channel) between the electrode surface and the channel will be formed. This means that the diffusion can be considered in only the

y-direction, so from the electrode channel inwards. This means that the diffusion will be one dimensional. This 1-d diffusion will be, of course, much slower than 3-d diffusion, where diffusion is in all directions. Next, at the start of the electrolysis process we assume the electrolyte does not contain any dissolved gas, so $C_{(y,0)} = 0$.

Electrode length influence

After the electrolysis process has started the gas concentration above the electrode is rising and gas will diffuse away from the electrode into the channel, as showed in Figure 3.9. With all these assumptions the diffusion into the channel can be described by the Fick's second law in one dimension [31; 15]:

$$\frac{\partial C_{(y,t)}}{\partial t} = D \left(\frac{\partial^2 C_{(y,t)}}{\partial y^2} \right) \tag{3.22}$$

where $C_{(y,t)}$ is the concentration of dissolved gas at plane (y) [mol/m] and D [m^2/s] the diffusion coefficient of the dissolved gas molecules. Attention should be paid that in this chapter $C_{(y,t)}$ is a concentration in mol/m, and therefore it should be divided by the area of the plane it is working on to get the concentration in mol/m^3. A solution for equation 3.22 is given by [15]:

$$c = \frac{N}{2\sqrt{\pi D t}} e^{-y^2/(4Dt)} \tag{3.23}$$

Given the initial amount N of the substance set in an infinitely thin plane at $y = 0$ and the value of the diffusion coefficient, one can calculate the concentration at any position and time.

This equation is not completely valid when the electrode surface is perpendicular to the channel direction, because there is no plane at $y = 0$ containing the initial amount of hydrogen, as can be seen in Figure 3.9. When a planar gas evolving electrode inside a nanochannel is used gas is built up over the length of the electrode and not in a single y-position. Simulations shown in Figure 3.10, show that the concentration profiles above 10 μm long electrodes is after 10 ms already comparable to ideal cases where all gas is released at a single plane, as described by equation 3.23. For these simulations, equation 3.24 has been used, derived from 3.23:

$$C_{(y)} = \sum_{i=0}^{n-1} \frac{\frac{1}{n}N}{2\sqrt{\pi D t}} e^{-(y+(\frac{i}{n} - \frac{1}{2}n)l)^2/(4Dt)} \tag{3.24}$$

where $n = 41$ and l is the electrode length. Figure 3.10 shows the normalized gas concentration 10 ms after a certain amount of hydrogen has been produced at $t = 0$, at electrode surfaces of 0, 10 and 50 μm length. In this graph the concentration profile of the 0 μm long electrode after $t = 10$ ms is standardized such that $C_{(y=0)} = 1$, to which the concentration profiles of the 10 and 50 μm long electrodes are compared. Thus, these profiles show the relative hydrogen concentration profiles of different electrode lengths at a short moment after a certain amount of gas was released at the electrode surface. As the diffusion distance in z-direction is much smaller than in y-direction, it is assumed
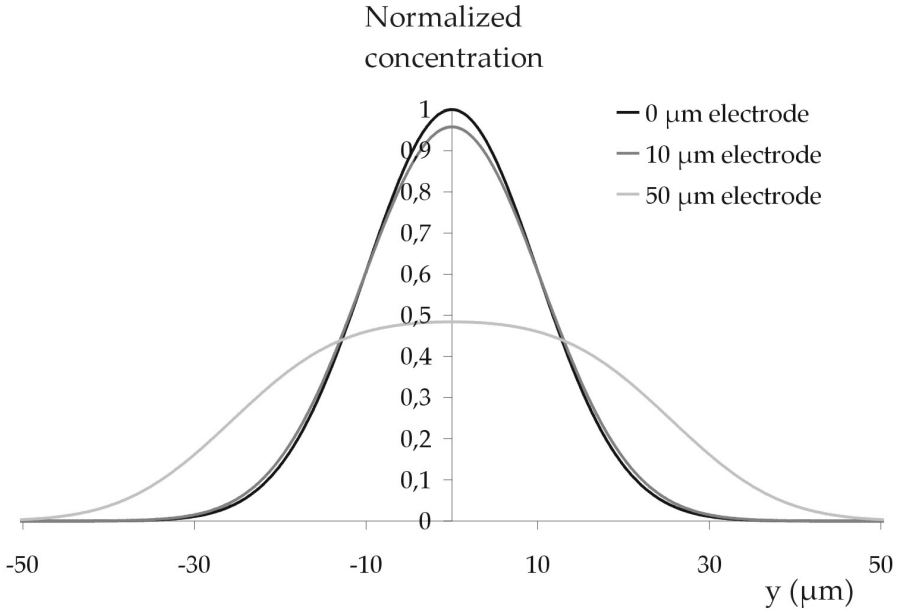
Normalized
concentration

Figure 3.10: *Plot of the normalized concentration profiles after $t = 10$ ms of different electrode lengths. At $t = 0$ gas was released equally distributed over the electrode surface. Gas diffusion only in the y-direction, and no concentration gradients in x- and z-direction were assumed. $C_{(y=0)}$ of the profile with electrode length = 0 is normalized to 1, all other values are plotted with respect to these values.*

that there is no concentration gradient in z-direction. Based on these graphs we assume the effect of the electrode length of 10 µm is very small on the concentration distribution, and therefore, the electrode length is negligible and equation 3.23 is used.

Constant gas production influence

Similar to the effect of the electrode length on the gas distribution in the nanochannel, there is the effect of a continuous gas evolving system, where gas is produced at a constant rate due to a constant current, and therefore N, the total amount of gas in the system present, is not constant, but increases in time. From section 3.1 it was shown that N is:

$$N = q \cdot \Delta t = \frac{i \Delta t}{2F} \tag{3.25}$$

where q [mol/s] is the gas production rate, Δt [s] is the time duration for the applied current i [A] and F is the Faraday constant (96485.3 C/mol) [7].

Figure 3.11 gives two concentration profiles through the nanochannel just before the
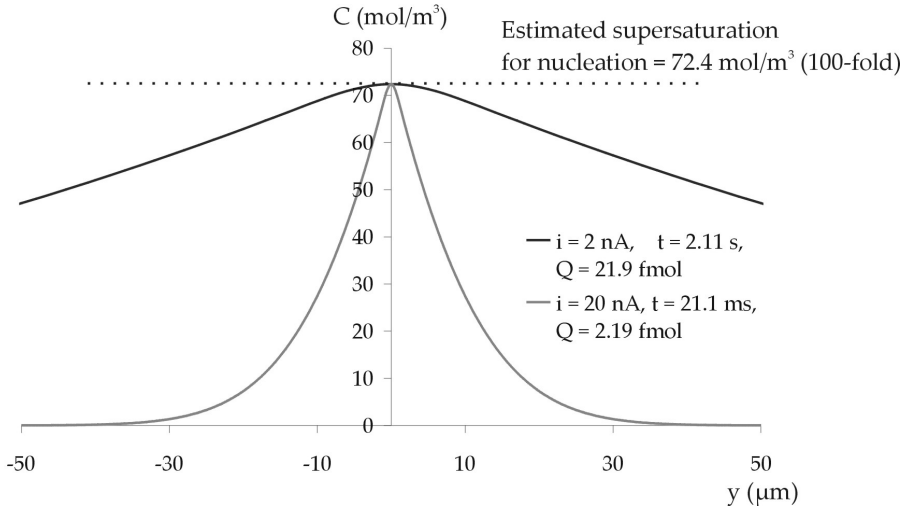
Figure 3.11: *Two concentration profiles at the electrode surface where the maximum concentration reaches the estimated required 100-fold supersaturation level for bubble nucleation. Different electrolysis currents will have different nucleation times. Long nucleation times result in larger initial bubble volumes compared to bubbles formed with shorter nucleation times because more gas has been produced.*

estimated nucleation takes place, calculated with equation

$$C_{(y,t)} = \frac{i \delta t}{4Fhw} \sum_{i=1}^{n=400} \frac{1}{\sqrt{\pi D \frac{it}{n}}} e^{-y^2/(4D\frac{it}{n})} \tag{3.26}$$

where h is the channel height and w the channel width. The used parameters are: $D = D_{H_2}$ in 0.1 M KNO_3 = 5.0 $\times 10^{-9} m^2 s^{-1}$ [32], $C_{(y,t)} = C_{saturation}$ of H_2 in water = 7.24 $\times 10^{-4}$ mol/L [33], electrode length = 0, channel width = 10 µm , channel height = 160 nm, applied current $i = 2$ nA and the estimated required supersaturation = 72.4 mol/m^3 (100-fold), approximately in agreement with the supersaturation level found for current densities of 1000 A/m^2 (100 nA/100 µm^2) [24]. In fact, the applied current density is less (20 A/m^2 for i=2 nA and 200 A/m^2 for i=20 nA), but the gas concentration will be much higher than in normal bulk situations because of decreased diffusion in nanochannels.

It is clear that the initial current is of significant importance in the nucleation time (i.e. the time between the onset of the electrolysis and bubble nucleation) and the initial bubble volume. The nucleation time is inversely proportional to the square of current and the gas produced prior to nucleation is inversely proportional to the current.

3.5.2 Gas diffusion after bubble nucleation

When a bubble has formed the curvature of the meniscus causes the diffusion direction not only to be in the y-direction, but also x-direction as the width of the channel can not

be neglected. This effect is assumed to be very small and for the sake of simplicity it will be neglected. No concentration gradient in z-direction is assumed as the channel height is extremely small and the diffusion layer is established very quickly.

The hydrogen concentration at the bubble surface is approximately equal to the saturation concentration of hydrogen [25]. One can assume that all supersaturated gas at the bubble surface will diffuse into the bubble. Just after nucleation there will be a steep concentration gradient toward the bubble and fast bubble growth is expected till all supersaturated gas is diffused into the bubble or further into the channel, and therefore the amount of gas dissolved N is decreasing in time, see Figure 3.12.
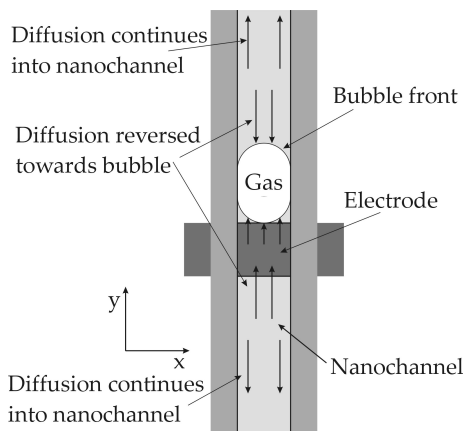

Figure 3.12: *Diffusion directions after bubble nucleation.*

Figure 3.13 shows the simulated decrease of dissolved gas after nucleation (electrical current before nucleation is 2nA, current stops at nucleation), where the amount of dissolved gas at a certain time (Q_t) is compared to the original amount of dissolved gas at nucleation, $t_{nucleation}$, (Q_0). The simulated graph of the dissolved gas decrease after $t_{nucleation}$ with $i = 20$ nA is simulated, only 100 times shorter. The graph ends exactly at $t_{equilibrium}$, the moment there is no supersaturated gas anymore, and no diffusion across the bubble meniscus occurs. The concentration profiles at $t_{equilibrium}$ for bubbles formed with $i = 2$ nA and $i = 20$ nA are shown in Figure 3.14. In Figure 3.13 it can be seen that at $t_{equilibrium}$ about 14% of the original dissolved gas is still in solution and is diffused into the channel. So, about 86% of the gas produced before $t_{nucleation}$ diffuses into the bubble when the electrical current is stopped at $t_{nucleation}$. And already about 50% of the produced gas has diffused into the bubble after 1.2% of $t_{equilibrium}$-$t_{nucleation}$. These percentages will be higher than in conventional bulk electrolysis where volume of the solution is proportional to the cube of distance compared to distance only for nanochannels. Because of this third power volume increase in bulk the concentration gradient decreases faster than in nanochannels. As a result, more gas is dissolved in bulk with a concentration below the saturation concentration, and therefore less gas will be able to diffuse into the bubble. Also, as 3-d diffusion in bulk is much faster than 1-d diffusion in nanochannels, the nanochannel bubbles will have a much slower decrease rate. Also, of course, the limited gas/liquid interface of nanochannels bubbles
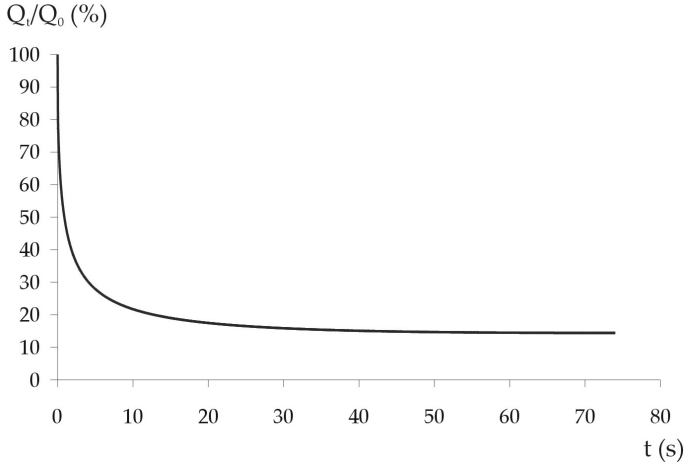
Figure 3.13: *Simulated decrease of dissolved gas after nucleation (Q_t) compared to the amount of dissolved gas at nucleation (Q_0). Applied current $i = 2nA$ and nucleation occurs at supersaturation of 100-fold.*

decreases the diffusion of gas out of the bubble. This results in a much more stable bubble volume.

The graph in Figure 3.14 is created using the following simulations. First, $C_{(y,t)}$ is simulated as described earlier. Second, the half of the symmetric concentration profile is taken, and further simulations are performed on this half without further gas production (i.e. the half facing the channel, or the half facing the electrode with applied current switched off). The channel is divided in 280 equal length distances δy, where $70 \times \delta y$ lie within the bubble (25%) and $210 \times \delta y$ are outside the bubble (75%). Now, the new $C_{(y,t)}$ is simulated using equations

$$C_{(y,t)} = \sum_{i=1}^{n=70} C_{sat} \tag{3.27}$$

$$C_{(y,t)} = \sum_{i=1}^{m=70} \sum_{j=1}^{n=280} \frac{N_{(j\Delta y,t)} - C_{sat}\Delta V}{const} e^{-(i\Delta y - j\Delta y)^2/(4D\Delta t)} \tag{3.28}$$

$$C_{(y,t)} = \sum_{i=71}^{m=280} \sum_{j=1}^{n=280} \frac{N_{(j\Delta y,t)}}{const} e^{-(i\Delta y - j\Delta y)^2/(4D\Delta t)} \tag{3.29}$$

where $N_{(y,t)} = C_{(y,t-\Delta t)}\Delta V$, $\Delta V = \Delta y \times$ cross-sectional area of the channel, $\Delta y = y/280$, $\Delta t = t/1500$, $C_{sat} = 0.724$mol/m^3 and $const = 2\sqrt{\pi D \delta t}$. The variable y is chosen such that the simulated concentration profile fitted in y, and t was exactly the time needed to achieve the equilibrium between gases diffusing in and out of the bubble, as shown in Figure 3.14. The total amount of dissolved gas $Q_{(t)}$ is the sum of $C_{(y,t)}$ at y out of the bubble multiplied with ΔV. The graph in Figure 3.13 shows the decay of
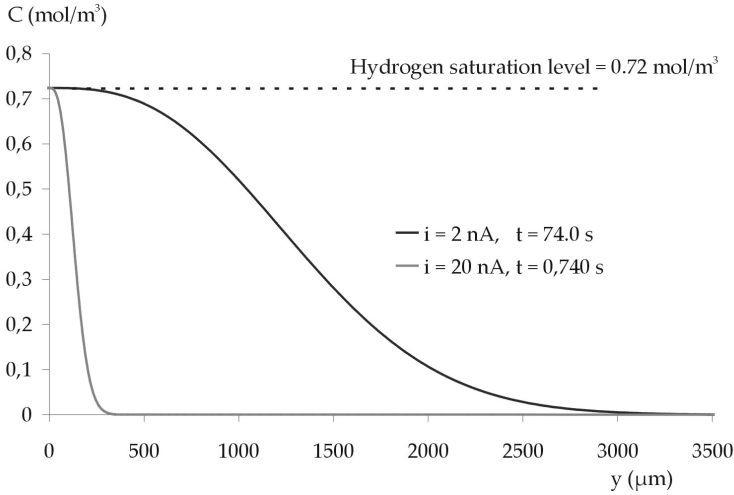
Figure 3.14: *Simulated concentration profiles when equilibrium occurs between gases in and out of the bubble after nucleation.*

$Q_{(t)}$. Further, it is assumed that the bubble had a rectangular shape and blocked the nanochannel.

If the electrical current continues to exist after $t_{nucleation}$, then the simulations will only predict the behavior at the bubble front side, not at the bubble electrode side, as gas is still produced at the electrode. Simulations have been performed, but no satisfying results are achieved. We estimate that about 95% till 99% of the produced gas will diffuse into the bubble, the other part will diffuse into the channel and therefore will take no part in the actuation of the bubble. Also here, these percentages will be much higher than in conventional electrolysis.

3.6   Hydraulic channel resistance

Assume a bubble with a cross-sectional area equal to the cross-sectional area of the nanochannel (i.e. the bubble is 'blocking' the channel and can act as a piston inside the channel). If this expanding bubble is fixed with one side to the electrode, then the free moving end of the bubble is pushing the liquid through the nanochannel as a piston. Assuming the liquid is incompressible, the channel structure is rigid and no volume changes due to temperature changes, then the volume flow through the nanochannel is exactly the bubble expansion. This volume flow will induce a pressure drop over the nanochannel from the moving bubble surface to the nanochannel outlet, caused by the channel resistance. For a nanochannel with a rectangular cross-sectional area this channel resistance [$\mathrm{Pa \cdot s \cdot m^{-3}}$] can be estimated with [34]:

$$R_{hyd} = \frac{3\mu l}{2a^3 b} = \frac{3\mu l}{a^2 A} \qquad (3.30)$$

where μ is the dynamic viscosity [Pa·s], l the channel length [m], a the half-channel height [m] and b the channel width [m], and A the cross-sectional area of the channel [m^2]. The pressure drop over the channel can be calculated as followed:

$$\Delta p = p_{hyd} = \phi \cdot R_{hyd} \tag{3.31}$$

where ϕ is the volume flow-rate [m^{3}s^{-1}]. The total internal bubble pressure can thus be given as: $p_{bubble} = p_{cap} + p_{atm} + p_{hyd}$. As the p_{hyd} is directly proportional to the volume flow-rate and the bubble is compressible, it acts like a spring with a spring constant directly proportional to the amount of gas and inversely proportional to the original length minus the compressed length, and can be derived from the ideal gas law [15]: $pV = nRT$, where p is the gas pressure [Pa], V is the gas volume [L], n the amount of gas in the bubble [mol], R the gas constant [8.3143 JK^{-1}mol^{-1}] and T is the temperature [K]; and the equation for the spring constant $k = F/s$, where k is the spring constant [Nm^{-1}], F the force [N] and s the compressed length [m] what is equal to the original length l_0 minus the new length l_1. Furthermore we can say that $p_0 = \frac{F_0}{A}$ and $V_0 = l_0 A$, which eventually gives:

$$k = \frac{nRT}{l_0 l_1} = \frac{p_0 V_0}{l_0 l_1} \tag{3.32}$$

It is clear that the spring constant depends on the bubble length at rest, and thus with the amount of gas in the bubble, as well as of the compression of the bubble. This spring constant in equation 3.32 together with the force on the bubble meniscus induced by the pressure drop described in equation 3.31 causes bubble compression. This compression will be released when the bubble growth has been stopped and the hydraulic resistance will damp the spring. The compression can be calculated using and rewriting equations 3.32 and 3.31:

$$F_{hyd} = p_{hyd}A = \phi R_{hyd}A = \phi \frac{3\mu l}{a^2} \tag{3.33}$$

This hydraulic resistance R_{hyd}, and thus the hydraulic force F_{hyd}, damps the movement of the liquid column. The damping ratio ζ [Pa·s/m^3] can be calculated with [35]:

$$\zeta = \frac{R_{hyd}A^2}{2\sqrt{km}} \tag{3.34}$$

When $\zeta \geq 1$, the response is a purely decaying non-oscillating motion.

The compression of the bubble and the hydraulic channel resistance work as a spring-damper system, schematically given in Figure 3.15, where F$_d$ is the damper force induced by the hydraulic resistance, m is the mass of the moving liquid column and F$_t$ the resulting force pushing the liquid column through the channel. The bubble length at any time can be described with [35]:

$$l_{(t)} = l_0 - (l_0 - l_1)e^{-2\pi f_0 \zeta t} \tag{3.35}$$

for $\zeta > 0$, where $(l_0 - l_1)$ is the oscillation amplitude, l_0 the length of the bubble in rest, l_1 the length of the compressed bubble, ζ is the damping coefficient and $f_0 = \sqrt{m/k}$ is the resonance frequency. The damping by the gas itself is not taken into account as it is assumed that this effect is much smaller than the damping due to the moving liquid column through the nanochannel. The total gas volume at a certain time becomes:
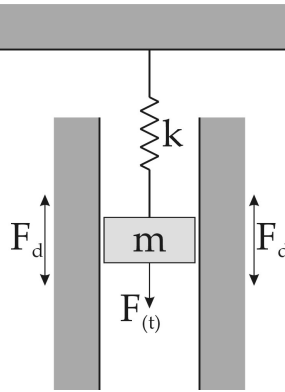
$$V_t = l_t A \tag{3.36}$$

Figure 3.15: *Schematic of the spring-damper system of expanding bubbles inside nanochannels. The spring constant k is the spring constant of a compressed gas bubble, F_d the resistance force of the moving liquid column and m the mass of the moving liquid column.*

Example

To estimate how the bubble compression affects the dosing we have to make some calculations. First we will see what the compression related to the gas production will be. Secondly, the spring constant, the resonance frequency and the damping coefficient will be found. And finally, we can find the bubble length at a certain time after the gas quantity inside the bubble has become constant.

When the bubble production rate q is 50 fl/s (i = 3.5 nA, see equation 3.11), and we assume all the gas produced is diffusing into the bubble, the volume flow-rate ϕ will also be 20 fl/s. Using equation 3.30 with l = 0.8 mm (channel length), a = 80 nm (half-channel height), b = 10 μm (channel width) and μ (dynamic viscosity) $= 1002 \times 10^{-6}$ Pa s [2], the hydraulic resistance $R_{hyd} \approx 2.35 \times 10^{20}$Pa s m^{-3}. The hydraulic pressure inside the bubble will be $p_{hyd} \approx 0.116$ bar.

As shown in section 3.3 the bubble pressure is 8.9 bar when the bubble in this example is in rest (p_0). The hydraulic pressure of 0.116 bar (1.3% of p_0) will decrease the initial bubble volume with 1.3%. Though this is a very small effect, it is increasing exponentially when decreasing the channel height and is directly proportional to the gas production rate. Because of the very small masses involved in the spring system described. Using equations 3.32,3.33,3.34 and 3.35 the solution is given in Figure 3.16, where can be seen that the non-oscillating decay is in the order of 30 seconds, and increasing with decreasing channel height. Though, this non-oscillating decay is not important using 160 nm high nanochannels due to the small effect of the bubble compression, the non-oscillating decay and bubble compression will gain significant influence when decreasing the channel height.
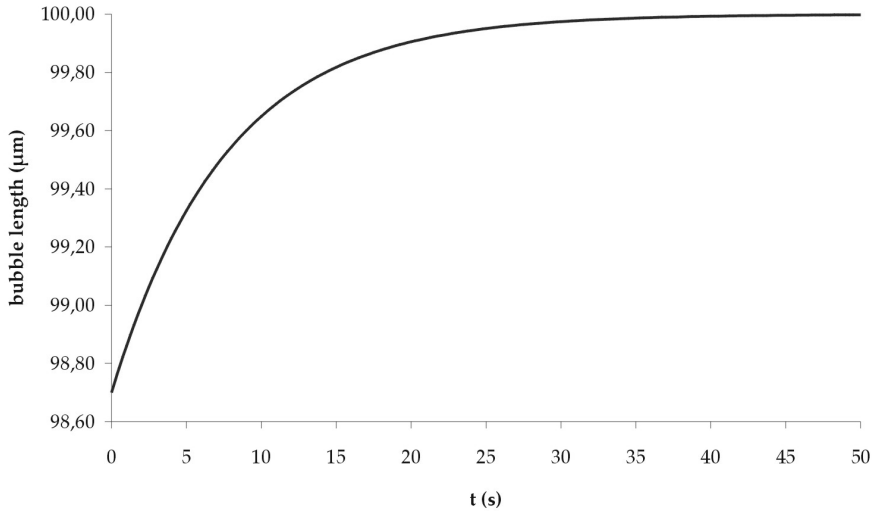
Figure 3.16: *Solution of equation 3.35 for a initial bubble length of 100 μm and a gas production rate of 50 fl/s, where the channel height = 160 nm, channel width = 10 μm and the length of the moving liquid column = 0.8 mm.*

3.7 Conclusions

Nanochannels strongly influence the electrochemical pumping process, especially the growth of bubbles caused by electrolysis. This already starts before electrolysis occurs: the charging of the electrodes. As the electrical currents are very small to generate very small bubble sizes, the charging of the double layers at the electrode surface takes time. Depending on the electrical current and the size of the electrodes the charging time $\sim$1 s.

When electrolysis occurs the produced gases will dissolve and diffuse away from the electrodes. The diffusion in the nanochannel is 1-D, i.e. along the length of the nanochannel. This will have a large effect on the diffusion rate, and thus on the gas concentration in the electrolyte. This limited diffusion eases bubble nucleation, but still, due to the very small gas production rate, the time before bubble nucleation can be on the order of seconds. On the other hand, due to the 1-D diffusion the concentration gradient away from the bubble is much smaller than in conventional bulk electrolysis, and therefore more gas diffuses into the bubble after nucleation, due to the much higher concentration gradient towards the bubble than towards the channel. Also, after stopping the electrolysis, bubbles in nanochannels will dissolve much slower due to the 1-d diffusion and the limited gas/liquid interface. This makes the bubble volume much more stable.

When bubbles have formed they experience capillary effects. First, there is the capillary pressure inside the nanochannels, as a consequence of the surface tension and

curvature of the bubble meniscus due to the hydrophilicity of the channel wall. In conventional sized channels this capillary pressure is neglected, but in nanochannels these pressures can easily be ~10 bar. This high pressure will reduce the bubble volume according the ideal gas law. Secondly, the bubbles will grow, except for a very short time range after nucleation, in 1-dimension: the length of the channel. When the bubble expands it will push the fluid column along the nanochannel. This fluid column will experience drag due to the channel wall, and this will cause the bubble to compress, which can be described with a simple spring-mass model. The drag will dynamically damp out the compressed bubble. In the system described, this effect is still small, about 1.5% volume difference with ~30 s decompression time, though this effect will become much more important when the used system is scaled down to smaller channel heights.

All these effects influence the electrolysis process and gas bubble behavior in nanochannels, some in large extent, such as capillary pressure and 1-D diffusion. Combining these effects causes electrolysis in nanochannels to appear very different from conventional electrolysis theory. However, for full understanding of the electrochemical bubble behavior in nanochannels, more modeling on gas and water diffusion should be performed. Current density at the electrode surface should also be further investigated.

Bibliography

[1] M. Faraday. On electrical decomposition. *Philosophical Transactions of the Royal Society*, 1834.

[2] D.R. Lide. *Handbook of Chemistry and Physics*. CRC, 74 edition, 1993-1994.

[3] A.J. Bard and L.R. Faulker. *Electrochemical Methods, Fundamentals and Applications*. John Wiley & Sons, 1 edition, 1980.

[4] M. Pourbaix and J.A. Franklin. *Atlas of electrochemical equilibria in aqueous solutions*. Pergamon Press, 1 edition, 1966.

[5] C. Neagu, H. Jansen, H. Gardeniers, and M. Elwenspoek. The electrolysis of water: an actuation principle for MEMS with a big opportunity. *Mechatronics*, 10:571–581, 2000.

[6] A.J. Bard and L.R. Faulkner. *Electrochemical Methods, Fundamentals and Applications*. John Wiley & Sons, 2 edition, 2001.

[7] G. Verkerk, J.B. Broens, R.E.A. Bouwens, P.A.M. de Groot, W. Kranendonk, M.J. Vogelezang, J.J. Westra, and I.M. Wevers-Prijs. *Binas*. Wolters Noordhoff, 5 edition, 2004.

[8] E. Tamaki, A. Hibara, H.B. Kim, M. Tokeshi, T. Ooi, M. Nakao, and T. Kitamori. Liquid filling method for nanofluidic channels utilizing the high solubility of CO_2. *Analytical Sciences*, 22:529–532, 2006.

[9] N.R. Tas, P. Mela, T. Kramer, J.W. Berenschot, and A. van den Berg. Capillarity induced negative pressure of water plugs in nanochannels. *Nano Letters*, 3:1537–1540, 2003.

[10] S. Mayer, L.A. Geddes, J.D. Bourland, and L. Ogborn. Faradic resistance of the electrode electrolyte interface. *Medical & Biological Engineering & Computing*, 30:538–542, 1992.

[11] E.J. Faber. *Towards the hybrid organic semiconductor FET (HOSFET)*. PhD thesis, University of Twente, 2006.

[12] W. Schmickler. *Interfacial Electrochemistry*. Oxford University Press, 1 edition, 1996.

[13] E. Warburg. Ueber die eolarisations capacitat des platins. *Analen der Physik*, 6:125–135, 1901.

[14] L.A. Geddes and R. Roeder. Measurement of the direct-current (faradic) resistance of the electrode-electrolyte interface for commonly used electrode materials. *Annals of Biomedical Engineering*, 29:181–186, 2001.

[15] G. M. Barrow. *Physical chemistry*. McGraw-Hill, 6 edition, 1996.

[16] A. Lee, N. Rajagopalan, M. Le, B.H. Kim, and H. M'Saad. PECVD silicon nitride for damascene applications. *Materials Research Society Symposium Proceedings*, 715:A10.7.1–A10.7.5, 2002.

[17] G.R. Langereis. *An integrated sensor system for monitoring washing processes*. PhD thesis, University of Twente, 1999.

[18] A. Isaacs, J. Daintith, and E. Martin. *Concise Colour Science Dictionary*. Oxford University Press, 1 edition, 1997.

[19] R.J. Hunter. *Foundations of colloid science*. Oxford University Press, 2 edition, 2001.

[20] N. Bremond, M. Arora, C.D. Ohl, and D. Lohse. Cavitation on surfaces. *Journal of Physics: Condensed Matter*, 17:S3603–S3608, 2005.

[21] C.E. Brennen. *Cavitation and bubble dynamics*. Oxford University Press, 1 edition, 1995.

[22] E.N. Harvey, D.K. Barnes, W.D. McElroy, A.H. Whiteley, D.C. Pease, and K.W. Cooper. Bubble formation in animals. i, physical factors. *Journal of Cellular Comparative Physiology*, 24:1–22, 1944.

[23] A.A. Atchley and A. Prosperetti. The crevice model of bubble nucleation. *Journal of the Acoustical Society of America*, 86:1065–1084, 1989.

[24] S. Shibata. The concentration of molecular hydrogen on the platinum cathode. *Bulletin of the Chemical Society of Japan*, 36:53–57, 1963.

[25] H. Vogt. On the supersaturation of gas in the concentration boundary layer of gas evolving electrodes. *Electrochimica Acta*, 25:527–531, 1980.

[26] H. Vogt. Interfacial supersaturation at gas evolving electrodes. *Journal of applied electrochemistry*, 23:1323–1325, 1993.

[27] K. Kikuchi, Y. Tanaka, Y. Saihara, M. Maeda, M. Kawamura, and Z. Ogumi. Concentration of hydrogen nanobubbles in electrolyzed water. *Journal of Colloid and Interface Science*, 298:914–919, 2006.

[28] K. Kikuchi, H. Takeda, B. Rabolt, T. Okaya, Z. Ogumi, Y. Saihara, and H. Noguchi. Hydrogen concentration in water from an alkali-ion-water electrolyzer having a platinum-electroplated titanium electrode. *Journal of applied electrochemistry*, 31:1301–1306, 2001.

[29] S. Shibata. *Denki Kagaku*, 44:709–712, 1976.

[30] S. Shibata. Supersaturation of oxygen in acidic solution in the vicinity of an oxygen-evolving platinum anode. *Electrochimica Acta*, 23:619, 1978.

[31] A. Volanschi. *Dynamic surface tension measured with single nucleation site electrodes*. PhD thesis, University of Twente, 1996.

[32] J.V. Macpherson and P.R. Unwin. Determination of the diffusion coefficient of hydrogen in aqueous solution using single and double potential step chronoamperometry at a disk ultramicroelectrode. *Analytical Chemistry*, 69:2063–2069, 1997.

[33] A. Seidell. *Solubilities of organic and inorganic compounds*. Van Nostrand Co., 1 edition, 1940.

[34] R.E. Oosterbroek. *Modeling, design and realization of microfluidic components*. PhD thesis, University of Twente, 1999.

[35] G.L. Trigg. *Encyclopedia of Applied Physics, Vol. 9*. VCH, 1 edition, 1994.

Chapter 4

Femtoliter dosing system: design and fabrication

This chapter describes the design and fabrication of the IMBID system. The complete dosing system consists of an integrated free-hanging planar nanoneedle for fluid delivery, which directly is integrated with a small nanochannel network. The nanochannels contain the electrolyte and sample material used for actuation and dosing. In the micropump, electrodes are located at specific locations in the nanochannels, and ensure proper actuation and dosing operations by means of electrochemical generation of hydrogen gas.

4.1   Introduction

The goal of this project is to develop an on-chip dosing system suitable to inject or extract small amounts of liquids into or from living human cells. Such a system could be used for biochemical research on single cell level on chip. Since average sized mammalian cells have a diameter of approximately 10 μm, the cell volume is ∼500 fL. Assuming that injected or extracted samples of 5% of the cell volume does not effect the viability of the cell, the dosing system should be able to dose samples smaller than 25 fL, as 30 fL microinjections in muscle cell nuclei gives maintaining viability [1]. No existing on-chip dosing system is able to dose these small samples accurately, and therefore, no dosing system for intracellular sampling on chip exists.

In Chapter 2 we reviewed the reported on-chip micropumps and dosing systems. Based on this review we state that electrochemical dosing systems are likely to be suitable to achieve accurate dosing samples smaller than 25 fL, as they are easy to integrate on-chip and have good possibilities to down-size due to the absence of any mechanical moving parts. Furthermore, they have low, or no, dead volumes, require low power and are very easy to control in both pumping/dosing directions.

4.2   System set-up

An on-chip femtoliter dosing system with integrated micro/nanoneedles has been designed and fabricated with conventional micromachining technology. As the electrolyte can not intefere with the cells directly, a system based on low diffusion between cell and dosing system has to be integrated. This system has not been integrated yet, as it is does not need to be a complicated system. Figure 4.1 shows a possible solution of plug injection into a cell without the cell being contaminated with electrolyte. Reversing this system enables it to be used as extraction system, and therefore, being bi-directional.
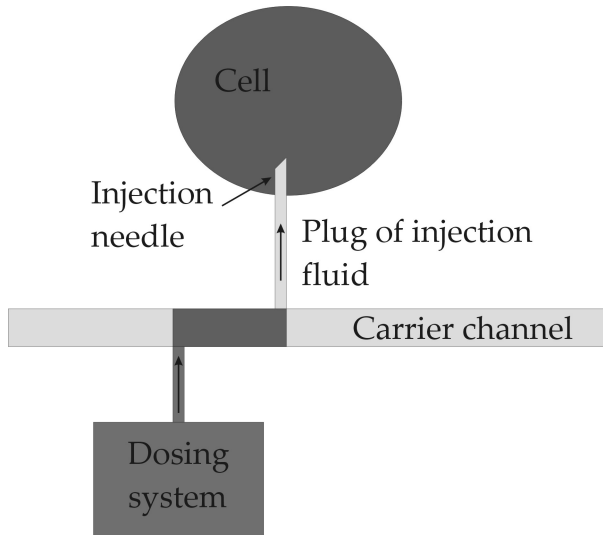
Figure 4.1: *Possible integration of dosing system with cells to avoid cells being contaminated with electrolyte. Be reversing the flow directions it is usefull for sample extraction, and therefore, suitable for a bi-directional dosing system.*

This femtoliter dosing system consists of a pair of platinum electrodes for electrochemical actuated hydrogen bubble formation inside a microfluidic network. This microfluidic network contains a bubble channel, wherein the bubble is formed and the cathode is situated in, ending in the micro/nanoneedle, a large anode chamber connected to the bubble channel, an electrical by-pass channel connecting the two electrodes electrically when a bubble is formed in the bubble channel, and a fresh electrolyte channel connecting the cathode with fresh electrolyte. Between the cathode and electrical by-pass channel, a height step is placed to prevent the bubble growing into the electrical by-pass or fresh electrolyte channel. The electrodes consist of a small cathode, placed directly inside the bubble channel, as working electrode and a large anode, situated in the large anode chamber, as auxiliary electrode. The cathode is kept small and placed directly in the nanochannel to achieve easy bubble formation, due to high hydrogen concentrations generated. On the other hand, the large anode is placed in a chamber, to suppress oxygen bubble formation by keeping the oxygen concentrations

low. A ruler is placed parallel of the bubble channel to measure the bubble length, and therefore, the dosed volume. A fabricated design of the femtoliter dosing system based on electrochemical actuation is shown in Figure 4.2.
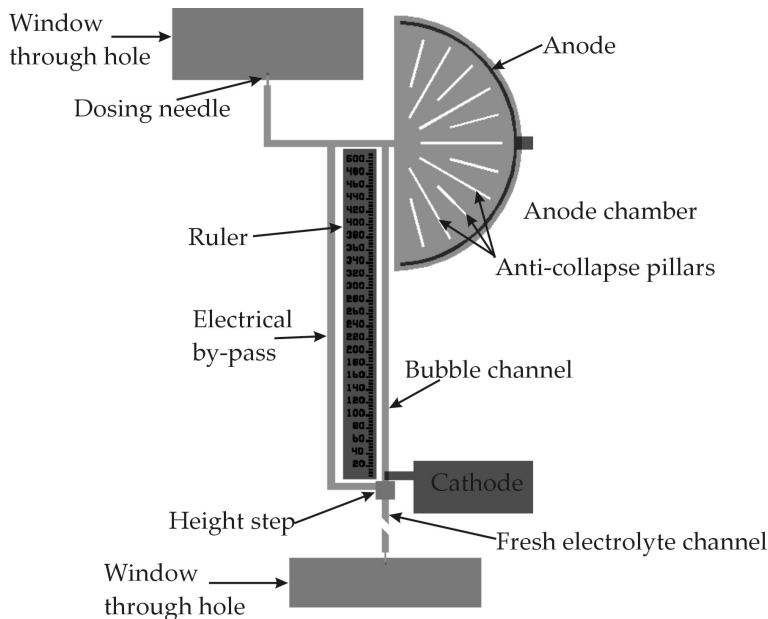

Figure 4.2: *Mask design of the front-side of the femtoliter dosing system.*

4.3   Nanoneedles

The function of the silicon based nanoneedle systems is to penetrate the cell membrane, and thus to access the contents of a single living cell. The hollow nanoneedles can pass fluidic samples through the cell membrane without mixing with the extracellular liquid. Therefore, the nanoneedles are very suitable for transportation of fluids into the cell (injection) or out of the cell (extraction). Important issues in the needle design are the easy integration of the nanochannel in the needle tip and the penetration properties of the needle. Penetration of the cell membrane with these needles should give low indentation depths to minimize cell damage [2], and therefore, the needle tip shape and size are important. Obataya *et al.* showed that flat frontal planes and small needle cross section decrease the indentation depth, where very good results were achieved using cylindrical needles with a diameter of 200 nm [3; 4].

Many microneedles have been fabricated for (transdermal) drug delivery or gene insertion [5; 6; 7; 8; 9]. These needles showed too large dimensions when using standing, or out-of-plane, microneedles, or gave problems when integrating these needles on-chip. Surface nanomachining gives solutions to these problems, and enables easy on-chip integration of nanoneedles and nanochannels.

4.3.1 Technical requirements

For cell membrane penetration the penetration force should be as small as possible to minimize cell damage. However, the needles should also be structurally strong enough to survive the cell penetration process. The following list of requirements are summarized:

- Minimal height and width, maximum sizes for cell penetration are not known, but reports have been made of diameters up to 1 μm [3], with good penetration results. Therefore, we aim at a maximum height of 1 μm and a maximum width of 5 μm

- Sharp needle tip. A sharper needle gives a lower penetration force[3].

- Structurally strong.

In addition, there are device requirements such that the needles can be easily integrated with conventional nanofluidic channels, such as:

- Hollow, with a 1-d nanochannel (see Section 4.6)

- Planar geometry

- Easy to integrate with nanofluidic channels

- Electrically insulating (see Section 4.4)

- Chemically resistant such that the structures can withstand long times in acid solutions, used to remove sacrificial layers, and basic solutions (see Section 4.6), used to etch through holes in the silicon wafer (see Section 4.5)

Because of these penetration and fabrication requirements we decided to use planar silicon nitride needle structures with a nanochannel integrated directly inside. The integrated nanoneedles and nanofluidic structure is discussed in more detail in the following sections.

4.3.2 Design

Figure 4.3 shows a schematic of the planar needles integrated with the nanochannels. The dimensions are chosen mainly because of conventional contact photolithography limitations. Minimal mask dimensions are 1 μm, therefore, the minimal width of the channel is 1 μm. Tests have shown that defect free channels of this width are very difficult to fabricate. 2 μm wide channels give much better results. The minimal alignment distance between two different masks is ∼1 μm when using conventional contact photolithography. To ensure that the channel is situated completely inside the needle, we used a spacing of 1.5 μm between the channel and the edge of the needle, resulting a needle width of 5 μm. The length of the needle is chosen to be long enough to penetrate the cell membrane of cells with diameters ranging from 5 μm to 50 μm, but short enough to prevent bending.

Tests have shown that the stiffness of solid silicon nitride needles of 260 nm thickness was sufficient to penetrate the cell membrane of K-562 cells. The channel height is chosen to be 150 nm. During fabrication the thickness was measured to be 160 nm. The silicon nitride isolation layer has a thickness of 500 nm, to give sufficient electrical
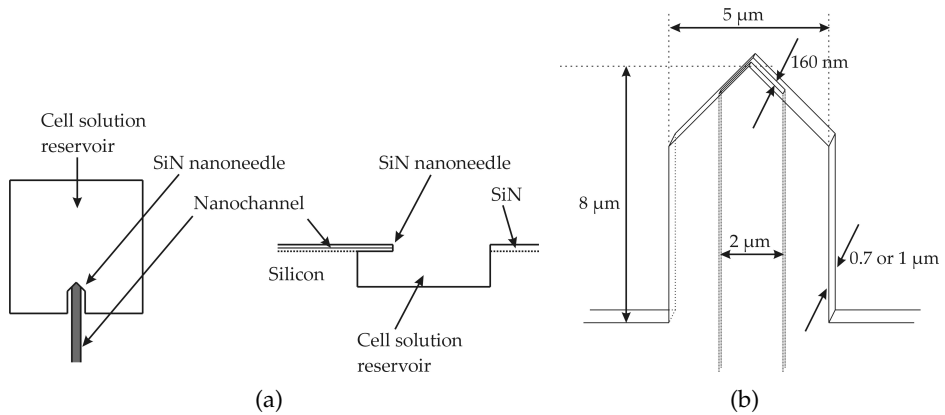
Figure 4.3: *Integrated nanoneedle and channel structure. (a) Left: top view, Right: cross-section, (b) 3D view with dimensions.*

resistance between the electrodes and the silicon. The capping layers are required to be thick enough to avoid collapsing of the nanochannel cavities, while not too thick such that film stress results in cracking or peeling. Figure 4.4 shows mask layout designs of the hollow silicon nitride based planar nanoneedles.
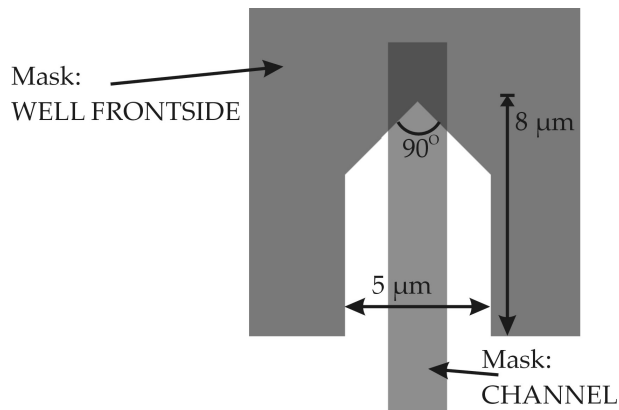

Figure 4.4: *Mask design of hollow needles. Typical channel width is 2 μm inside the needle.*

4.3.3 Fabrication

The wafers used for the fabrication are <100>-oriented 4″ double side polished (DSP) silicon wafers. First, a plasma enhanced chemical vapor deposition (PECVD) 200-500 nm layer of silicon nitride (SiN) is deposited at 400 °C providing the electrical isolation
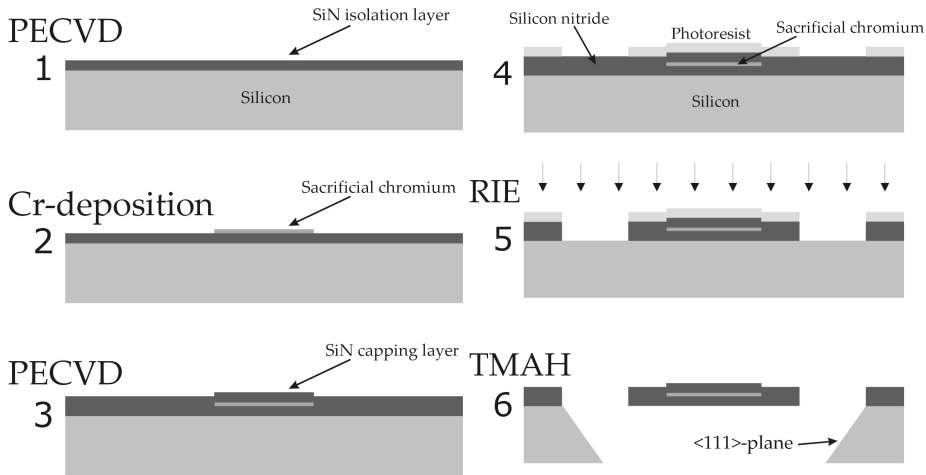
Figure 4.5: *Simplified process schematic of the fabrication of the planar SiN nanoneedles. (1) PECVD SiN isolation layer; (2) Deposit and pattern Cr sacrificial layer; (3) PECVD SiN capping layer; (4) Photolithography step defining the SiN layer; (5) RIE removal of exposed SiN; (6) Release of nanoneedle from Si substrate and through hole formation.*
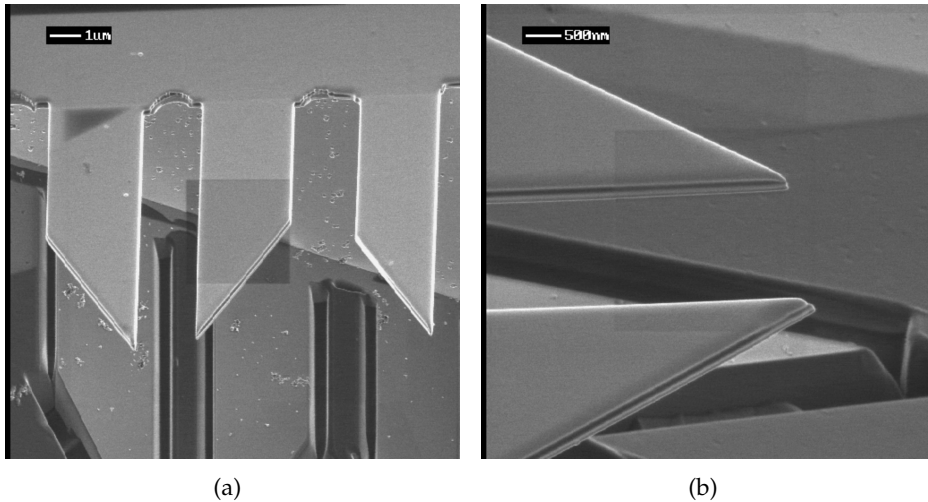

(a)   (b)

Figure 4.6: *SEM-pictures of fabricated solid planar SiN nanoneedles. (a) Three needles are shown, where the edges have been cut with FIB. The FIB-cutting has produced sharp edges of the needles, as well as ditches in the floor of the well. (b) Close-up of a needle tip after FIB-machining.*

between the electrodes and the silicon substrate. For solid needles one layer of SiN is sufficient to produce the needle, for hollow needles two SiN layers are needed with a sacrificial chromium strip in between to produce the nanochannel. To produce the sacrificial chromium strip and nanochannel, see section 4.6.
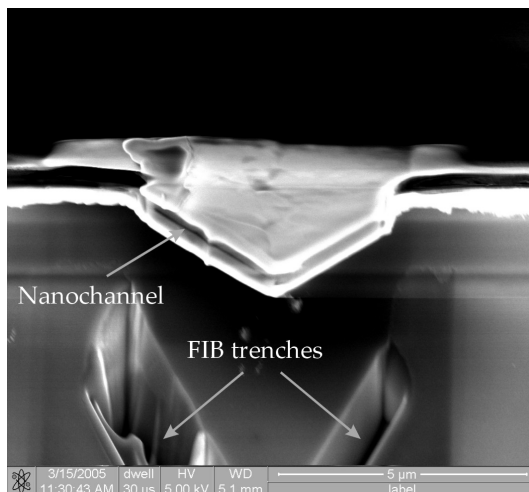

Figure 4.7: *SEM-picture of a fabricated completely released integrated SiN nanoneedle and nanochannel following the FIB sharpening procedure. In the bottom of the picture trenches from the FIB machining process are visible.*

To form the nanoneedle positive photoresist (Olin 907/12) is spun over the wafer and contact photolithography and etching are used to form the needle shapes, see Figure 4.5. With RIE, the exposed nitride layer is etched from the silicon substrate. To create a free-hanging nanoneedle wet-chemical TMAH-etching is used, at low temperature and low concentration (55 °C and 10 mass%). This reduces the Si etch rate, but increases the selectivity between Si and SiN, therefore, the nitride needles will not be attacked compared with conventional KOH-etching or TMAH-etching at 90 °C and 25 mass%. All fabrication steps are shown in detail in Appendix A.

To increase the sharpness of the needle edges, the edges have been cut using focused ion beam (FIB) machining by Vishwas Gadgil, MESA$^+$, University of Twente, Enschede, The Netherlands. Pictures of the sharpened needles can be seen in Figure 4.6. A fabricated sharpened hollow silicon nitride needle is shown in Figure 4.7.

4.4 Electrodes

Platinum electrodes are commonly used for on-chip electrolysis [10; 11; 12] because Pt is an inert metal and which efficiently produces hydrogen [13]. A disadvantage of Pt is that it is hard to etch compared to other metals. Platinum can be evaporated [14] or sputtered [15] on the substrate. To create Pt structures, it can be wet-etched using an appropriate etch mask, such as oxidized platinum [16]. Alternatively, platinum can be

removed using IBE [17] or using a lift-off procedure [18]. Recently a new wet-etching technique has been reported where platinum is alloyed with titanium [19]. This alloy can be removed in a standard H_2SO_4:H_2O_2 etchant.

4.4.1 Technical requirements

Design requirements as described in 2:

- Small cathode for high concentration hydrogen for easy hydrogen bubble formation

- Large anode for low concentration oxygen

- Equal distribution current density anode to suppress oxygen bubble formation

Fabrication requirements:

- Platinum

- Minimal height differences after processing to reduce risk of fluidic leakage

- Adhesion layer suitable for cathode and anode

To increase the adhesion of platinum on silicon substrates layers of an other metal are typically used. Common adhesion layers are chromium, titanium or tantalum [20; 21]. Tests have been performed with all these layers. Chromium was not suitable as it dissolved at the anode during device testing. Tantalum was hard to remove from the unpatterned silicon nitride and needed an extra chemical wet-etching step that attacked the silicon nitride as it contains hydrofluoric acid (HF). Therefore, titanium was used as adhesion layer for both the anode and cathode and it was easy to remove from unpatterned silicon nitride by the platinum etchant.

4.4.2 Design

The cathode and anode electrodes serve different purposes, therefore each has different design requirements. The cathode is used for hydrogen gas bubble generation, and the anode is used to complete the electrical circuit.

Cathode

To ensure a high concentration of hydrogen, the gas that is used for the bubble actuation, the cathode is chosen small, 100 μm^2, and positioned inside the gas-flow channel, see Figure 4.8. To control the bubble direction, the cathode is placed close to a height step, at 5 μm. It is assumed that the minimal distance between the height step and the cathode should be at least the channel height, because the bubbles are formed at the electrode edge, and there should be enough space to allow the bubble growth until they touch the channel floor and roof. This is because the height step will have maximum effect if the bubbles have grown to their maximum radius between the channel floor and roof. Increasing the distance also increases the electrical resistance of the electrolyte via the by-pass channel and the dead volume of the dosing system, as gas bubbles between the height step and the cathode do not cause dosing in the preferred direction. Tests
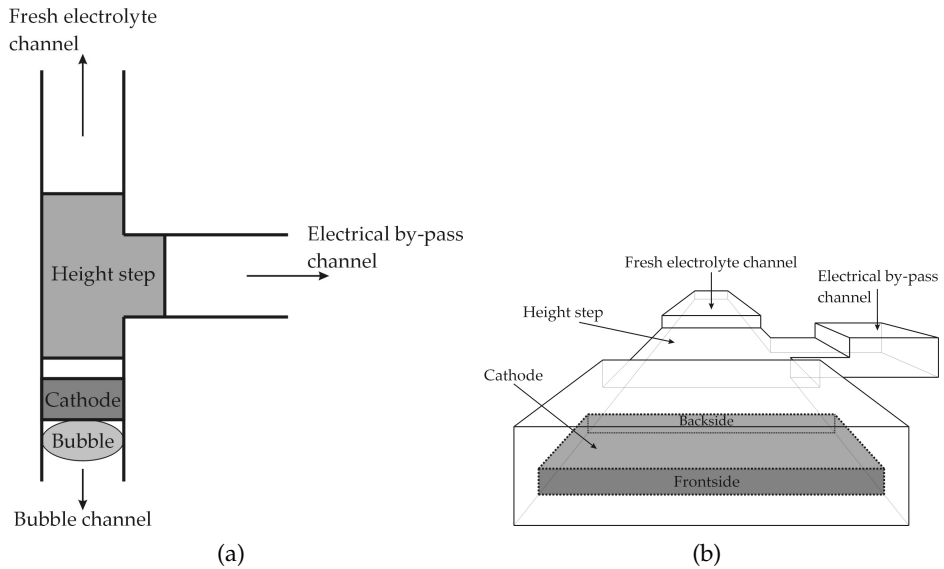
Figure 4.8: *Topview (a) and wire work (b) of the cathode, completely across the nanochannel, and height step integrated in the channel.*
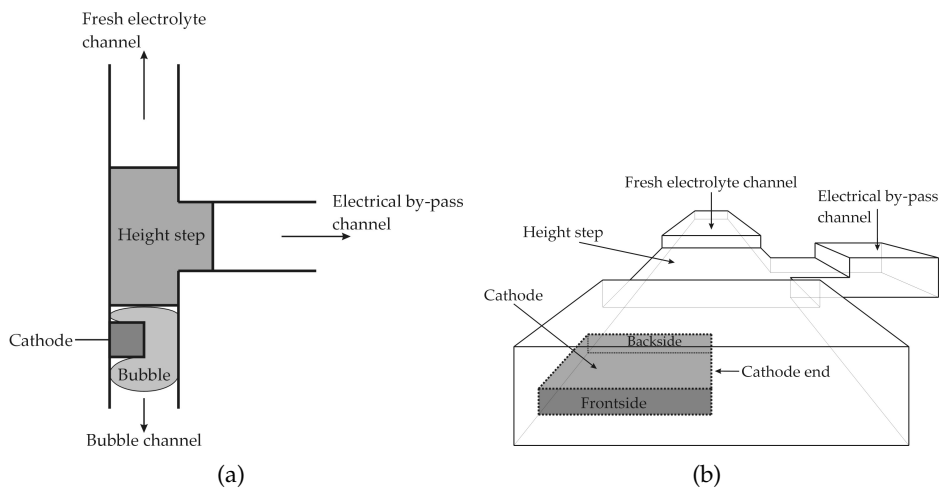

Figure 4.9: *Topview (a) and wire work (b) of the cathode, reaching only halfway the nanochannel, and height step integrated in the channel.*

have been performed with varying distances, and it was determined that a distance of 5 μm gave satisfactory results. With distances shorter than 5 μm, not all bubbles stopped at the height step.

In early experiments when the cathode was positioned across the complete channel width (see Figure 4.8), bubble formation occurred at the anode-side of the cathode. Due to differences in channel height above the cathode and the normal channel, the cathode was functioning as a weak height step itself, and therefore restricted bubbles passed over the cathode and moved towards the height step. The counter pressure caused by hydraulic resistance of the moving liquid column increased with increasing bubble growth to a point when the weak step height of the cathode could no longer hold the bubble, resulting in the bubble detaching and moving to the designed height step. This situation resulted in a very unstable actuator. To overcome this problem a new cathode design was chosen where the cathode reached half-way across the channel, giving a area of 50 μm^2, see Figure 4.9. Now, there was space left open for the bubble to fold around the cathode to the height step in the beginning of the evolution, and before the dosing experiments started. This eliminated unwanted bubble backward movements. A close-up at the mask layout design of the cathode is shown in Figure 4.10.
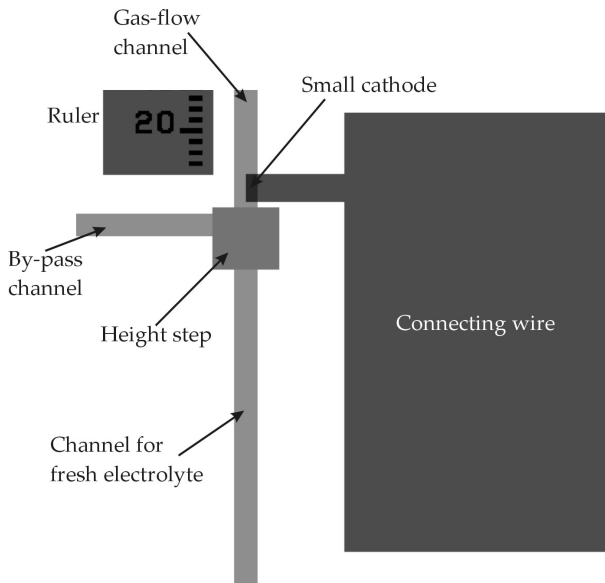

Figure 4.10: Close-up of the cathode in the mask design.

Anode

The design of the anode is shown in Figure 4.11. The purpose of the anode is simply to complete the electrical circuit in the electrochemical system. The dosing system is based on the volume expansion due to hydrogen bubble evolution at the cathode. Oxygen bubble formation will introduce an extra volume expansion, and thus extra dosing, therefore oxygen bubble formation should be suppressed. To achieve a small oxygen concentration at the anode low current density at the anode surface and a large volume around the anode are needed. To achieve a low current density the anode surface

area is made large in relation to the cathode surface area (6.0×10^{-9} m^2 versus 50×10^{-12} m^2) and thus the current is equally distributed over the anode by making the anode a large half-circular electrode, with the channel towards the cathode in the center of the radius. The roof of the large anode chamber has to be supported to prevent collapsing caused by the large capillary forces that can occur during drying of the channels [22]. In experiments, under no circumstances have we seen bubble formation at the anode.
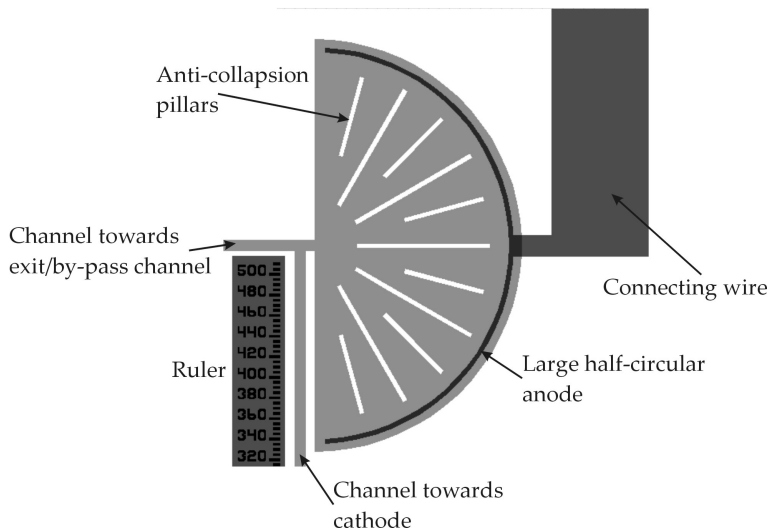
Figure 4.11: Mask design of the anode.

An additional design element is the ruler to measure bubble growth and volumetric dosing, shown in Figure 4.11 Fabrication is discussed in Section 4.5.

4.4.3   Fabrication

In a homemade sputter apparatus, a titanium adhesion layer of 10 nm is sputtered on the silicon nitride, and directly followed (the wafer remains in vacuum) by a 40 nm thick layer of platinum. Photoresist is patterned over the areas of platinum to be removed, and the exposed platinum is oxidized using a oxygen plasma for two minutes at 500 W [16]. After the removal of the photoresist the unoxidized platinum and its titanium adhesion layer are removed in a wet-chemical etchant.

4.5   Through holes/cell reservoirs

During early experiments placing single human living cells on the nanoneedles it was determined that partially etched silicon wells, or reservoirs, were not suitable for visualizing cells using optical microscopy. Secondly, to increase the potential using the nanoneedles with an inverted microscope or optical tweezers [23] for cell placement may also be useful. Therefore through holes are needed at the nanoneedle tip. Different

techniques are possible to etch completely through a wafer. Commonly used dry directional methods such as deep reactive ion etching (DRIE) [24], powder blasting [25; 26] or mechanical or laser drilling [27] are available. For wet anisotropic methods KOH-, TMAH- and EDP-etching [28; 29; 30; 31] are often used. Finally, the well known HF-based etching can be used for isotropic wet etching [32; 31].

4.5.1 Technical requirements

To improve the visibility of the cells, through holes have to enable microscope light to pass through the wafer. The needle is at the edge of the through hole, so the edges should be clearly illuminated. Therefore, the opening on the bottom side should be larger than the opening in the top side to prevent light blocking. Furthermore, the needles have to become free hanging during fabrication of the through holes and must not be attacked or damaged during etching.

For creating suspended needles a high etch selectivity between silicon and silicon nitride is needed. This eliminates almost all the wet etching techniques for etching through holes. Only low-temperature (55 °C) and low-concentration (10 mass%) TMAH-etching gave sufficient selectivity, making it suitable for very long etching times (~24 hours). The TMAH-etching stops at the <111>-planes of the silicon, with a measured Si:SiN etch selectivity of about 1:100. Imperfections in the silicon nitride can result in pinholes due to the long etching time, thus decreasing the yield. Therefore, for testing the dosing system the through holes were not etched.

A possibility to increase the yield is to reduce the etching time by combining DRIE and TMAH-etching. The DRIE is used to etch from the bottom almost through the wafer, and the remaining silicon is removed by TMAH-etching thus producing the suspended nanoneedles. This possibility has not been tested.

4.5.2 Design

We use double sided polished wafers, on which silicon nitride has been deposited on both sides. In order to make through holes, windows have to be etched in the silicon nitride on the front and the back side of the wafer. Therefore, two photolithography masks were made, which are shown in Figure 4.12. In the mask designs the black regions are the masks for the front side of the wafer, the larger gray regions are the masks for the back side of the wafer. Attention has to be paid to needle structure, this is part of the front side mask, although it may seem to be part of the back side mask. In fact, the back side mask only contains squares. The masks for the front side contain the windows for the through holes, the needles, and the measurement ruler alongside the bubble channel (not shown in the figures).

The only difference between the masks for use in TMAH and DRIE are the sizes of the windows on the back side. TMAH-etching is anisotropic, so it follows the <111>-planes of the silicon, as where DRIE is directional with nearly vertical sidewalls. In Figure 4.13 the resulting cross sections of the wells after TMAH-etching and DRIE are shown. The <111>-planes are positioned with an angle of 54.7° [31] with respect to the <100>-plane. With a window of 300×300 µm^2 on the front side and a wafer thickness of 525 µm, one can calculate that the side length of the window on the back of the wafer has to be 1044 µm.
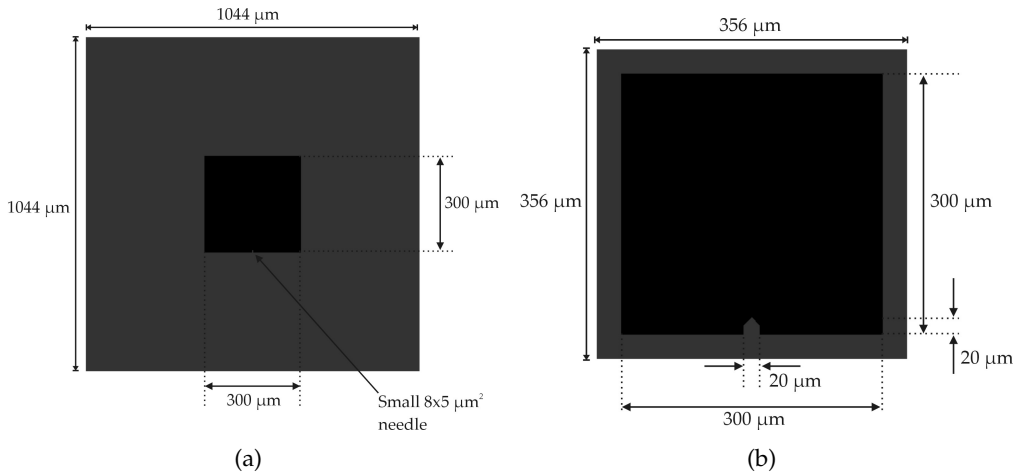
Figure 4.12: *Mask layout designs for the through holes, functioning as cell reservoirs. The black regions are the front side masks containing the front side through hole windows and the nanoneedles, the gray regions are the backside masks containing the backside through hole windows. (a) The masks are used for TMAH-etching, and (b) RIE.*
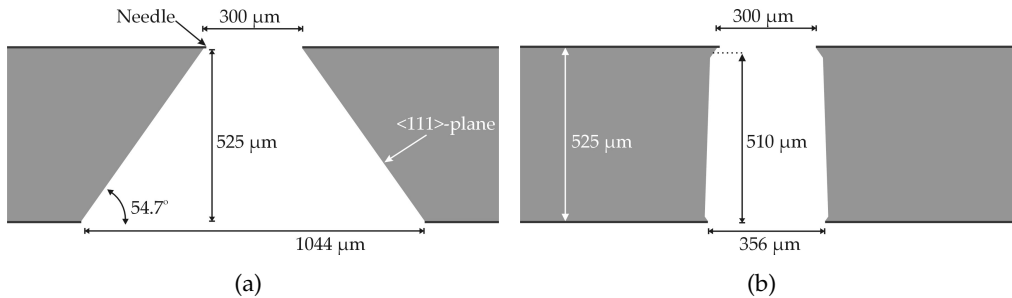

Figure 4.13: *Cross-section of the through holes produced with (a) TMAH, and (b) DRIE. Due to the angle of 54.7° between the <111>-planes and the front/back side of the wafer and the wafer thickness of 525 μm the needed back side window will be 1044 × 1044 μm^2 for the through holes etched with TMAH. The aspect ratio for the DRIE is assumed to be 1:30 and this gives for an etch depth of 510 μm a needed back side window of 356 × 356 μm^2. A short TMAH-etching step will etch the last 15 μm. Due to this TMAH-etching the vertical walls will be etched a little too and the through holes become a little wider.*

An additional design element in the mask is the ruler. The ruler shows the length of a bubble situated in the bubble channel. The ruler is etched together with the front side windows in the silicon nitride, but the RIE stops on the platinum ground plate.

4.5.3 Fabrication

The through holes have been made with TMAH-etching. Tests with more conventional KOH-etching showed that the etchant was too aggressive for the PECVD SiN films, and therefore not an option. Low temperature (55°C) and low concentration (10 mass%) TMAH-etching gave satisfactory results. After etching the windows in the silicon nitride on the front and back side of the wafer, the wafer was put in a stirred TMAH-solution for approximately 24 hours, until the through holes were formed. Optical microscopy inspection was performed, and etched longer if necessary. The through hole was narrower just below the needles, as can be seen in the microscope photo in Figure 4.14. Figure 4.14 also shows a schematic of the device cross-section, which shows the hour-glass shape due to imperfect etching along the <111>-planes. To avoid the hour-glass shape below the needle, it is suggested to increase the side length of the windows at the back side of the wafer to 1074 μm.
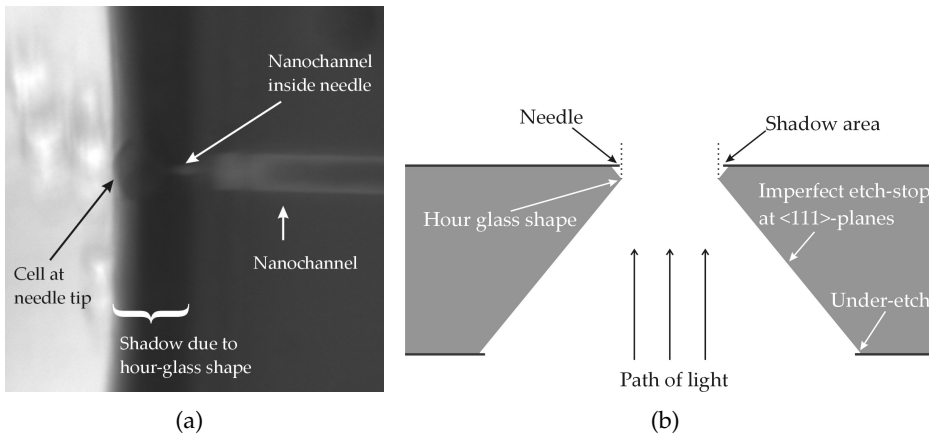

(a)   (b)

Figure 4.14: *(a) Optical microscopy photo of a cell at the needle, partly hidden in the shadow of the hour-glass shape. (b) Schematic of the through hole after etching showing the hour-glass shape and the under-etched areas.*

As a result of the long etching times the silicon nitride can be chemically attacked by the TMAH. This can be seen in Figure 4.15 where the photo at the left shows an hollow needle before TMAH-etching and at the right photo a solid needle after TMAH-etching is shown. Clearly visible are the damages at the edge of the silicon nitride and the under-etched areas. Therefore, it is suggested to produce the through holes with the combined DRIE and TMAH-etching.

In the left photo in Figure 4.15 a tongue under the needle opening is visible. This tongue is a result of the chromium sacrificial strip that was present during the DRIE-etching of the needle shapes. This chromium strip acts as an etch mask, and therefore the silicon nitride beneath the strip is not removed, what results in a small tongue under the needle opening when finished. This tongue may sharpen the needle for puncturing the cell membrane, as this small item pre-cuts the membrane with its much smaller
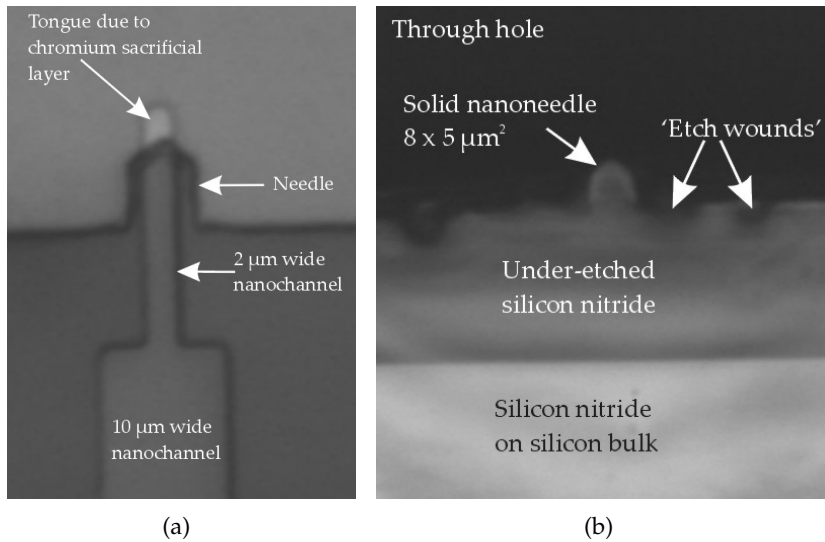
Tongue due to chromium sacrificial layer

Needle

2 μm wide nanochannel

10 μm wide nanochannel

(a)

Through hole

Solid nanoneedle 8 x 5 μm²

'Etch wounds'

Under-etched silicon nitride

Silicon nitride on silicon bulk

(b)

Figure 4.15: *(a) Hollow needle before TMAH-etching; (b) solid needle after TMAH-etching with under-etch and damages to the silicon nitride.*
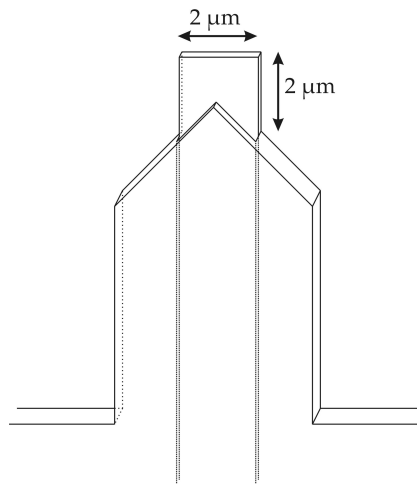

2 μm

2 μm

Figure 4.16: *Wire frame model of the hollow silicon nitride needle with tongue, resulting from the RIE-etching of the needle shape when the chromium sacrificial layer was still present, what acts like a etching mask. It is assumed that this tongue sharpens the needle, as due to its much smaller cross-sectional area can pre-cut the cell membrane.*

cross-sectional area. Therefore, it is not removed. Figure 4.16 shows a wire frame of the resulting hollow needle with tongue.

4.6 Nanochannels

To achieve hollow nanoneedle tips that can penetrate the cell membrane with minimal damage to the cell requires that the tip and channel height must be of submicron dimensions [2; 3; 4; 33]. Han et al. showed that cells penetrated by needles up to 600 nm in diameter still remained viable after 150 minutes. Additionally, the channel roof and bottom need to be rigid to resist the high capillary pressures inside the channels. With channel walls that are not stiff it is impossible to control the dosed volume. Therefore, of the three different known techniques for fabricating nanochannels [34] (bulk nanomachining and wafer bonding, nanoimprint lithography and surface nanomachining), surface nanomachining is the only technique possible. To be able to dose 25 fL multiple times, the channel has to contain sufficient volume, therefore the fabrication of 1d-nanochannels is chosen [35; 36].

4.6.1 Technical requirements

Assuming cells of 10 μm in diameter have a volume of ∼500 fL. For the dosing into single cells we aim at a volume of 5 % of the cell volume, giving a dosing volume of 25 fL. To be able to dose this volume in controlled sequences, the volume in the channels should be ∼500 fL. Furthermore, a precise volume prediction and dosing calibration is only possible if microscopic inspection is possible and the cross-sectional area does not differ significantly over the length of the channel. Therefore, a 1D-confined nanochannel is required.

To resist the long TMAH-etching times the chosen needle material, and therefore the channel wall material, is silicon nitride, see 4.5.3. Wolbers *et al.* have shown that silicon nitride does not have a negative influence on the cell viability, and therefore it is a suitable material for working with living cells [37]. A conventional sacrificial layer material for nanochannels is polysilicon, deposited in a low pressure chemical vapor deposition (LPCVD) reactor, but this is only possible if no metals are on the surface of the wafer. In our case, the platinum electrodes are at the surface of the wafer, as they have to be in contact with the electrolyte in the nanochannels after releasing the sacrificial layer. We have chosen to use chromium as the sacrificial layer, because chromium is easily removed in a chromium etchant, and does not attack the platinum electrodes or silicon nitride materials.

In addition, an electrical by-pass channel is integrated in the system design. The purpose of the by-pass channel is to supply an electrical current between the cathode and anode at all times. After a gas bubble has been formed at the cathode the electrical resistance of the bubble channel will increase to very high level, therefore, sustained electrode current for further bubble growth becomes problematic. To eliminate this problem, an electrical by-pass channel is positioned in parallel with the bubble channel, but in such a way that the initial resistance through the by-pass channel is higher than the bubble channel. Thus, the bubble growth will be initiated at the front side of the cathode, i.e. the side facing the bubble channel, because the current density at that side of the cathode will be higher than at the side facing the electrical by-pass channel, see Figures 4.8 and 4.9.

As the anode chamber has to be large, as described in 4.4.2, anti-collapse pillars are needed to ensure the roof does not collapse as a result of the capillary forces during

drying of the chamber. The pillars should be placed in such a way that they do not interfere with the current density over the anode.

To control the bubble growth direction at the cathode a height step is used as described earlier. The higher capillary forces in the height step, compared to the capillary forces in the nanochannel, will restrict the bubble from traversing the height step, and therefore it will control the direction of the bubble growth into the bubble channel. This height step can be achieved by ion beam etching of the chromium strip until its original height before the silicon nitride capping layer is deposited. RIE and chemical wet-etching appeared not to be suitable in our case.

4.6.2 Design

In Figure 4.2 a mask design of the nanochannel is shown. The channel has a width of 10 µm, except at the needle, where the width is 2 µm. The distance between the electrical by-pass channel and the bubble channel is 85 µm, making the electrical resistance of the by-pass channel about 35% higher than the electrical resistance of the bubble channel, in the pre-nucleation stage. It has been assumed that this gives 35% higher current density on the front side of the cathode. Tests where the distance between the bubble channel and the by-pass channel was 285 µm showed comparable results in respect with the 85 µm spacing, even though the electrical resistance over the by-pass channel was 107 % higher than that over the bubble channel. We chose to use the smaller distance between the two channels because of the easier optical inspection due to the smaller distance between both channels.

A side effect of the by-pass channel is that part of the dosed liquid enters the by-pass channel instead of continuing to the needle exit, therefore the by-pass channel is a fluidic divider. As the hydraulic resistance is a function of the length of the channel, when the cross-sectional area remains the same of the whole channel, it can be calculated that about 16 % of the total dosed liquid enters the by-pass channel and flows via the fresh electrolyte channel out of the system (length of the needle exit = 190 µm, length of the exit via the by-pass and fresh electrolyte channel = 1010 µm, both lengths are corrected lengths to the original channel height for the smaller channels at the needle tips and the lower channel height in the height step).

4.6.3 Fabrication

The 500 nm thick bottom layer of the channel, the same layer used for the fabrication of the nanoneedle, is made of PECVD-silicon nitride deposited, at 400 °C serving as an electrical isolation layer between the electrode and the Si substrate. On top of this layer a 160 nm thick layer of chromium is sputtered. The chromium layer is etched using standard photolithography and wet-etching with standard chromium etch (MERCK 111547.2500, Merck KGaA, Darmstadt, Germany) at room temperature for ~1 minute. During etching, the etching is monitored continuously to minimize the undercut. To ensure that the chromium layer has been etched completely electrical resistance of the wafer surface is measured. The height step is etched using conventional photolithography and IBE. Using photoresist a small window is left open over the chromium strip at the place the height should be reduced. The photoresist is hard-baked at 120 °C for 10 minutes before the IBE process, which takes ~30 minutes. Dektak measurements

showed that the height of the chromium strip for the nanochannel and the height step were 140-160 nm and 70-80 nm, respectively. The width of the channels are ~10 µm, see Figure 4.17. Figure 4.18 shows schematically the stack of different fabrication layers.
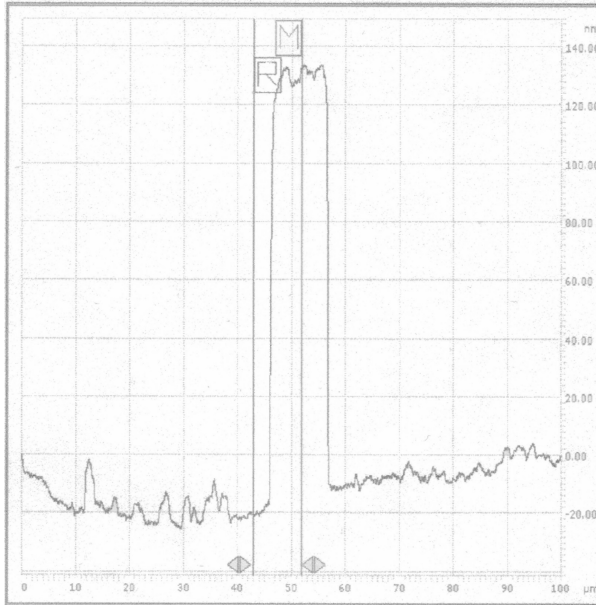

Figure 4.17: *Dektak measurement of the chromium strip before the capping layer is deposited. Height of the strip is 140-160 nm and the width of the strip is 10 µm.*
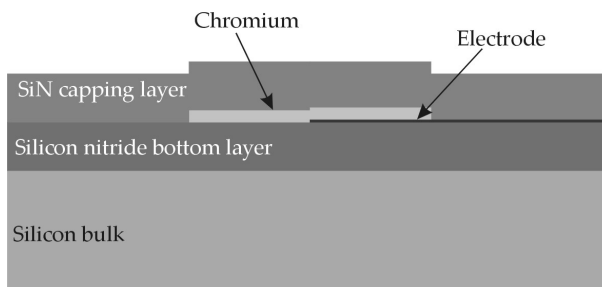

Figure 4.18: *Drawing of the cross-section of the fabrication before the sacrificial chromium is released.*

A 1 µm thick PECVD silicon nitride capping layer is then deposited at 300 °C. This lower temperature is chosen to reduce the stress in the capping layer, as it is assumed that high stresses in the capping layer cause fractures in the roof of the anode chamber. These fractures occurred in about 90 % of the cases. Increasing the caption layer thick-

ness from 500 nm to 1 µm did help, but further improvements on this have to be made. Deposition of low-stress SiN should be considered. The design of the anti-collapse pillars should be revised, as the cracks mainly occured at the ends of the anti-collapse pillars. The corners of the pillars should be rounded to eliminate stress concentration.

After the capping layer has been deposited the needles are processed, giving a connection between the outer world and the sacrificial chromium strip. The wafer is put in standard chromium etch and etched for ~4-5 days at 55 °C. Higher temperatures are not possible; the chromium etch will degenerate at higher temperatures. After all chromium is removed and the channels are completely released, the wafer is put in deionized water for another ~4-5 days to let the chromium etch diffuse out of the channels. With two cycles of drying the channels and filling with DI water the channel is cleared of chromium etchant. Figure 4.19 shows a SEM-picture of a fabricated nanochannel at the needle tip.
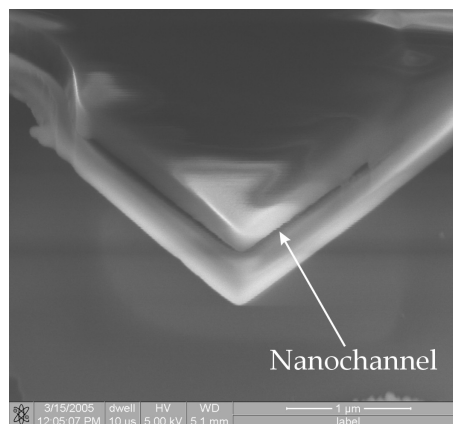

Figure 4.19: SEM-picture of a fabricated nanochannel (dark slit) at the needle tip.

4.7   Complete system

The complete IMBID system is fabricated combining silicon bulk etching, for the through holes, and surface nanomachining for the other elements. Twenty-one chips of $2 \times 1 \, cm \times 1mm$ containing four equivalent IMBID systems are fabricated in each wafer. Photographs of fabricated dosing systems can be seen in Figure 4.20, and a fabricated chip is shown in Figure 4.21. The complete process document is shown in Appendix A. Tests have been performed with different design parameters, which have different distances between cathode and height step, between the electrical by-pass channel and the bubble channel, the cathode completely or half-way in the bubble channel, the size and thickness of the needles, and the size of the channels. As a result of these tests the final dosing system is described.
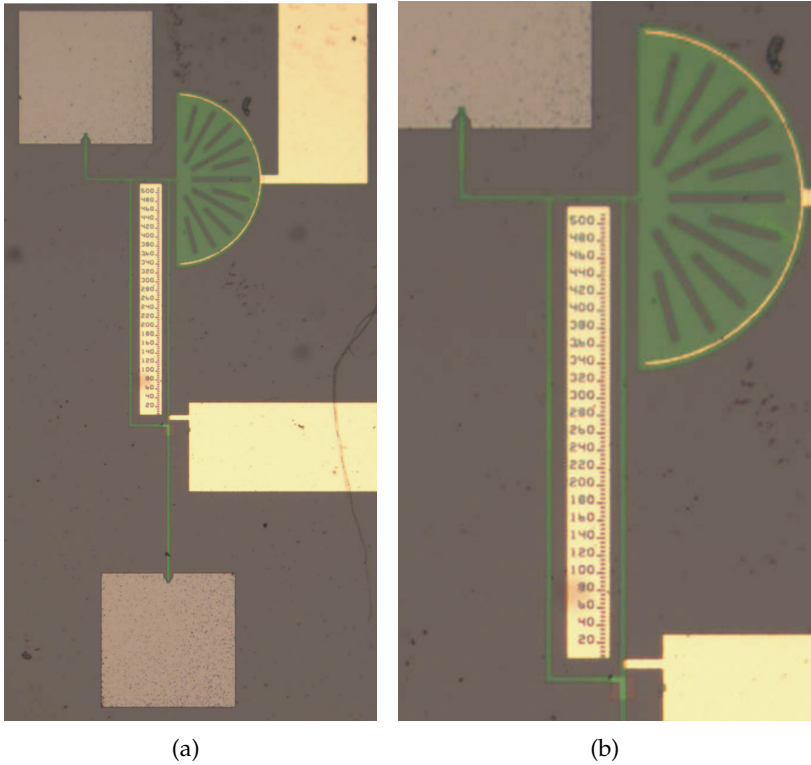
(a) (b)

Figure 4.20: *(a) Photos of the fabricated total dosing system, and (b) close up of a produced system.*
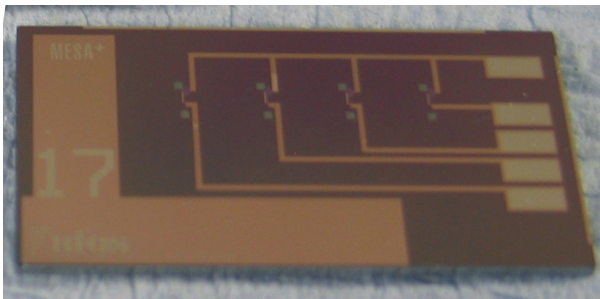

Figure 4.21: *Photographs of a fabricated chip containing four dosing systems. The connection pads for the electrodes are on the rightside of the chip. The top pad is connected to the anodes and the others to the cathodes, one for every dosing system. The windows for the non-etched through holes are the little green squares, with the dosing systems in between.*

4.8   Conclusion

An IMBID system has been designed and produced, combining surface nanomachining (nanoneedles, electrodes and microfluidic network) and silicon bulk wet-etching (through holes). Surface nanomachining has been used for the easy integration of the nanochannels, needles and electrodes, and it gives the possibility to go to very small dimensions.

The fabrication mainly focused on three aspects: the selectivity of the needles in respect with the silicon when through holes are etched, the release of the sacrificial layer in the fabrication of the nanochannels and the fabrication of the platinum electrodes.

Hollow micro/nanoneedles could be fabricated combining the sacrificial layer technique and silicon nitride deposition with reactive ion etching to structure the planar needles. For fabricating free-hanging planar needles, wet-chemical TMAH etching is used to remove the silicon under the needles. Since the through holes, to contain the cell suspension and for enabling top and down illumination, were etched using this TMAH etching step, the selectivity between the needle material and silicon was tremendously important. Since only PECVD could be used for the capping layer, due to the deposited metal electrodes, only the combination of PECVD silicon nitride and low temperature (60°C) and low concentration (10 %) TMAH etching appeared to be successful. In the future deep reactive ion etching should be considered to etch the bulk material in the through hole fabrication process, and only finishing the through hole fabrication with TMAH etching. This reduces the TMAH etching time, and therefore, reduces the impact of TMAH on the needles, enabling thinner needle walls and smaller needle dimensions. This can eventually reduce indentation depth and, therefore, reduce cell mortality.

Chromium appeared to be a very successful sacrificial material for nanochannel fabrication. Conventionally poly silicon can be used, but due to the metal electrode structures, no LPCVD of poly silicon can be used. Instead, we use chromium, which gives fast etching rates and chromium etchant does not attack the silicon nitride. The use of aluminum has been considered, but preliminary tests showed too low etching rates due to high viscosity of the etchant or attacks to the platinum electrodes.

Another important issue on the nanochannels are the silicon nitride capping layers. These layers can have intrinsic stress, resulting in cracks at places where stress concentrates. This is especially the case at the ends of the anti-collapse pillars in the anode chamber. Cracks in the capping layer result in liquid flow towards the anode chamber instead of the nanoneedle, giving incorrect dosing volumes. Low stress silicon nitride has to be considered to avoid this problem.

Platinum is needed for the electrode material, as it gives efficient hydrogen production. Structuring platinum is often done using the lift-off technique, as it is very difficult to remove platinum by chemical wet-etching or dry etching. It appeared very difficult to achieve completely flat electrodes using the lift-off technique, an effect commonly known as 'ears' or 'wings' occurred. 'Ears' cause electrical leaks through the silicon nitride capping layer, resulting in electrolysis occurring at these leaks instead of at the electrode. This problem is overcome with the use of local oxidation of the platinum, giving good selectivity for wet chemical etching of the platinum. The oxidized platinum remains, resulting in flat electrode structures and no leak currents. Also, to avoid leak currents to the silicon substrate through pinholes in the ground layer, this layer has to be sufficiently dense and thick. In these studies, 500 nm thick deposited at 400°C gave

satisfying results, although it has not been investigated what the minimal thickness is.

Characterizing the fabricated system showed that the capacitances had great effect on the system related to applied current and bubble generation. These capacitances can be decreased easily by reducing the areas of the electrode connections, which reduces in a smaller parasitic capacitance, and the anode, reducing the double layer capacitance at the anode. An optimized anode size still avoids bubble formation, but has minimal double layer capacitance. These reduced capacitances are even more important when smaller volumes are dosed. The channel structure can easily be scaled down as it is still 10 μm wide and 160 nm high. This easily can be reduced to 2 μm and 100 nm, respectively, resulting in a system that intrinsically can dose smaller than 15% of the dosed volumes shown in this chapter, so towards dosing volumes of ∼2–3 fL.

Experiments have been mainly focused on characterizing the dosing system, or on cell membrane penetration by the nanoneedles. Therefore, the produced systems were also dedicated to one of those two experiments, therefore, the through holes were not etched for the characterizing experiments. Cell membrane penetration experiments were conducted with both solid and hollow nanoneedles, but without the platinum electrode structure. Some small adjustments might be necessary to use a complete system for cellular dosing.

Bibliography

[1] P.R. Nelson and K.C. Kent. Microinjection of dna into the nuclei of human vascular smooth muscle cells. *Journal of Surgical Research*, 106:202–208, 2002.

[2] R.M. Hochmuth. Micropipette aspiration of living cells. *Journal of Biomechanics*, 33:15–22, 2000.

[3] I. Obataya, C. Nakamura, S.W. Han, N. Nakamura, and J. Miyake. Mechanical sensing of the penetration of various nanoneedles into a living cell using atomic force microscopy. *Biosensors and Bioelectronics*, 20:1652–1655, 2005.

[4] I. Obataya, C. Nakamura, S.W. Han, N. Nakamura, and J. Miyake. Nanoscale operation of a living cell using an atomic force microscope with a nanoneedle. *Nano Letters*, 5:27–30, 2005.

[5] J.G.E. Gardeniers, R. Luttge, J.W. Berenschot, M.J. de Boer, Y. Yeshurun, M. Hefetz, R. van 't Oever, and A. van de Berg. Silicon micromachined hollow microneedles for transdermal liquid transfer. *Journal of Microelectromechanical systems*, 12:855–862, 2003.

[6] D.V. McAllister, P.M. Wang, S.P. Davies, J.H. Park, P.J. Canatella, M.G. Allen, and M.R. Prausnitz. Microfabricated needles for transdermal delivery of macromolecules and nanoparticles: fabrication methods and transport studies. *PNAS*, 100:13755–13760, 2003.

[7] K. Oka, S. Aoyagi, Y. Arai, Y. Isono, G. Hashiguchi, and H. Fujita. Fabrication of a micro needle for a trace blood test. *Sensors&Actuators A*, 97-98:478–485, 2002.

[8] G. Cabodevila, B. Lepioufle, and H. Fujita. Arrayed micro needles for mechanical gene insertion. In *Biomedical Applications of Micro- and Nanoengineering*, pages 90–97, 2002.

[9] O.T. Guenat, S. Generelli, M. Dadras, L. Berdondini, N.F. de Rooij, and M. Koudelka-Hep. Generic technological platform for microfabricating silicon nitride micro- and nanopipette arrays. *Journal of Micromechanics and Microengineering*, 15:2372–2378, 2005.

[10] R. Gomez, A. Fernandez-Vega, J.M. Feliu, and A. Aldaz. Hydrogen evolution on Pt single crystal surfaces. effects of irreversibly adsorbed bismuth and antimony

on hydrogen adsorption and evolution on Pt(100). *Journal of Physical Chemistry*, 97:4769–4776, 1993.

[11] S. Böhm, W. Olthuis, and P. Bergveld. An integrated micromachined electrochemical pump and dosing system. *Journal of Biomedical Microdevices*, 1:2:121–130, 1999.

[12] V.I. Furdui, J.K. Kariuki, and D.J. Harrison. Microfabricated electrolysis pump system for isolating rare cells in blood. *Journal of Micromechanics and Microengineering*, 13:S164–S170, 2003.

[13] G. M. Barrow. *Physical chemistry*. McGraw-Hill, 6 edition, 1996.

[14] M. Loster and K.A. Friedrich. Angle-dependent infrared absorption spectroscopy at electrode/electrolyte interfaces. *Surface Science*, 523:287–297, 2003.

[15] H. Jacobsen, Th. Jung, K. Ortner, K.I. Schiffmann, H.J. Quenzer, and B. Wagner. Development of piezoelectric lead titanate thin film process on silicon substrates by high rate gas flow sputtering. *Sensors&Actuators A*, 133:250–258, 2007.

[16] M.J. Kim, L.A. Gruenke, R.J. Saia, and S.S. Cohen. Inhibition of acid etching of pt by pre-exposure to oxygen plasma. *Applied Physics Letters*, 44:462–464, 1984.

[17] Z.G. Zhang, D. Xie, C.G. Wei, T.Q. Shao, T.L. Ren, J.S. Liu, Z.H. Liu, and J. Zhu. RIE effect on the ferroelectric properties. *Integrated Ferroelectrics*, 81:69–76, 2006.

[18] J. Kitzmiller, D. Beversdorf, and D. Hansford. Fabrication and testing of microelectrodes for small-field cortical surface recordings. *Biomedical Microdevices*, 8:81–85, 2006.

[19] M. Zaborowski, P. Grabiec, and A. Barcz. Manufacturing of Pt-electrode by wet etching. *Microelectronic Engineering*, 82:283–288, 2005.

[20] A.W. Ruff and K.G. Kreider. Deposited thin film wear sensors: materials and design. *Wear*, 203-204:187–195, 1997.

[21] M.I. Awad, S. Sata, K. Kaneda, M. Ikematsu, T. Okajima, and T. Ohsaka. Ozone electrogeneration at a high current efficiency using a tantalum oxide-platinum composite electrode. *Electrochemistry Communications*, 8:1263–1269, 2006.

[22] N.R. Tas, P. Mela, T. Kramer, J.W. Berenschot, and A. van den Berg. Capillarity induced negative pressure of water plugs in nanochannels. *Nano Letters*, 3:1537–1540, 2003.

[23] Y. Wakamoto, S. Umehara, K. Matsumura, I. Inoue, and K. Yasuda. Development of non-destructive, non-contact single-cell based differential cell assay using on-chip microcultivation and optical tweezers. *Sensors&Actuators B*, 96:693–700, 2003.

[24] T. Akashi, M. Kanamaru, A. Kazama, Y. Itou, M. Horino, K. Fukuda, T. Ishikawa, T. Harada, and R. Okada. Fabrication of an optical beam scanning array integrating mirror and lens arrays by passive self-alignment using precisely formed through-holes. *Journal of Micromechanics and Microengineering*, 15:1754–1761, 2005.

[25] J. Emmelkamp, F. Wolbers, H. Andersson, R.S. DaCosta, B.C. Wilson, I. Vermes, and A. van den Berg. The potential of autofluorescence for the detection of single living cells for label-free cell sorting in microfluidic systems. *Electrophoresis*, 25:3740–3745, 2004.

[26] H. Wensink and M.C. Elwenspoek. Reduction of sidewall inclination and blast lag of powder blasted channels. *Sensors&Actuators A*, 102:157–164, 2002.

[27] T. Matsumura, T. Nakatani, and T. Yagi. Deep drilling on a silicon plate with a femtosecond laser: experiment and model analysis. *Applied Physics A*, 86:107–114, 2007.

[28] F.E. Rasmussen, M. Heschel, and O. Hansen. Batch processing of CMOS compatible feedthroughs. *Microelectronic Engineering*, 67-68:487–494, 2003.

[29] A. Faes, F. Giacomozzi, B. Margesin, and A. Nucciotti. Fabrication of silicon bolometers with bulk micromachining technology. *Nuclear Instruments and Methods in Physics Research A*, 520:493–495, 2004.

[30] J. Tiren, L. Tenerz, and B. Hoek. A batch-fabricated non-reverse valve with cantilever beam manufactured by micromachining of silicon. 18:389–396, 1989.

[31] M. Elwenspoek and H. Jansen. *Silicon Micromachining*. Cambridge University Press, 1 edition, 1998.

[32] F. Wang, X. Li, N. Guo, Y. Wang, and S. Feng. A silicon cantilever probe card with tip-to-pad electric feed-through and automatic isolation of the metal coating. *Journal of Micromechanics and Microengineering*, 16:1215–1220, 2006.

[33] S.W. Han, C. Nakamura, I. Obataya, N. Nakamura, and J. Miyake. Gene expression using an ultrathin needle enabling accurate displacement and low invasiveness. *Biochemical and Biophysical Research Communications*, 332:633–639, 2005.

[34] J.L. Perry and S.G. Kandlikar. Review of fabrication of nanochannels for single phase liquid flow. *Microfluidics & Nanofluidics*, 2:185–193, 2006.

[35] M.B. Stern, M.W. Geis, and J.E. Curtin. Nanochannel fabrication for chemical sensors. *Journal of Vacuum Science & Technology B*, 15:2887–2891, 1997.

[36] N.R. Tas, J.W. Berenschot, T.S.J. Lammerink, M. Elwenspoek, and A. van den Berg. Nanofluidic bubble pump using surface tension directed gas injection. *Analytical Chemistry*, 74:2224–2227, 2002.

[37] F. Wolbers, P. ter Braak, S. le Gac, H. Andersson, I. Vermes, and A. van den Berg. Viability study of hl60 cells in contact with commonly used microchip materials. *Electrophoresis*, 27:5073–5080, 2006.

Chapter 5

Femtoliter dosing system: characterization

This chapter describes the characterization of the fabricated electrochemical femtoliter dosing system. After a short introduction the experimental set-up is described and data processing techniques explained. In the following sections the bubble nucleation position and time are compared to the theoretical expectations. The bubble growth experiments are divided into two parts: i) dc-measurements where constant bubble growth is characterized and, ii) pulsed bubble growth used for dosing small sample volumes. Dosing of volumes down to 16 fL are presented. For sample retraction an electrochemical back-reaction is used and described in the next section. The last experimental section demonstrates the concept of electrochemical sample dosing from the nanochannels to an external reservoir through the integrated nanoneedle tip.

5.1   Introduction

In Chapter 4 we describe the design and fabrication of the electrochemical dosing system used. This dosing system should be able to dose small liquid samples in the femtoliter range, below 25 fL. This femtoliter dosing system has the cathode as working electrode, located in a nanochannel, next to a flow directing height step. The anode of the system is an auxiliary electrode, not being used for bubble generation. Therefore, hydrogen gas is produced at the cathode, and the resulting hydrogen bubble will be directed into the nanochannel. As this hydrogen seals the nanochannel, it acts as a piston. By growth or shrinkage, controlled electrically, fluid can be dosed out of or into the nanochannel where the bubble is located in.

Since electrochemical actuation is new in nanochannels, and no known reports of similar femtoliter dosing systems exist, it is of great importance to characterize the fabricated dosing completely. This chapter describes the characterization of the femtoliter dosing system, and discusses the results in relation to theory, shown in Chapter 3.1 and design, shown in Chapter 4. In the pathway to our ultimate goal, achieve an femtoliter dosing system suitable for intracellular dosing of sample volumes less than 25 fL, we divide the characterization in smaller steps:

1. **bubble nucleation**: does a hydrogen bubble form in the nanochannel? And if

so, does it compare to the theory in terms of nucleation time and position? Since no electrochemical bubble formation in nanochannels has been performed before, this is an important issue and can give fundamental insights.

2. **bubble growth**: how performs the linear bubble growth? After a bubble has been formed, it can be used for actuation. This step characterizes this linear actuation, or pump rate, based on applied dc current and time, since current×time gives theoretically a perfectly linear volume increase.

3. **discrete volume increments**: can we achieve dosing samples smaller than 25 fL? Current pulses are applied to generate certain amounts of hydrogen, generating a discrete volume increase of the bubble. Characterization of the volume increments is performed here, and the smallest repeatable dosing volume will be shown.

4. **bubble shrinkage**: is it possible to extract volume samples? Next to sample injection, sample extraction can be valuable for single cell research. Characterization of the extraction properties, or dosing in reversed direction, is performed in this step. For a successfull bi-directional dosing system this step needs to be successfull and controllable.

5. **sample transportation**: is sample transportation through the nanochannel really achieved? The bubble actuation is only useful when the bubble really acts as a piston, sealing the nanochannel. Fluid flow and ejection out of the nanochannel is characterized in this last step.

For a successful dosing system for intracellular dosing, all these characterization steps should give satisfying results.

In this chapter we start describing the experimental set-up. The chip and electrolyte preparation, electrical and optical set-up, and the data processing are described. After, the characterization of the bubble nucleation is described, dealing with the nucleation position and nucleation time, with thorough discussion of the latter. Followed by the bubble growth and flow rate characterization. The discrete volume increments, or dosing, by current pulses is the next characterization, split in a general part and in a part describing dosing volumes smaller than 25 fL. For reversed dosing, or sample extraction, we characterize the bubble shrinkage in the next section. The bubble shrinkage is described in three sections: shrinking due to diffusion, a free back-reaction where the electrodes are shorted and a forced back-reaction where a reversed current is applied. In the last but one section, the fluid flow through the nanochannels due to the bubble actuation is characterized. Finally, the conclusions are shown in the last section.

5.2   Experimental set-up

The experimental set-up can be divided in a few parts: the dosing chip and electrolyte preparation, the electrical set-up, and optical imaging set-up and data processing. The electrical set-up is used to drive the bubble growth and to record the electrical current and voltage across the electrodes. With the optical set-up, images of the bubble growth are recorded and bubble growth is quantified by data processing of the recorded images. The electrical and optical measurements are synchronized, in order to couple the optical bubble behavior to the applied electrical currents.

5.2.1   Chip preparation

The complete fabrication of the dosing chips was shown in Chapter 4. Following fabrication the chips are stored in DI water in a covered beaker to avoid contamination. Before each measurement, the chips are dried in a convection oven at 60 °C. After drying the chips are put in a beaker with the electrolyte solution, and the channels are filled by capillary forces. The chip remains in the electrolyte for ~5 minutes or until no air bubbles are visible in the channels. The chip is then taken from the electrolyte and placed under the microscope objective. The electrode contact pads are dried, and a small droplet of DI water is placed on the chip. Electrical connection is made by placing platinum wires, hold by micromanipulators, on the electrode contact pads, as discussed in more detail in Section 5.2.3.

5.2.2   Electrolyte

The electrolyte used was a 0.1M KNO_3(KNO_3 99+%, CAS 7757-79-1, Sigma-Aldrich, St. Louis, MO, USA) and 0.05 mass% (4×10^{-4} M) Tween® 20 (polyoxyethylene (20) sorbitan monolaurate, CAS 9005-64-5, Acros Organics, Geel, Belgium) solution at room temperature.

5.2.3   Electrical set-up

To properly characterize the bubble growth, the applied charge should be known at all times during testing. Since the required current is in the nA range, as discussed in Chapter 3, a simple current source was constructed and shown in Figure 5.1.
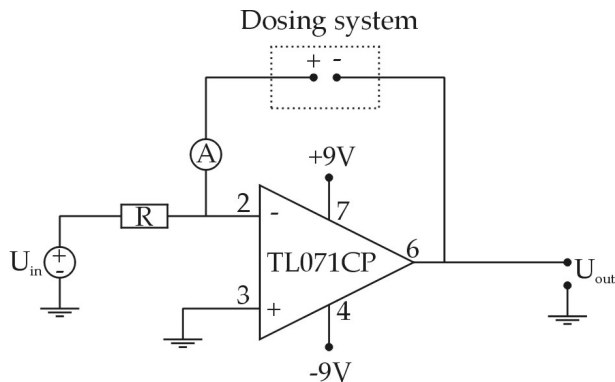
Figure 5.1: Electrical schematic of the built current source.

    The operational amplifier, TL071CP (Texas Instruments, Dallas, TX, USA), and resistance R, realized using 10-10MΩ resistors connected in series to achieve a resistance of 100 MΩ, are used to create a stable current source. With this electrical circuit the applied current can be set to a value equal to U_{in}/R. Therefore, to achieve a current of 1 nA, the applied voltage U_{in}=0.1 V. The voltage U_{in} of the circuit is provided by a Keithley 2400 SourceMeter (Keithley, Cleveland, OH, USA). The current i is measured

with a picoammeter (Keithly 6485 Picoammeter) and the output voltage U_{out} is measured with a multimeter (Keithley 2700 Multimeter). All instruments are controlled by a LabView program (LabView 7.0, National Instruments, Austin, TX, USA). The measurement rate was ∼2-2.5 samples per second. Electrical connection to the dosing chip is made with platinum wires, held in position by micromanipulators (PH120, Süss MicroTec, Munich, Germany), and connected to the current source by coaxial cables (Lemo Elektronik GmbH, Munich, Germany). The electrical set-up is shown schematically in Figure 5.2.

5.2.4 Optical set-up

The bubble growth in the nanochannels is measured optically with a microscope (Optical: Leica DM600M, Leica Microsystems GmbH, Wetzlar, Germany, Control box: Leica CTR600) with 200× magnification (ocular: 10×, objective: 20× 0.40 BD, Leica PL Fluotar). Images are recorded with a color CCD camera (ColorView8, Soft Imaging Systems GmbH, Münster, Germany) and the AnalySIS 5.0 software (Olympus Soft Imaging Solutions GmbH, Münster, Germany). The images are recorded with the Fast Image Sequence software package, with a capture time of 0.155 seconds, giving a frame rate of ∼6.5 frames/second. With the specified magnification the pixel size was 0.33 × 0.33 μm^2.

To be able to synchronize the electrical and the optical measurements, a shutter (Uniblitz VCM-D1, Vincent Associates, Rochester, NY, USA) is placed between the microscope's light source and the microscope. The shutter is controlled by the LabView program, thus synchronizing the optical and electrical measurements. The electrical and optical set-up can be seen in Figure 5.2.
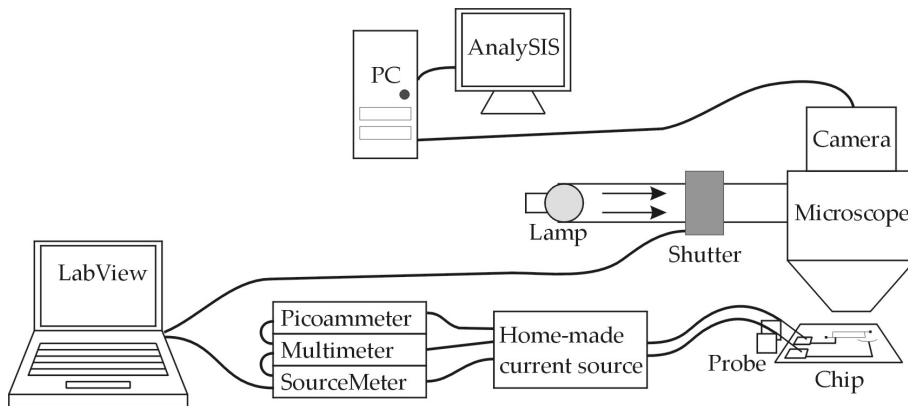

Figure 5.2: Schematic of the experimental set-up.

5.2.5 Data processing

The bubble size and growth is extracted from the raw data of the recorded images. Matlab (Matlab 6.5, The MathWorks Inc., Natick, MA, USA) is used to process the raw data.

A slight error is introduced because the end of the bubble is not square but spherical. As the bubble becomes larger this error can be neglected. Due to the pixel size of 0.33 $\times$ 0.33 μm^2 and cross-sectional area of 160 nm $\times$ 10 μm, the volume can be measured in steps of 0.53 fL. During data processing the electrical and optical measurements are synchronized using the dark images taken when the shutter was closed. First, the bubble length is estimated based on color contrasts between adjacent pixels, since, due to diffraction, bubble and electrolyte regions in the nanochannel have different colors. The bubble volume is estimated as bubble length $\times$ channel cross-sectional area.

5.3 Bubble nucleation

As discussed in Chapter 3.1 the bubble nucleation time can not be predicted precisely as the required parameters for supersaturation and charging time of the electrical double layers are not known. This section describes observations of the nucleation sites, followed by the estimations of the nucleation time. Some estimations of the earlier mentioned unknown parameters will be made.

To estimate the correct bubble pressure in the calculations, the contact angle of the electrolyte with the channel walls of $\sim$30° has been measured using simple light microscopy. Using the surface tension of water with 0.05 mass% Tween® 20 (0.032 N/m) [1], a channel width of 10 μm and a channel height of 160 nm, an internal bubble pressure of $\sim$3.5 bar is obtained using equation 3.21. All results have been measured with the system layout equal to the design shown in Figure 4.2.

5.3.1 Nucleation position

For the nucleation site a nucleation point is necessary, at which the hydrogen concentration reaches the required supersaturation level. The edge of the electrode is the expected nucleation site, as the shape of the edge is irregular so that bubbles can form more easily, and the local hydrogen concentration is very high. Graph 3.11 predicts that the middle of the cathode will have the highest hydrogen concentration, but also that at the edges of the electrode, which are relatively close to the center, the gas concentration will be almost the same. All experiments have been performed with the cathode extending half-way across the channel, as shown in Figure 4.9. Experiments have shown that bubble nucleation can occur at two different edge locations of the electrode: on the side edge, as shown in Figure 5.3, or on the front edge, shown in Figure 5.4.

On the other hand, most hydrogen gas is produced where the current density is the highest. In section 4.6.2 it was predicted that the front edge of the cathode will have the highest current density, and therefore the highest gas production rate. Nucleation also occurred at the front edge of the cathode, as is shown in Figure 5.4. Additionally, Figure 5.4 also shows the folding of the hydrogen bubble around the cathode, as described in section 4.4.2 and depicted in Figure 4.9.

Most nucleation appeared to occur at nucleation sites at the front side of the cathode, but this must be verified, as the bubble evolution is very fast compared to the slow frame rate and low optical magnification (200$\times$) of the measurement set-up. Therefore, for further research on this topic we recommend a higher magnification and frame capture rate.
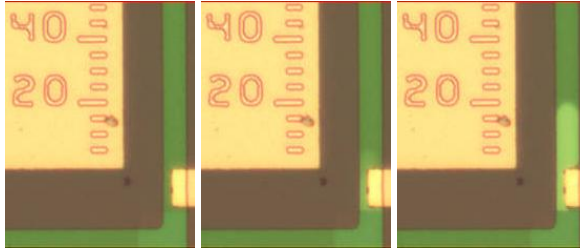
Figure 5.3: *Photo series of bubble nucleation at the middle of the cathode end. Applied current is 2 nA and the nucleation time is 9.5 seconds. Time between each picture is 0.155 seconds. Electrolyte contains 0.1 M KNO$_3$ and 0.1 mass% Tween 20. Bubble starts to form in the center picture.*
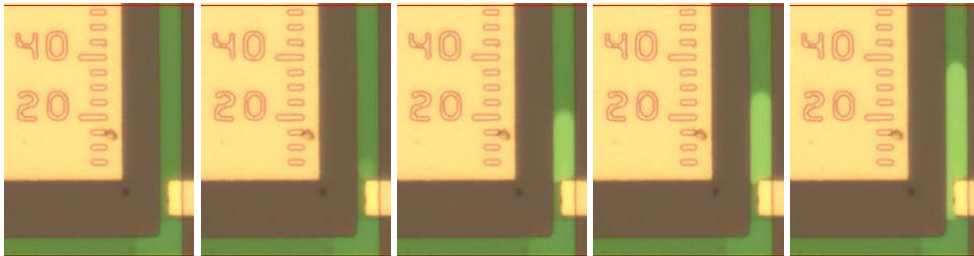

Figure 5.4: *Microscopic photographs series of the bubble nucleation at the front side of the cathode and bubble folding around the cathode towards the height step. Bubble folding around the electrode can be seen in the last two photographs, where the in last but one photograph the complete bubble is located at the front side of the electrode, whereas the bubble in the last photograph has folded around the electrode and reaches the height step. Drive current is 6 nA and the nucleation time is ~2.7 seconds. Time between the pictures is 0.155 seconds. Electrolyte contains 0.1 M KNO$_3$ and 0.1 mass% Tween 20. Bubble starts to form in second picture.*

5.3.2 Nucleation time

In Chapter 3 we predicted charging times for the cathode and the nucleation time after the cathode was fully charged. The nucleation times were calculated assuming 100-fold supersaturation of hydrogen, as reported in literature. For charging of the electrical double layer we estimated that the parasitic capacitance is of significant importance. In this section we characterize the nucleation time, and propose values for the required supersaturation.

The nucleation time, and other important properties, are discussed with the use of Figure 5.5, which shows the applied current, voltage and the bubble nucleation, followed by the bubble evolution. For further discussion we refer to the proposed electrical model shown in Figure 3.4.
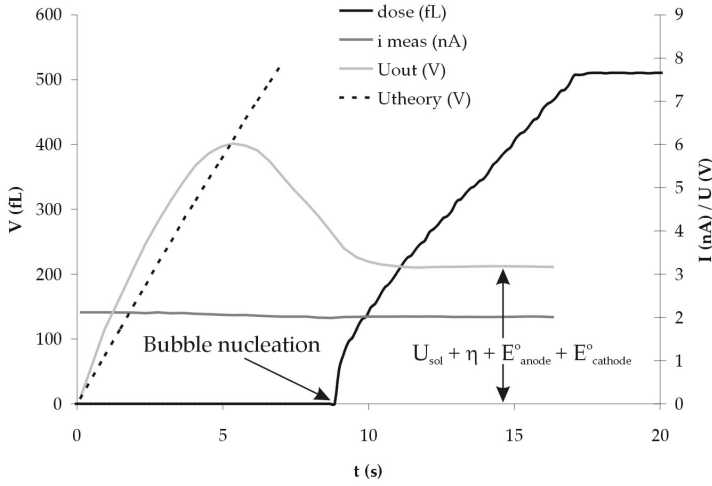
Figure 5.5: *Typical graph of the measured applied current (i_{meas}), measured voltage (U_{out}) and bubble volume (dose) during nucleation and bubble growth.*

Charging double layers

Figure 5.5 shows a typical measured response of the dosing system. A constant current i_{meas} of 2 nA is applied to the electrodes. The electrode potential is expected to increase linearly due to charging of the double layer and parasitic capacitances, until the onset of electrolysis, from where it is expected to have a constant value. The measured potential across the electrodes, U_{out}, is shown to increase approximately linearly for the first 4 seconds of operation, and finds its maximum value after 5.4 s. Then, unexpected, U_{out} decreases and settles to a constant value of about 3 V. The measured dose volume (solid black line) shows the onset of bubble nucleation at around 9 seconds, and increases approximately linearly until approximately 1 second after stopping applying current.

In theoretical calculations shown in Section 3.2.6, we expect a charging capacitance $C = 0.61$ nC, hydrogen production starting at 0.18 s, and a constant $U_{out} = 1.68$ V, achieved after $t = 1.32$ s, when all current is used for hydrogen production.

Though, the observed values are different. From the graph, we find $C = \frac{i\Delta t}{U} = 1.5$ nF, which is higher than the predicted value of 0.6 nF. Furthermore, U_{out} reaches 6.0 V at $t = 5.4$ s. The longer time t is a result of the higher observed values for C and U_{out}. The reason for a higher C is not known, but a possible explanation could be the quality of PECVD SiN isolation layer, which is less than conventional used LPCVD SiN. A reason for the higher U_{out} is found in the solution resistance, described in the following paragraph.

According to the electrical model shown in Figure 3.4 the charging potential should start at 0 V. This is not the case, where it is 0.12 V in this measurement, where other measurements have shown that this value can go up to 2.12 V. We expect this is caused by the capacitance charging from previous measurements. After a measurement the charge

on the capacitances is discharged by leakage, as the two electrodes are not shorted. As a result some charge remains at the start of a new measurement.

Solution resistance

As shown in Section 3.2.6, the expected $U_{out} = 1.68$ V, being the sum of $U_{dl\ an}$, $U_{dl\ cat}$ and U_{sol}. As the charges at the double layers remain constant during the electrochemical reactions, the decrease in U_{out} must be caused by a decreasing U_{sol}. Subtracting the constant values of $U_{dl\ an}$ and $U_{dl\ cat}$ being $E° = 1.39$ V, see Sections 3.1 and 3.2.6, from the measured U_{out} gives U_{sol}, decreasing from 4.6 V at maximum to 1.8 V at minimum. Therefore, according to our model, this means that R_{sol} peaks at 2.3 GΩ and decreases to 0.90 GΩ, where bubble nucleation occurs, where it is still approximately 6 times higher than the expected value of 141 MΩ. We find three possible reasons for the high R_{sol} at the maximum of the curve:

- So far, the over-potential η for the electrolysis reaction is neglected, as its value is unknown and depends on various variables, such as current density, electrode material and solution. Overpotential is caused by kinetic energy of the individual chemical species involved in the reaction [2]. This implies a higher η when the electrode is partly blocked by bubbles or when the reaction occurs at higher rates. Values of η=0.47 V for oxygen production at the anode and η=0.5 V for hydrogen production at the cathode have been reported [3]. Because of our very low gas production rate and current density at the anode, and the applied voltage remains stable during bubble nucleation and evolution, it is expected that the overpotential is much lower than the reported values, and can go down to the mV range.

- The dosing systems in the chip are loaded with an electrolyte with an initial concentration of 0.1 M. To avoid drying of the channels during the experiments, a small droplet of DI water is placed on top of the chip. During the experiments electrolyte is pushed into the DI water droplet, and after dosing the channel is filled again taking a sample of the droplet. This dilution, together with normal diffusion between the channel and the droplet, causes a decrease of the KNO_3 concentration in the electrolyte. As a result κ_{sol} decreases, and therefore R_{sol} increases.

- During the very long charging times of the capacitance, the ions in the solution have time to migrate towards an electrode. The ion mobilities of the K^+ and NO_3^- are 7.61×10^{-8} m s^{-1}/(V m^{-1}) and 7.41×10^{-8} m s^{-1}/(V m^{-1}), respectively. With an applied potential of 4 V over 800 μm, the ions would travel with $\sim$ 0.37-0.38 mm/s through an infinitely diluted electrolyte. Therefore, the ions are not evenly distributed over the electrolyte resulting in a R_{sol} increase.

We assume that the decrease of R_{sol} has to do with ion migration. During the electrolysis process OH^- and H+ ions are produced, and these ions migrate, due to electrophoresis into the channels. These ions have very high ion conductivities (349.65×10^{-4} m^2 S mol^{-1} for H^+ and 198×10^{-4} m^2 S mol^{-1} for OH^-) and therefore contribute to a decrease of R$_{sol}$ during electrolysis. After the electrolysis process

has stopped and the electrodes are shorted, the produced gases and OH$^-$ and H$^+$ react back to water, and R_{sol} increases until the original value if the back-reaction has completed.

After U_{out} decreases it stabilizes at a constant level. Subtracting E° and neglecting the overpotential η leaves U_{sol}. Using $U_{sol} = i_{meas} \times R_{sol}$, with known values of i_{meas} gives values for R_{sol} at different applied currents, as shown in Table 5.1.

Table 5.1: *Measured values for U_{sol} and estimated R_{sol} against i_{meas}.*

i_{meas} (nA)	U_{sol} (V)	R_{sol} (GΩ)	i_{meas} (nA)	U_{sol} (V)	R_{sol} (GΩ)
2.00	1.78	0.89	3.01	2.12	0.71
2.01	1.79	0.90	2.99	1.57	0.52
2.02	1.81	0.91	4.02	1.80	0.45
2.00	1.52	0.76	4.01	1.99	0.50
3.02	1.73	0.58	5.04	1.82	0.36
3.02	1.66	0.55			

These are very limited results, but it can be seen that U_{sol} remains rather constant over different applied currents while R_{sol} decreases approximately exponentially. Calculations have shown that if the remaining value of R_{sol} is completely caused by the produced H$^+$ and OH$^-$ ions, the amount of ions needed for this conductance is produced in 2.4 s. In an infinitely dilute electrolyte the travel time for a produced H$^+$ and OH$^-$ ion to travel to the counter electrode is approximately 1.3 s and 2.3 s, respectively (U=1.8V, l=0.92mm, ionic mobility H$^+$=36.3$\times 10^{-8}$ m s^{-1}/(V m^{-1}), and ionic mobility OH$^-$=20.5$\times 10^{-8}$ m s^{-1}/(V m^{-1}) [2]). As this is by far not an infinitely dilute electrolyte, it can be assumed that the final R_{sol} is caused by the produced H$^+$ and OH$^-$ ions in solution. These concentrations are approximately proportional to the applied current, and therefore, R_{sol} is approximately inversed proportional to the current, leaving a rather constant U_{sol}.

The rounded top of the potential curve can be explained by the assumption that R_{sol} limits the electrolysis current, i.e. the part of the applied current which goes through the electrolyte solution. The electrolysis starts when the double layers meet the required potential E°, and a part of the applied current is used for the electrolysis. When all applied current flows through the electrode/electrolyte interface, "full"electrolysis is achieved. If this interface is the cathode/electrolyte interface, the resulting electrolysis product is hydrogen, and therefore, "full"hydrogen production is the result, for the anode/electrolyte this is "full"oxygen production. All applied current can only flow through the electrolyte solution, and thus full electrolysis is achieved, when the potential difference $U_{sol} = i_{meas} \times R_{sol}$, and the potential over C_{par} equals $U_{sol} + E^\circ$. As R_{sol} starts to decrease and the part of current used for electrolysis starts to increase from the onset of electrolysis, the top of the potential curve is rounded. Due to this rounded top it can not be estimated accurately where the full hydrogen production starts. For simplicity reasons, we state that full oxygen production is performed when the curve meets its top, and the full hydrogen production is achieved a certain time before full oxygen production what is equal to the difference in charging times of the anode and cathode. For the shown graph, this time is equal to $\frac{CU}{i} = 0.36$ s.

The nucleation time will be estimated as the time from the start of full hydrogen production until nucleation occurs. Figure 5.6 shows the total time before nucleation,

and the estimated nucleation times against the applied current. From this graph it can
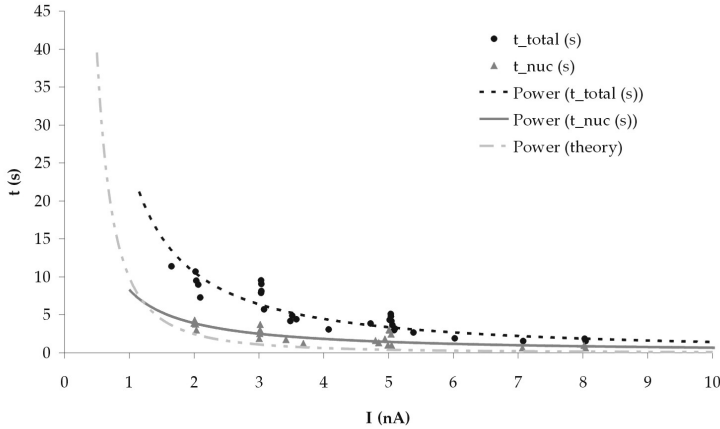

Figure 5.6: *Measured total times until nucleation occurs and the estimated nucleation times compared to the theoretical curve, calculated from Figure 3.11 in Section 3.5.1.*

be seen that the total time, including charging of the capacities, is about double the nucleation time. Furthermore, it can be seen that the estimated nucleation time is much longer than expected from the theory, as shown in Figure 3.11. The reason for this discrepancy could be the required supersaturation, which is not known. In the theoretical section we assumed a required supersaturation of 100-fold, but experimental values go up to 160-fold [4]. In Table 5.2 supersaturation values for several applied currents, estimated from the measured average times from Figure 3.11 in Section 3.5.1, are listed.

Table 5.2: *Estimated required supersaturation levels using a theoretical model with experimental data.*

i (nA)	average nucleation time (s)	required supersaturation (fold)
2	3.71	123
3	2.77	159
5	1.88	218

The estimated values for the supersaturation correspond well to values presented in literature (see Section 3.4.1), and increase with increased current density, also consistent with literature. Furthermore, the measurements were performed with very low electrical sample rates of ~ 2.5 s^{-1}, thus introducing large errors for these short times. The optical measurements were performed with a frame rate of 6.5 s^{-1}. Increasing the sample rate will increase accuracy, especially for the higher applied currents.

5.4 DC measurements/pump rate

This section describes the characterization of the bubble evolution under a constant applied dc-current. In the previous section, Figure 5.5 showed the nucleation of a hydrogen bubble. It was stated that the charging times of the capacitances was influenced by the starting potentials, and therefore the total time before nucleation is not constant. Figure 5.7 shows four bubble evolution measurements at 2 nA.
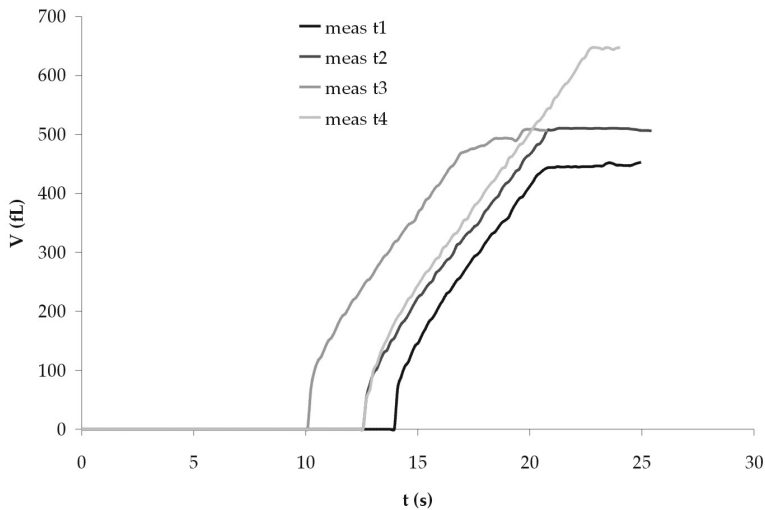

Figure 5.7: *Unsynchronized measurement series of bubble evolution with a constant dc-current of 2 nA at times t_1, t_2, t_3, t_4 where $t_4 > t_3 > t_2 > t_1$. The times between the successive measurements is not constant. Due to the differences in the duration of applied current and differences in nucleation time, different end volumes are achieved.*

As mentioned earlier following the initial test at time t_1, the bubble nucleation occurs earlier (at times t_2, t_3 and t_4) due to hydrogen gas remaining in the system. If we synchronize these measurements with t_0 at bubble nucleation, we get the graph shown in Figure 5.8. This graph shows a good correlation between the different measurements, and very linear growth of the bubble volume.

The growth rate of the bubble evolution can be taken from the slope of the linear increase. Figure 5.9 shows these growth rates, with their average and the theoretical expected value. This theoretical value (14.4 fL/nC) is much lower than the average measured value (26.8 fL/nC). The theoretical curve was calculated using the surface tension of water (73 mN/m) and a internal bubble pressure of 8.9 bar. If the surface tension of 0.4 mM Tween® 20 (∼32 mN/m) [1], and an internal bubble pressure of 4.5 bar are used, the results compare very well with theoretical value of 28.8 fL/nC. The measured values are ∼7% below the theoretical values. We think this is caused by the following reasons:
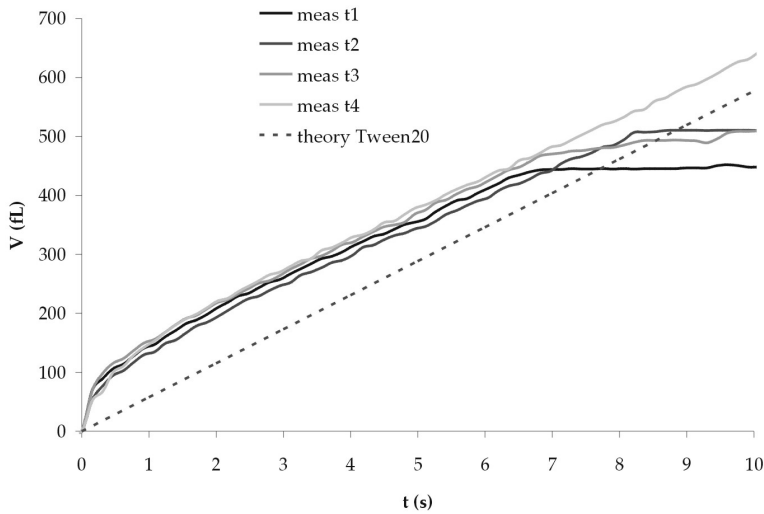
Figure 5.8: *Bubble evolution with a dc-current of 2 nA. The measurements are synchronized and t_0 is set at bubble nucleation.*
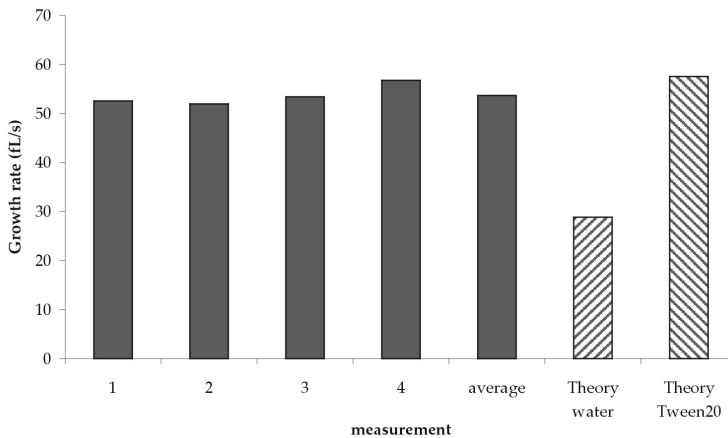

Figure 5.9: *Growth rates of the bubble growth with a dc-current of 2 nA.*

- Diffusion of produced gas into the channel. In the theory (see Section 3.5.2) we expect 95 - 99% of the produced gas will diffuse into the bubble.

- Decreasing the concentration of Tween® 20 due to dosing and diffusion into the DI water droplet on top of the chip. If the concentration of Tween 20 decreases from 0.4 mM to 0.1 mM the surface tension increases to ∼34 mN/m, resulting in a volume decrease of ∼6%.

- Small variations in the channel height and width can give some volume errors. We estimate these errors to be ~5%.
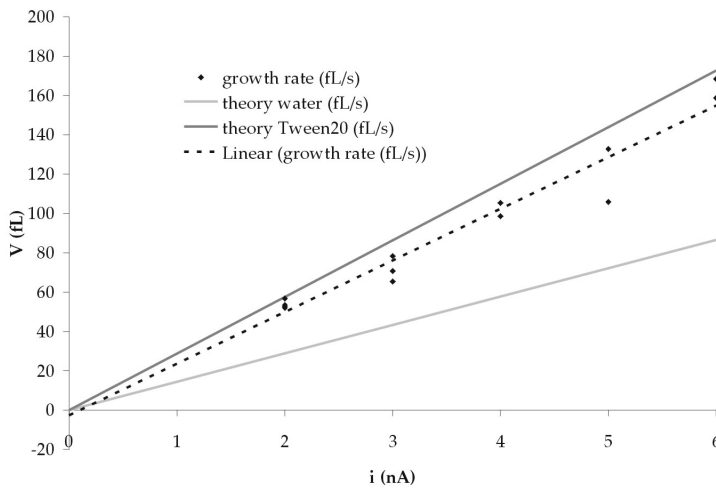
Figure 5.10: *Measured growth rates over measurement series of 2, 3, 4, 5, and 6 nA. The measured values are approximately 9% below the theoretical value of the Tween20 solution.*

Also, in the theory chapter (see Section 3.5.2) we estimate that 86% of the produced gas before nucleation will diffuse into the bubble when the current would be stopped at nucleation. The current is not stopped at nucleation, but still a bubble volume increase is expected. It is assumed that the fast bubble growth directly after nucleation is the result of this effect. The measured nucleation time for i = 2 nA is 3.71 s (see Table 5.2), the theoretical bubble growth rate is 57.6 fL/s for 2 nA, thus 86% of the calculated volume equals 184 fL. According to the graph in Figure 5.8 this increase is ~100 fL. Why this measured increase is much lower than the theoretical one is not known, but could be caused by the T-junction with the by-pass channel close to the cathode. This T-junction could increase the diffusion of gas into the channels, and therefore a decrease in the predicted percentage of gas generated before nucleation diffusing into the bubble. An other reason could be that, due to an unknown reason, the amount of hydrogen gas generated is lower than expected.

Figure 5.10 shows the growth rates of all measurements, with currents of 2, 3, 4, 5 and 6 nA. The error between the theoretical curve of Tween20 solution and the median of the measured curve over all currents is ~9%. This slight increase in error still can be explained by the reasons mentioned earlier.

5.5   Current pulse measurements/dosing of small volumes

The dc-measurements characterize the dosing system with a constant dc-current, to compare the continuous bubble growth with predicted values. As the purpose of the dosing system is to dose small volumes into living cells, the assumed volumes are at maximum ~5% of a round cell of 10 μm diameter, therefore a target dosing volume of 25 fL, see Section 4.6.1. Therefore, in addition to continuous bubble growth, we need to characterize bubble growth with small current pulses, to dose the small incremental volume of liquid samples. Incremental bubble growth with successive current pulses is presented in the next section.

5.5.1   General characterization

Figure 5.11 shows two photographs of a bubble before (left) and after (right) the dosing experiment. The current used is 2 nA and the dosing time is 4 seconds. The red line corresponds with the bubble front, the green line in the right picture starts with the bubble front at the start of the dosing experiment. The ruler is in μm, to convert this to fL a multiply factor of 1.6 is used (channel cross-section area: 10 μm × 0.16 μm). The bubble volume increase, and thus the dosing volume, equals $\Delta V = (102.5 - 46) \times 1.6 = 90$ fL. The graphs of the applied current, voltage and bubble volume against time of this experiment are shown in Figure 5.12.
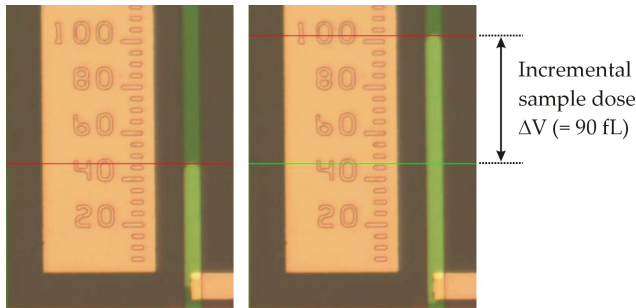
Figure 5.11: *Left: photo of the hydrogen bubble before start of bubble increment experiment, and Right: photo of the hydrogen bubble when the increment has stopped and volume is stabilized. The green line indicates the starting position of the bubble front, the red line the actual position of the bubble front. The difference between these two lines multiplied with the cross-sectional area of the bubble gives the volume increase, in this case $\Delta V = 90$ fL.*

Initially, a base current of 0.3 nA is used to compensate the bubble shrinking caused by hydrogen diffusion out of the bubble, into the channel and silicon nitride. Following 4.7 seconds a 2.0 nA current pulse is applied. It can be seen that the cell potential increases by approximately 2 V, and we estimate that the total capacitance of the system is 1.5 nF (see Section 5.3.2). Therefore, the calculated charging time equals $\Delta t = \frac{UC}{i} = \frac{2 \times 1.5 \times 10^{-9}}{(2.0 - 0.3)10^{-9}} = 1.8$ s, corresponding with the charging time in the graph
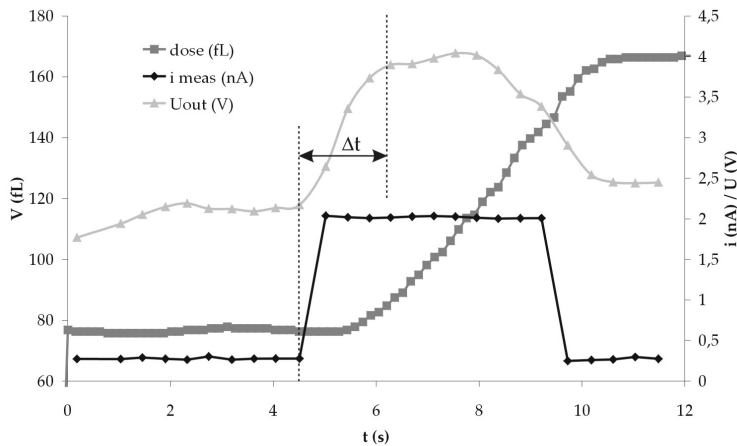
Figure 5.12: *Graphs showing the measured applied current, voltage and bubble volume against time during the dosing experiment.*

shown in Figure 5.12. The resulting volume increase of this hydrogen bubble is 90 fL. Though, the theoretical volume increase equals 209 fL (see Section 5.4). This mismatch between theoretical volume increase and the measured value shows up in every measurement, as can be seen in Figure 5.13, where the volume increments and theoretical expectations, based on the measured bubble growth rate, against applied charge are shown.
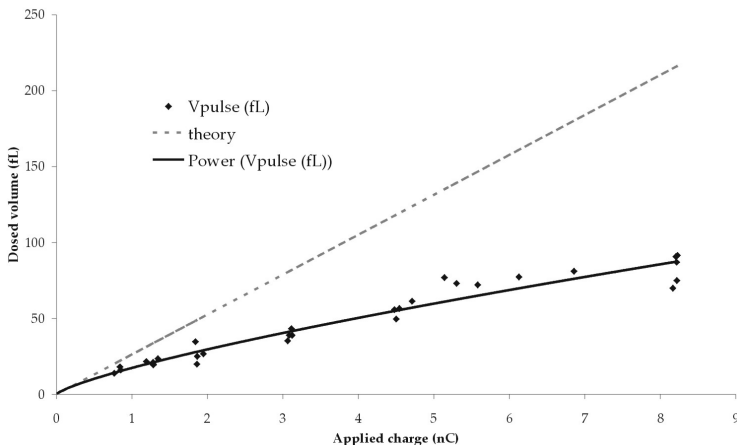
Figure 5.13: *Graph of measured volume increments due to applied current pulses against applied charge, compared with the predicted value, based on the growth rate measured in the dc-measurements.*

The charging and discharging of the parasitic capacitance of 0.6 nF due to the changes in the applied voltage causes delays in the positive and negative bubble growth, but should not affect the total bubble volume increment. Though, we assume that current used for charging and discharging of the double layer capacitance at the cathode is not used for the hydrogen evolution. As the value of this double layer is only 10 pF (5×10 μm^2 $\times$ 20 μF/cm^2), this can not explain the large mismatch compared to the expected value. In Table 5.3 the measured errors per measurement series are shown.

Table 5.3: *Mismatch of volume increments with theoretical expected values listed per measurement series. The values for i and t are set values, not measured values. Q and V are measured average values of 3 - 5 measurements. V_{theory} and correlation (= V/V_{theory} $\times 100\%$) are calculated values.*

i (nA)	t (s)	Q (nC)	V (fL)	V_{theory} (fL)	correlation (%)
0.8	2	0.82	16.0	21.5	72
1	1	1.27	21.6	33.5	63
1	2	1.88	26.6	49.4	52
2	1	3.10	39.1	81.4	48
2	2	4.56	55.8	120	47
2	3	5.80	76.1	153	49
2	4	8.21	82.8	216	40
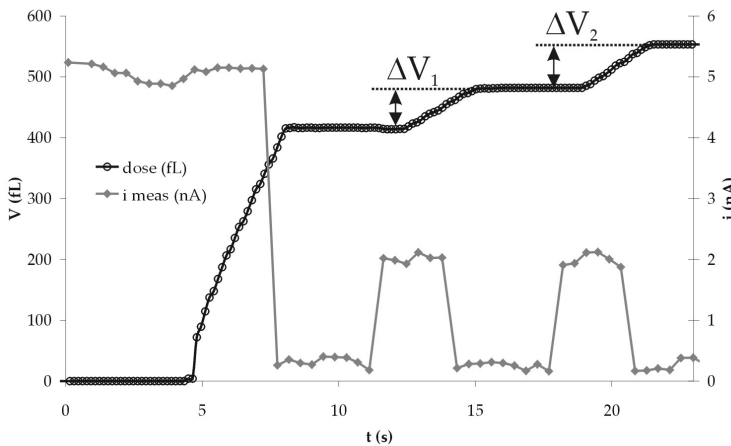
Figure 5.14: *Graph of a measurement combining the constant dc-current bubble growth with pulsed current bubble growth. The growth rate values are 21.0 fL/nC for the initial constant current and 14.4 fL/nC and 15.9 fL/nC for the first and second pulse, respectively. ΔV_1 = 65 fL and ΔV_2 = 71 fL.*

From Table 5.3 it appears that the smaller applied charges have higher correlation with the predicted values than the larger applied charges. For an applied current of 2 nA the correlation appears to be constant at ∼48%, but with longer charging times the cor-

relation with expected values decreases. Figure 5.14 shows a graph of a measurement where first with a constant current a bubble is generated, and after holding this bubble constant in volume, current pulses give increases to the bubble volume. The constant dc-current used for generating the bubble gives a bubble growth rate of 21.0 fL/nC, but the current pulses give bubble growth of 14.4 fL/nC for the first pulse and 15.9 fL/nC for the second pulse. Three other identical measurements gave simular results. We do not know the reason for this large difference in growth rates between constant bubble growth and pulsed bubble growth, and why the growth rates with pulsed currents are far from the theoretical expected values. This can not be explained by losses due to charging and discharging the electrical double layer at the cathode, as its capacitance is only 10 pF.

5.5.2   Volume increments smaller than 25 fL

In Chapter 2 it was stated that one goal in this research is to be able to dose volumes smaller than 25 fL. For that, the system should be able to produce controlled bubble increments smaller than 25 fL. Figure 5.15 shows two photographs of the start and end of a volume increment of 16 fL.
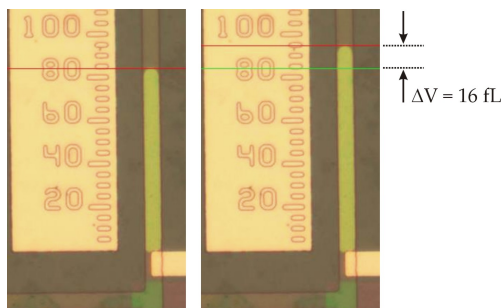
Figure 5.15: *Left: photo of the hydrogen bubble before start of a volume increment of 16 fL, and Right: photo of the hydrogen bubble when the increment has stopped and volume is stabilized. The green line indicates the starting position of the bubble front, the red line the actual position of the bubble front. The channel volume between the red and the green line is 16 fL.*

The accompanying graph of the applied current and bubble volume is given in Figure 5.16. It can be seen that these measurements are near the precision limits of the current source. The precision of the current source is ∼0.05 nA, and for current pulses where $\Delta i = 3.0$ nA, the precision becomes significant. For smaller volume increments the electrical set-up should be changed to achieve a more precise current source. Furthermore, also the optical volume detection for these channels and optical magnification reaches almost the limit, where one pixel of the camera corresponds with 0.33 μm, corresponding to a volume of 0.53 fL. To improve this the cross-sectional area of the channels should be decreased. To avoid higher capillary and hydraulic pressures the preferred dimension to decrease is the width of the channel. Also, the optical magnification can
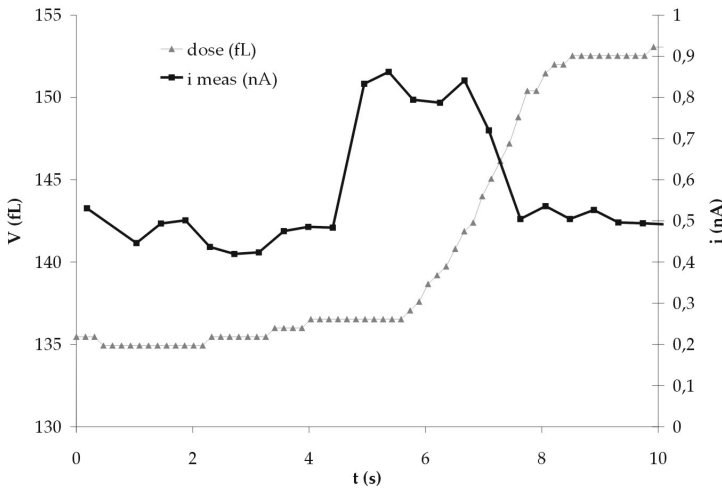
Figure 5.16: *Graph of the applied current and bubble volume of a bubble volume increment of 16 fL.*

be improved.

Three measurements in this data series have been performed, the other two measurements showed volume increments of 14 and 18 fL (not shown), demonstrating that these small volumes are repeatable.

5.6 Bubble shrinking by back-reaction/sample extraction

Corresponding to the bubble growth experiments, this section describes the shrinking of the hydrogen bubbles, that can be used for reversed dosing, i.e. liquid extraction. Three types of measurements have been performed: bubble shrinking by diffusion, free back-reaction by shorting the electrodes and forced back-reaction by applying a negative current.

5.6.1 Bubble shrinking by diffusion

When no current is applied, all bubble shrinking is caused by diffusion. Two measurement series have been performed with two different starting volumes, to see if the bubble size makes any difference in the diffusion. If hydrogen diffuses into the silicon nitride the diffusion rate should increase with bubble size. The bubbles in the first measurement series (graphs shown in Figure 5.17) have an initial bubble length of $\sim$60 μm and volume of $\sim$92 fL. The bubbles in the second measurement series (graphs shown in Figure 5.18) have initial lengths of $\sim$200 μm, and volumes of $\sim$320 fL.

As the bubble pressure for longer and shorter bubbles is equal (the bubble pressure of a bubble in rest is only caused by the capillary pressure, i.e. the pressure caused by the
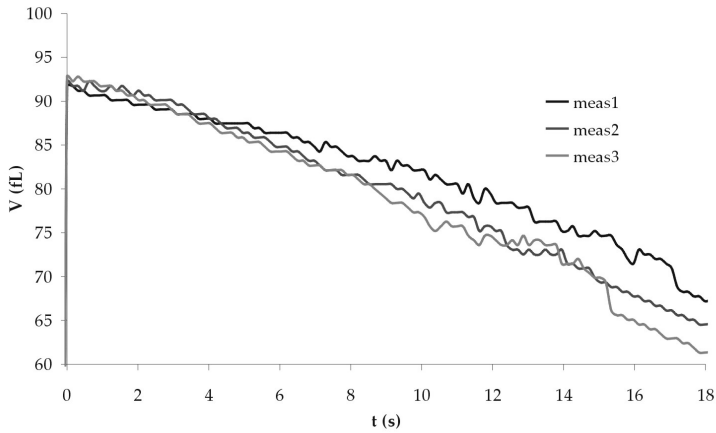
Figure 5.17: *Graph of bubble decrease by diffusion; initial bubble volume ~92 fL.*
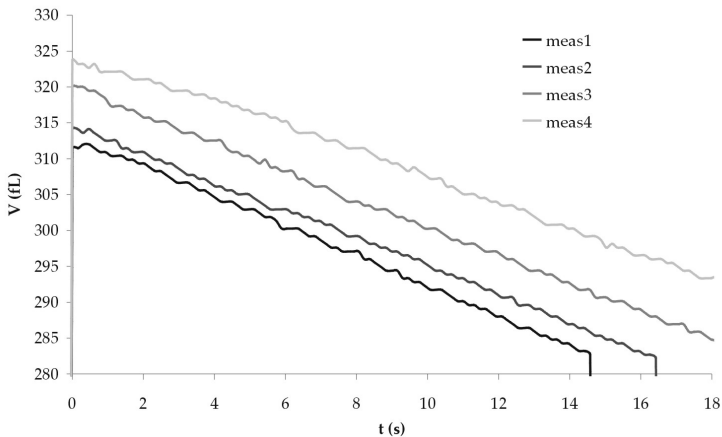

Figure 5.18: *Graph of bubble decrease by diffusion; initial bubble volume ~320 fL.*

meniscus, what is the same for longer and shorter bubbles), the diffusion into the channel is expected to be the same for longer and shorter bubbles in infinitely long channels. For channels with limited length the distance between the channel end and the bubble decreases with bubble length, and therefore, the diffusion gradient between bubble and bulk (with an estimated negligible hydrogen concentration) outside the channel increases. Due to this it is assumed that the diffusion out of the bubble into the channel increases with bubble length and is inversely proportional to the remaining channel length. Due to the larger contact area between bubble and silicon nitride for longer

bubbles it is expected that the hydrogen diffusion into the silicon nitride increases with bubble size. Both graphs show that the diffusion rates for longer and shorter bubbles are comparable, where the diffusion rates for the 60 µm long bubbles equal 1.5 fL/s and that of the 200 µm long bubbles equal 1.9 fL/s. This small difference of 0.4 fL/s could be caused by diffusion of hydrogen into the silicon nitride, or by increased diffusion for the longer bubble. It is assumed it is caused by the latter reason. Close to the electrode the channel appeared to be less clean, possibly causing the bubble to shrink less fluently, as shown in the graph in Figure 5.17.

5.6.2   Free back-reaction

When the electrodes are shorted the redox reaction to form the hydrogen and oxygen is reversed, and hydrogen with hydroxide will react back to water. During this back-reaction current the small electrode will be the anode and the large electrode the cathode and chemical energy will be converted into electrical energy. Figure 5.19 shows a graph where the after ∼2 seconds the electrodes are shorted until ∼7 seconds. After 15 seconds the electrodes are shorted again. To short the electrodes, the battery of the nanoamp source is switched off, therefore, the opamp is switched off. This situation does not represent a complete short, there is still the internal resistance of the opamp. Test have shown, that switching off the battery gave similar results as shorting the electrodes. As completely shorting the electrodes is much more complicated these experiments have been performed by switching off the battery.
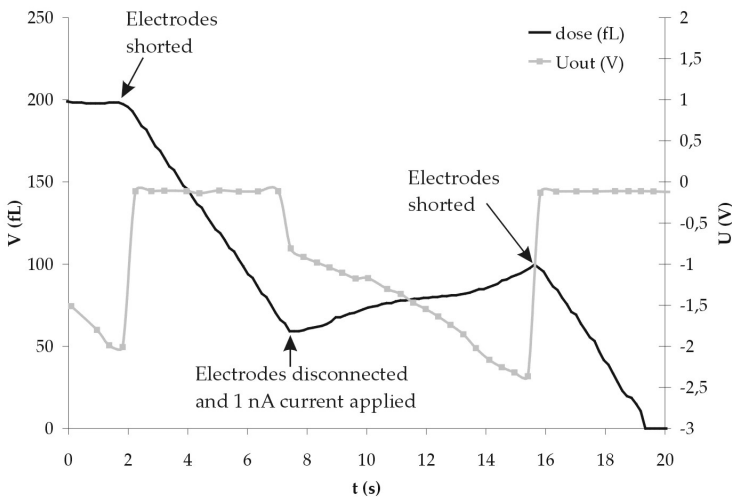

Figure 5.19: *Electrical and bubble volume graphs during electrode short-ing and gas generation. During shorting the bubble size is decreasing and a back-reaction occurs, transforming chemical energy into electrical energy.*

During shorting the potential can no longer be measured, however, the generated current can be measured. It is clear to see that during the electrode shorting, the bubble
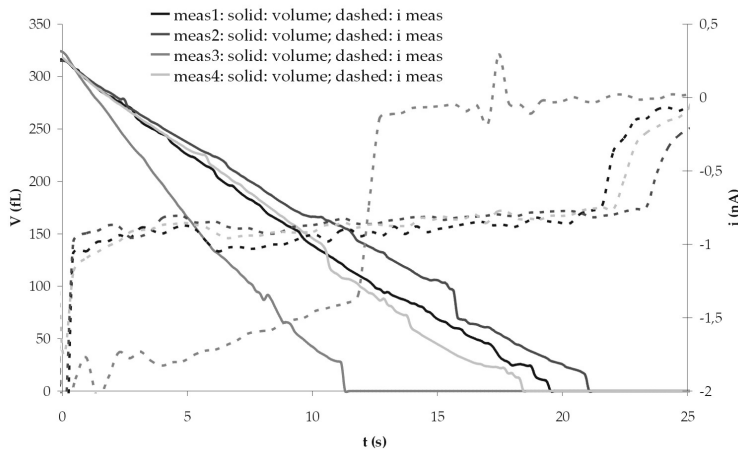
Figure 5.20: *Graphs of the generated current and bubble shrinking when the electrodes are shorted. Simply shorting the electrodes is not useful for controlled volume reduction for femtoliter extraction, because of the differences and instabilities in the gas reduction rates. The dashed curves are the measured generated currents accompanying the solid curves of gas reduction.*

shrinks linearly and electrical current is generated. In between the two shorting steps, the bubble grows due to the 1 nA applied current.

Figure 5.20 shows four graphs of shorted back-reactions until all gas is vanished. All these graphs show a linear decrease of the bubble size, but the gas reduction rates are not all equal, where measurement 3 clearly has a much higher gas reduction rate than the other three measurements. Also, the generated negative current is much higher. Furthermore, all four measurements show, more or less, a declining gas reduction rate during gas reduction. Next, the gas reduction rate appears to be much more sensitive to imperfections in the channel or resistances causing irregularities in the measured curves, especially when the gas volumes are below 150 fL. Therefore, simply shorting the electrodes is not very useful for controlled gas reduction.

5.6.3 Forced back-reaction

To increase the controllability of the gas reduction the current is not freely generated by the back-reaction itself, but applied by the current source. And thus, the back-reaction is forced. This increases the accuracy of the gas volume reduction, as can be seen in Figure 5.21 and 5.22, where graphs are shown of the gas volume reduction using applied currents of -1 nA and -2 nA, respectively. The curves are very linear and repeatable, especially with the applied current of -2 nA. The irregularities that can be seen in the curves in Figure 5.20 have almost completely disappeared and the controllability appears much improved. After ∼18 seconds the hydrogen bubbles of ∼320 fL have completely been vanished using -1 nA. With the -2 nA current the ∼320 fL bubbles have

almost disappeared after close to 10 seconds. A small hydrogen bubble remains and at around 11 seconds this bubble starts to increase, due to oxygen production. The measured oxygen production rate is 12.7 fL/s, corresponding to 6.35 fL/nC. The hydrogen reduction rate is 17.3 fL/nC for -1 nA (17.8 fL/s, measured current is -1.03 nA) and 15.8 fL/nC for -2 nA (32.1 fL/s, measured current is -2.04 nA).
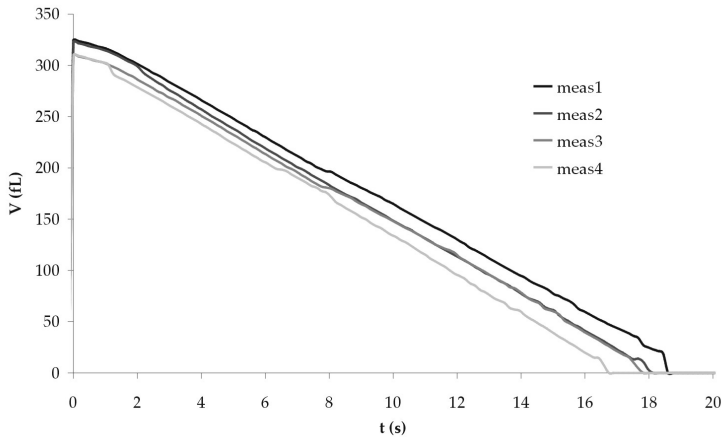

Figure 5.21: *Gas volume reduction curves where an external negative current of 1 nA is applied to control the electrolysis back-reaction. Measured hydrogen bubble volume reduction is 17.3 fL/nC.*

Theoretically, the oxygen production rate should be exactly half of the hydrogen reduction rate, and the hydrogen reduction rates should be the same for -1 and -2 nA. The oxygen bubble growth is almost half of the hydrogen bubble shrinking, a small difference is measured. This is probably due to the fact that the electrolyte has a higher solubility for oxygen than for hydrogen (oxygen: 2.501×10^{-5}, hydrogen: 1.455×10^{-5}, both at 20 °C and 1 atmosphere [5]). The reduction rate for -2 nA is slightly less than for -1 nA, $\sim$9%. Partly, this has to do with the channel resistance, see Section 3.6. The channel resistance causes two small effects that cause the hydrogen bubble reduction rate per applied charge is less for the -2 nA current in respect to the -1 nA current. Due to higher fluid flow caused by faster bubble shrinking for -2 nA currents, with respect to -1 nA, the hydraulic resistance goes up and the internal bubble pressure decreases. Due to the lower bubble pressure hydrogen diffusion out of the bubble to the electrode will be slightly smaller. The calculated difference in bubble pressure is 33 mbar, so this is less than 1% of the total bubble pressure of 4.5 bar. The second effect due to the increased hydraulic resistance is the higher mechanical energy needed for moving the liquid column. This causes a higher overpotential at the electrodes, and therefore a slower back-reaction. It is assumed that the differences in the gas reduction rates by the two different reduction currents is caused by differences in the overpotential, partly caused by the reason mentioned. The other reason could be caused by the diffusion of the ions to the electrode surface through the double layer, faster with higher negative currents.
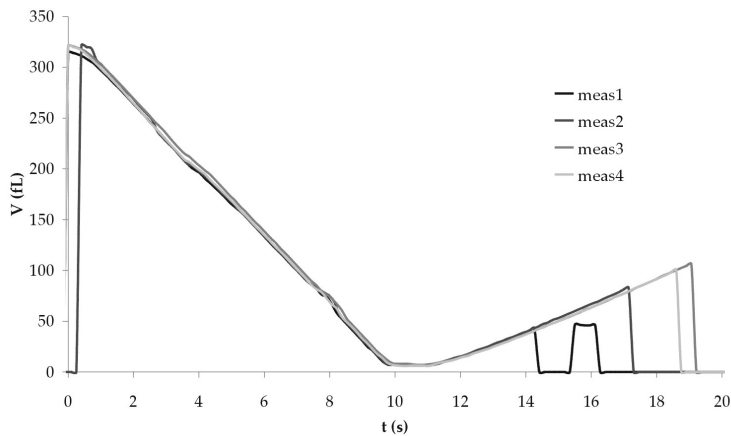
Figure 5.22: *Gas volume reduction curves where an external negative current of 2 nA is applied to control the electrolysis back-reaction. measured hydrogen bubble volume reduction is 15.8 fL/nC. Between ~10-11 seconds a small bubble remains, what grows after ~11 s due to oxygen production. The measured oxygen production rate is 6.35 fL/nC, what is slightly less than the expected value of 7.9 fL/nC, what is 0.5 times the hydrogen reduction rate.*

The graph in Figure 5.23 shows the curves of measured back-reaction rates for the negative currents of 1 and 2 nA, together with the measured diffusion rates (black; average of 16.5 fL/nC), and the corrected curved where the diffusion rate is subtracted (gray; average of 15.3 fL/nC). It is obvious that the curves do not fit the theoretical expectation (28.8 fL/nC), but is about half of the expected value. These measurements have been performed on newer chips and devices than the dc- and pulse measurements, but with the same electrolyte and the same Tween20 concentration. Measurements have shown that the gas reduction is in relation with the gas production in these chips under the same circumstances, which also can be seen in Figure 5.22 where the hydrogen reduction relates to the oxygen production. It appeared that the channel width and the contact angle between electrolyte and silicon nitride at the new chips was not significantly different than the old chips. A possibility could be the presence of a leakage current, although we do not expect that this leakage current can be constant and approximately of the same value as the measured current, over numerous measurements with different applied currents and refreshed electrolyte solutions. Thus, although the gas reduction is related to the gas production in these chips, the reason for the too low rates is not known, but we assume it has to do with some unknown faults in these chips.
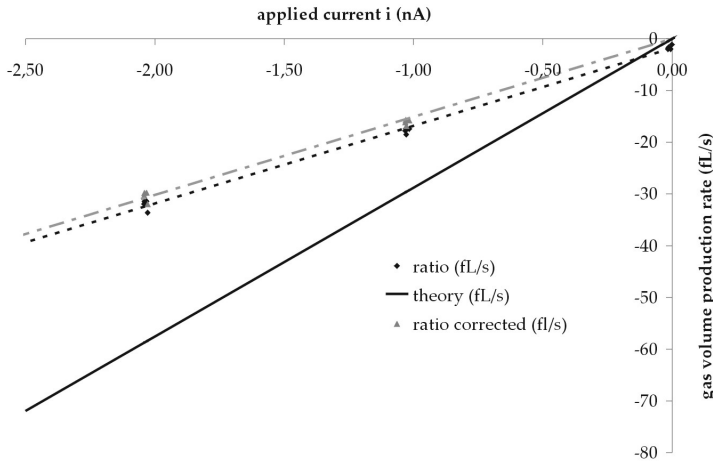
Figure 5.23: *Graph of gas reduction due to an applied negative current. The dashed lines are the linear fits to the measured values. In black are the measured values (average of 16.5 fL/nC) and in gray the corrected values (average of 15.3 fL/nC) to the diffusion, measured with a constant current of 0 nA. The measured values are approximately half of the theoretical expected values of 28.8 fL/nC. The reason for this is not known, although the gas reduction relates to the gas production for these chips.*

5.7   Sample transportation through the nanochannel

This section describes that the gas bubbles in nanochannels actually can be used for a pumping mechanism. Using hydrogen bubbles for dosing liquids in microchannels is not new (see Chapter 2), but in nanochannels it is.

Figure 5.24 shows two pictures of a gas bubble being pushed by another expanding gas bubble. The distance between the two gas bubbles remains ∼80 μm over a displacement of ∼75 μm, or a dosing volume of ∼120 fL.

Photographs in Figure 5.25 show a gas bubble passing the T-junction towards the anode chamber and the electrical by-pass channel towards the needle exit. These images demonstrate that the fluid flow is not affected by the anode chamber and only slightly by the by-pass channel. The bubble enters the by-pass channel over a distance of 12 μm, about 6.5% compared to the distance from the T-junction to the needle exit. Thus, for this chip the resulting dosed volume at the needle exit is 100/(100+6.5)=94% of the bubble growth. This is more than the predicted value of 84%, see Section 4.6.2, and therefore the measured final dosing volume compares to the produced bubble growth even better than the theoretical expectation.

Photographs of actual dosing through the needle exit are shown in Figure 5.26, where hydrogen gas is ejected. Energy needed for gas ejection to overcome the gas passing critical edges [6] causing pressure to build up inside the bubble, which is released

Figure 5.24: *Proof of dosing due to gas production. The distance between the two bubbles (light colored) remains ~80 μm over a displacement of ~75 μm, or a dosing volume of ~120 fL.*
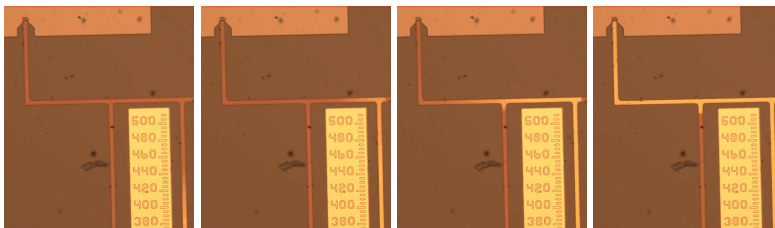

Figure 5.25: *Photographs of a growing bubble moving towards the needle exit, passing the T-junctions to the anode chamber and the electrical by-pass channel. The measured volume flow towards the needle exit is 94% of the total generated volume flow.*
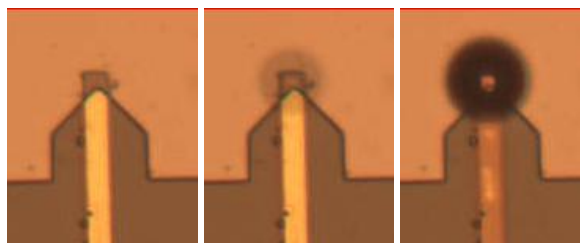

Figure 5.26: *Photographs of gas exiting the needle and forming a spherical bubble at the needle exit. Proof of ejection by the needle exit due to the electrochemical dosing.*

when the hydrogen bubble exiting the needle exit is formed. The estimated diameter of the bubble in the last picture is 18 μm, and therefore the exiting bubble has a vol-

ume of 3.0 pL. The internal bubble pressure equals $p_{bubble} = p_L + p_{cap}$, where p_L is the pressure inside the bulk liquid covering the chip and is approximately the atmospheric pressure, and p_{cap} is the capillary pressure inside the ejected bubble, calculated using the Young-Laplace equation, see Equation 3.18. The calculated internal bubble pressure equals $p_{bubble} = p_0 + p_{cap} = 101 \times 10^3 + 0.032/9 \times 10^{-6} = 105 \times 10^3$ Pa = 1.05 bar. The total amount of gas in the ejected bubble is therefore approximately 127 fmol. This amount of gas is ejected in 0.31 s (the time between three frames), and therefore during this ejection the rate is 0.41 pmol/s. The applied current was 20 nA, thus generates a gas production rate of 103 fmol/s, so $\sim \frac{1}{4}$ times the ejection rate. The time between full bubble at the needle exit (right photo in Figure 5.26) and the gas reaching the needle exit (right photo in Figure 5.25) is 1.24 seconds. This corresponds with a hydrogen production of $1.24 \times 103 = 128$ fmol, thus is equal to the total amount of gas ejected. In the right image in Figure 5.26 some electrolyte has entered the channel, on the order of 40 fL. We assume that this is a result of the very fast gas transfer into the ejected bubble, and the pressure changes accompanying this.

5.8 Conclusions

In this chapter we have described the characterization results of the femtoliter dosing system. In most experiments the results fitted very well to the theory, and in some experiments the error was a factor of 2.

The nucleation fits well to the theory. The nucleation position was mainly at the designed position and in most cases the bubble folded nicely around the cathode and stopped at the height step, as designed. The total time needed for nucleation was longer than expected, due to an increase in charging time of the electrical double layers at the electrodes and the parasitic capacity with the silicon substrate. This increase in charging time is assumed to be caused by the increase in solution resistance, due to long ion migration times. The measured value of the capacitances was with 1.5 nF higher than the expected value of 0.6 nF. The nucleation time depends very much on the required level of supersaturation. From the measured nucleation time the calculated supersaturation fitted very well with published data, and therefore the nucleation time fits very well with the theory.

The constant gas growth experiments showed constant and linear gas volume increases. The measured values for bubble growth rates were over a wide range of applied currents (2, 3, 4, 5, and 6 nA) approximately 9% lower than the theoretical expected value. Best results were measured with an applied current of 2 nA, where the measured growth rate is 26.8 fL/nC, compared to the theoretical value of 28.8 fL/nC. These small errors are within the expected error range, and therefore the linear bubble growth fits very well with the theory.

The experiments with pulsed currents to dose small volumes is the most important section of this chapter as it shows the possibility of this femtoliter dosing system for dosing very small samples into cells. The goal of the dosing experiments was to dose controlled volumes smaller than 25 fL, as that is ~5% of an average sized mamalian cell. It has been assumed that a living mamalian cell can maintain viability when these small values are injected into, or extracted from, the cells. We have achieved repeatable dosing volumes around 16 fL, so this important goal has been achieved. Although the

dosed volumes are very repeatable, the correlation of the measured dosing volumes with the expected volumes starts at 72% for the 16 fL volumes, but goes down to 40% for volumes just over 80 fL. The reason for this large error is not known.

In order to extract a volume sample from a cell, gas volume reduction is needed. This is achieved by the back-reaction of the electrolysis reaction: the anode and cathode are reversed and hydrogen and hydroxide react back to water. Free back-reaction, where the electrodes are simply shorted gave unsatisfactory results: the volume reduction rate was not constant. For precise femtoliter volume extraction forced back-reaction is more convenient, where the rate is controlled by the applied negative current. Very linear results for -1 and -2 nA currents are achieved. The measured shrinking rates of 15.3 fL/nC correlate with the growth rates of this chip, but not with the theory (28.8 fL/nC) and the measured growth rates in the dc-measurements (26.8 fL/nC). The dc- and pulse measurements have been performed with the same chip, but the bubble shrinking measurements have been performed on another chip. It is assumed that these errors are caused by some unknown faults in this chip.

Gas flow measurements have proven the concept of an electrochemical femtoliter dosing system in nanochannels as expanding hydrogen bubble has transported other hydrogen bubbles through the channel with a constant distance between the bubbles. The fluid flow through the channels towards the needle exit has been shown and functions even better than theoretically expected. Finally, actual visible dosing from the needle exit has been achieved by dosing a hydrogen bubble of 127 fmol gas into the bulk solution on top of the chip. The measured dosed amount of gas compares very well with the theoretical expected value of 128 fmol.

Therefore, we can state that the characterizing experiments achieved very satisfactory results and the goal of dosing volumes smaller than 25 fL has been achieved with dosing volumes of ~16 fL.

Bibliography

[1] R. Miller, V.B. Fainerman, M.E. Leser, and M. Michel. Surface tenison of mixed non-ionic surfactant/protein solutions: comparison of a simple theoretical model with experiments. *Colloids ans Surfaces A: Physicochemical and Engineering Aspects*, 233:39–42, 2004.

[2] G. M. Barrow. *Physical chemistry*. McGraw-Hill, 6 edition, 1996.

[3] B. Yazici. Hydrogen evolution at platinum (Pt) and at platinized platinum Ptz cathodes. *Turkish Journal of Chemistry*, 23:301–308, 1999.

[4] S. Shibata. The concentration of molecular hydrogen on the platinum cathode. *Bulletin of the Chemical Society of Japan*, 36:53–57, 1963.

[5] D.R. Lide. *Handbook of Chemistry and Physics*. CRC, 74 edition, 1993-1994.

[6] F. Goldschmidtboeing, M. Rabold, and P. Woias. Strategies for void-free liquid filling of micro cavities. *Journal of Micromechanics and Microengineering*, 16:1321–1330, 2006.

Chapter 6

Cell membrane penetration with planar micromachined silicon nitride micro/nanoneedles

This chapter presents cell membrane penetration experiments, which have been performed with hollow nanoneedles integrated in a femtoliter dosing system and K562-cells. Successful penetration has been achieved, with low estimated indentation depth, indicating low cell damage. Preliminary results based on optical inspection have not indicated severe cell damage within 30 minutes after penetration. Nanoneedle integrity was confirmed during all cell penetration experiments. Based on reported literature we expect maintaining cell viability.

6.1   Introduction

The first time needles, or micropipettes, were used for intracellular mass transport was performed with in vitro fertilization in the 1970's, where a male sperm cell was injected into a female egg cell to achieve fertilization [1]. The egg cells in this studies are approximately 10 times larger than average mammalian cells, and the needle in this studies has a diameter of tens of μm, what is far too large for normal sized cells of approximately 10 μm in diameter. On the other hand, there are the carbon nanotubes, with a diameter of a few nm. These carbon nanotubes are used in neural research for measuring electrical signals directly from the brain or nerve tissues [2]. A drawback of these carbon nanotubes is that they can not be integrated with an microfluidic network, and therefore, are not suitable.

The combination of recent technological achievements of decreased needle sizes and established microfluidic delivery systems (Chapter 2) opens up new possibilities for research on the single-cell level. Several micromachined microneedles for cell membrane penetration have been reported. Wong et al. have produced micromachined micropipettes and single-cell traps for drug injection, but are not suitable for chip integration [3]. Others are suitable for chip integration, like on-chip microneedles for cell membrane penetration. These needles are not suitable for injection, as the needles are not hollow [4]. Lipid-assisted intracellular mass transport has shown to be a very gentle

way, where the membranes fuses with lipids on the needle, and therefore, the membranes opens up without being penetrated [5]. Due to the difficult aligning of such a system, this system is not very useful to be integrated in an IMBID system.
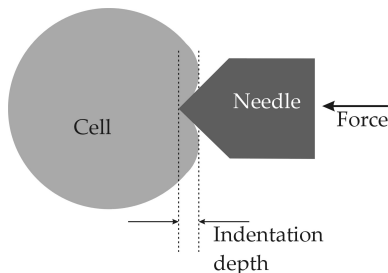

Figure 6.1: *Schematic of the indentation depth of the cell membrane before penetration by a needle.*

It has been reported that mechanical stress causes various changes in cell activity [6; 7]. It is suggested that a distance of indentation before penetration less than 1 μm causes low mechanical stress in average sized cells (see Figure 6.1), and because of that low changes in cell activity [7]. After the first reports of microneedles penetrating the cell membrane, Obataya et al. investigated the required penetration force and measured the indentation depth [8]. They attached silicon based sub-micron tip microneedles to AFM-tips and measured the penetration force and reported the indentation depth. Several different needle designs (cone, pyramid, cylinder and prism) and different diameters (200 – 800 nm) were tested. The best results, based on lowest penetration force and indentation depth, were achieved with 200 nm diameter cylinder silicon nanoneedles with a measured force of 0.65 nN, a penetration probability of 92% and an indentation depth of 610 nm. The prism nanoneedle, with 800 nm base dimension, gave about the same force (0.67 nN), but a lower probability (56%) and a higher indentation depth (1900 nm). They showed that the needle tip shape is as important as the needle tip size, where cylindrical shapes needed less force and reached less indentation before penetration than cone-like shape needles needed, see Figure 6.2. We assume that cylindrical needles, with a radial frontal area, cause large stress in the cell membrane at positions where the corner of the needle tip is in contact with. This results in rupture of the membrane locally, followed by penetration, with lower indentation depth and penetration force than with prism needles. Therefore, we expect easy cell membrane penetration with small needles with radial front sides, as is the case with our nanoneedles where the tip has a rectangular shape with a width of 2 μm and a height of 300 nm, see Figure 6.3. The rectangular tongue has a length of 2 μm, which is longer than the expected indentation depth, and therefore, sufficiently long to penetrate the cell membrane before the larger part of the nanoneedle reaches the cell.

After penetration of the cell membrane with the rectangular tongue, we expect that the remaining nanoneedle will penetrate the cell membrane with ease. Han et al. showed cell membrane penetration with nanoneedles till 600 nm diameter attached to AFM tips without leakage and cell death after 150 minutes [9]. To achieve hollow nanoneedles width dimensions small enough to maintain cell viability, it is clear that
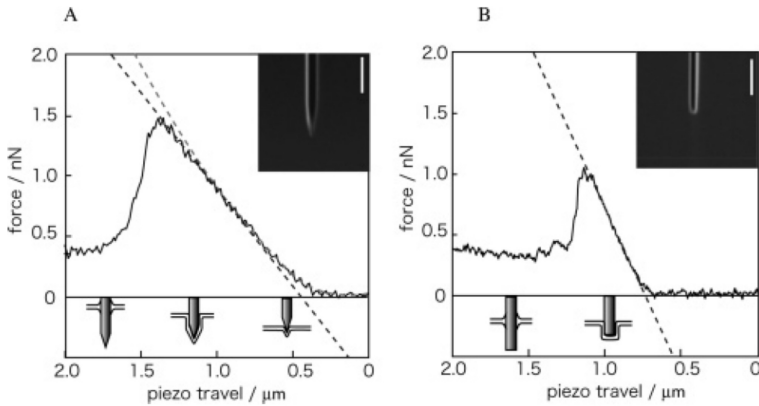
Figure 6.2: *Figure taken from Obataya et al. [7] showing typical force–distance curves for a human epidermal melanocyte using 200–300 nm diameter nanoneedles that have cone-like shapes (A) and cylindrical shapes (B) at the edges. Insets show magnified SEM images around the needle tip. By Obataya et al. proposed situations of the needle tip and the cell surface are depicted under the plots.*

these needles must be integrated with nanochannels.

No reports have been found of the influence of the needle material or the use of biocompatible coatings on the penetration characteristics. As the cell membrane is a lipid bilayer and consists of a polar outside and a non-polar inside [10], the hydrophilic properties of the nanoneedle surface might have an influence on the opening of the membrane. Furthermore, no reports have been made of silicon based planar sub-micron tip microneedles on the penetration of the cell membrane. This chapter shows the penetration of the cell membrane by planar silicon nitride nanoneedles.

6.2   Materials and methods

6.2.1   Nanoneedles

The silicon nitride nanoneedles are fabricated as described in Section 4.3.3, with nanochannels through the needles as described in Section 4.6.3 and the through holes are etched as described in Section 4.5.3. The silicon nitride layers have thicknesses of 300 nm and channel height of 160 nm, resulting in a total needle thickness of 760 nm. See Figure 6.3 for a schematic of the nanoneedles with the dimensions and the position of the needles in respect to the through hole. These through holes make top and down illumination possible, to improve the visibility of the cells.

As described in Section 4.5.3 the fabricated through holes are not exactly the same as designed, as can be seen in Figure 6.4. This results in poor visibility of cells close to the edge of the through hole, and thus close to the needle. Light projection under an angle was used to minimize this problem.
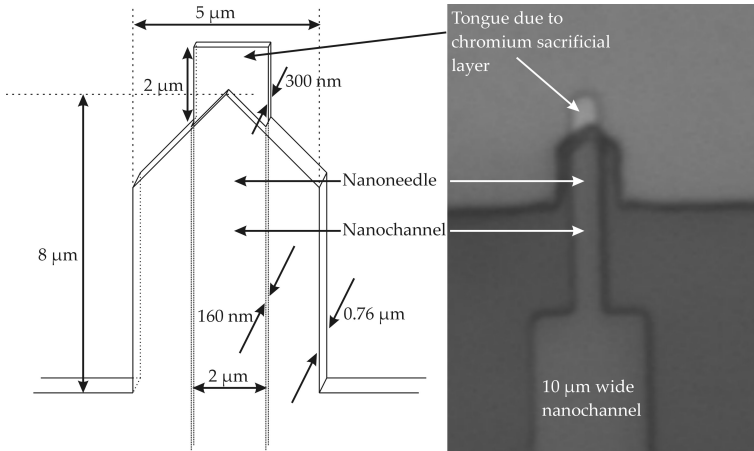
Figure 6.3: *Left: schematic of the nanoneedle, and Right: microscope photograph of a fabricated hollow nanoneedle.*
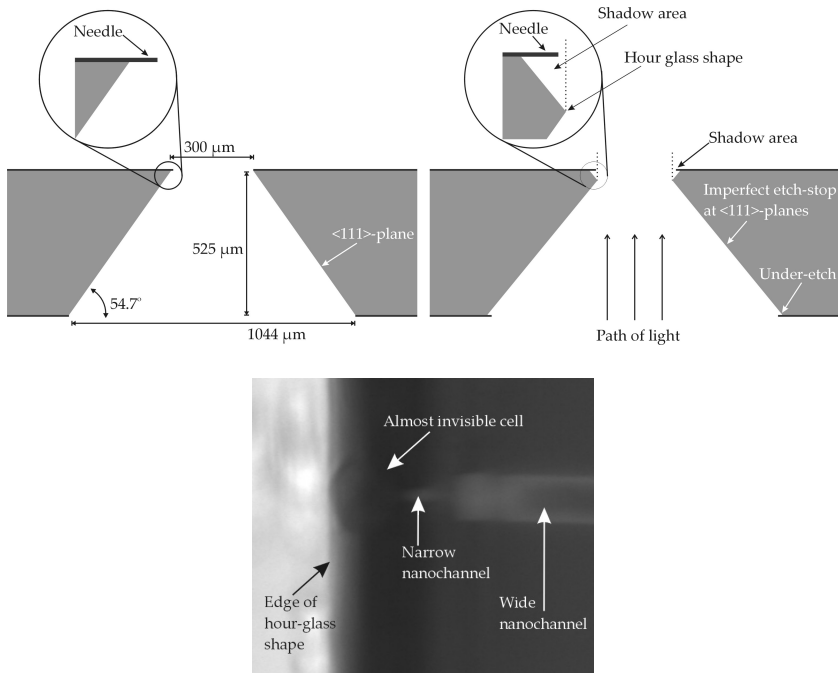

Figure 6.4: *Top: schematics of the through holes: Left: the designed through hole; Right: the resulting through hole. Bottom: photo of a cell at the needle tip, with poor visibility due to the shadow of the hour glass protrusion.*

The wafers are not cut into small chips to prevent damage done to the fragile nano-needle. Before the experiments the wafers were cleaned with ethanol and dried without the use of pressurized nitrogen. Experiments are performed with either uncoated or fluorescently coated needles. Fluorescent coating was done using a drying solution with a low concentration of green fluorescent protein (TurboGFP, Evrogen, Moscow, Russia).

6.2.2 Cells

All needle penetrations were carried out with K562 cells, a specialized cell-line of human erythroleukemia cells. They have been selected for their robustness, nonadherent property and size of ∼15 μm, which is around 50% larger than the average mammalian cell. The K562 cell lines were cultured in RPMI Glutamax medium (Invitrogen, Carlsbad, CA, USA) supplemented with 10% FCS and incubated at 37°C under 5% CO_2. Cells were fluorescently labeled using Acridine Orange (Invitrogen) by incubating the cell suspension in phosphate buffered saline (PBS) containing 0.01 mg/mL Acridine Orange for 10 min, or CFSE (carboxy-fluorescein diacetate, succinimidyl ester, Invitrogen) by incubating the cell suspension in PBS containing 5 μM CFSE for 15 min. Before labeling the cells are washed with PBS twice. The cell concentration was 10^5 cells/mL.

6.2.3 Experimental set-up

A long working distance non-inverted microscope is used (BL51, Olympus) with a motorized stage (Ecodrive, Märzhäuser, Wetzlar-Steindorf, Germany). The wafer with cell suspension is placed on top of a transparent box. The transparent box is placed on the motorized stage. Bottom illumination is achieved using external fiber optics (Schott, Mainz, Germany) and a revolving 45° mirror inside the transparent box, top illumination is performed by the microscope. With top and bottom illumination the cells in the through holes of the chip are much better visible. To increase visibility of cells close to the nanoneedle, experiments are performed with fluorescent cells and nanoneedles, where the emission and excitation wavelengths of the cell and needle dyes used are suitable for the same fluorescence optical filter. Fluorescent experiments are performed with a mercury lamp and standard FITC fluorescence filter (U-MWIBA3, ex: 460-495 nm, em: 510-550 nm, dicromatic: 505 nm, Olympus). Microscope images are taken with a CCD camera (Orca ER, Hamamatsu Photonics, Hamamatsu city, Japan) and captured with an Olympus software package.

The cells can be captured by a glass micropipette (GC150TF-15, Clark Electromedical Instruments, Reading, UK), which is connected to an adjustable under pressure. A hanging water column is used to create the underpressure, a valve system can regulate the under pressure in the micropipette. The micropipette is placed in a holder that is attached to a 3-d micromanipulator (three micromanipulators are combined to achieve a 3-d micromanipulator, Micromanipulator company, Carson City, NV, USA). For pulling the micropipettes (GC150TF-15, Clark Electromedical Instruments, Reading, U.K.) to a an outer diameter of 2 μm we used a P-97 micropipette puller (Sutter Instrument, Novato, CA, USA). To minimize cell adhesion to the micropipette, the micropipettes were coated with SigmaCoat (Sigma-Aldrich, St. Louis, MO,USA). Figure 6.5 shows a schematic of the experimental set-up.
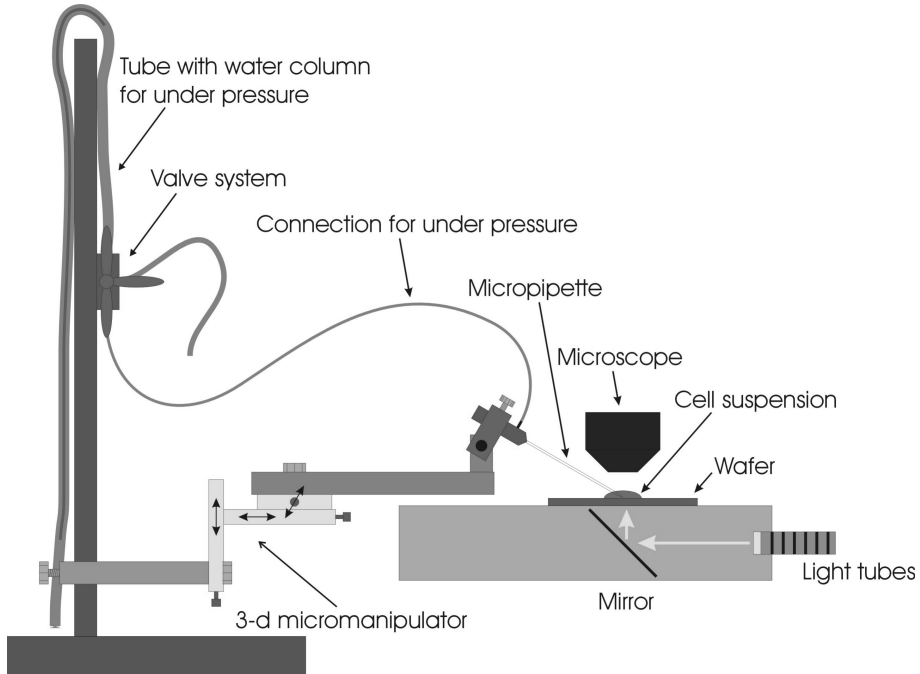
Figure 6.5: *Schematic drawing of the experimental set-up.*

6.2.4   Experiments

Goal is to penetrate the cell membrane of a viable cell with the needle tip without damaging the cell. To minimize the cell destruction the indentation depth should not exceed more than approximately 1 µm. Two methods have been used:

- Cell grab method: Grab a cell with the micropipette using under-pressure and release it at the needle tip using over-pressure. For the pressures the tube and valve system is used, see Figure 6.5. Under-pressure is achieved using the water column and over-pressure is achieved by a small blow by the mouth. A cell captured using the cell grab method is shown in the left photograph of Figure 6.6.

- Cell push method: Grab a cell with the micropipette; this cell is called the *sacrificial cell*. This *sacrificial cell* is used to push another cell at the needle tip. This method is more gentle to the pushed cell as the cell does not get damaged by the harsh micropipette tip, but is much harder to control, especially in the z-direction. See right photograph in Figure 6.6.

Due to the difficulty to place cells at the needle tip using the cell push method, most cells are placed at the needle tip using the cell grab method.

For increased visibility of the cells near the needles, and for possible use of a confocal microscope for detection of successful cell membrane penetration, fluorescent dyes are used to stain the cells and the needles. The dyes are selected in such a way that the excitation wavelengths and emission wavelengths are almost identical, so during cell
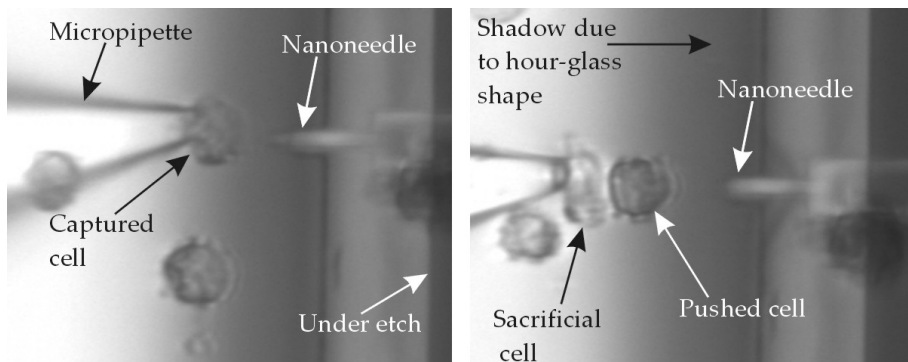
Figure 6.6: *Two methods to place a cell at the needle tip. Left: grab a cell by the micropipette using under-pressure and release it at the needle tip using over-pressure. Right: push a cell with a grabbed cell to the needle tip. More gentle, but much more difficult to control.*

handling both stained needles and cells are visible in the same captured image using the same optical filter. Table 6.1 shows the used dyes and filter with their excitation and emission wavelengths.

Table 6.1: *Excitation and emission wavelengths of the used dyes and filter.*

Dye	Object	Excitation (nm)	Emission (nm)
Acridine Orange	cells	502	526
CFSE	cells	492	517
TurboGFP	needles	482	502

Filter	Dicromatic (nm)	Excitation (nm)	Emission (nm)
U-MWIBA3	505	460-495	510-550

6.3   Results and discussion

The first experiments were to achieve suitable needle staining. Although needle staining appeared to be possible, as can be seen in Figure 6.7, it gave some problems. During drying of the TurboGFP solution the liquid flows into the corners, transporting the TurboGFP. This results in a increased concentration of TurboGFP in the last drying liquid in these corners. Due to under etching of the silicon nitride around the through hole such a corner is located directly next to the needle, causing a very high fluorescent background intensity close to the needle. Such increased background intensity can be seen in the left side of the through hole shown in Figure 6.7. As this background intensity is much higher than the fluorescent intensity of the cells, it appeared to be impossible to achieve a suitable coating for the needles without over-illumination by background fluorescence.

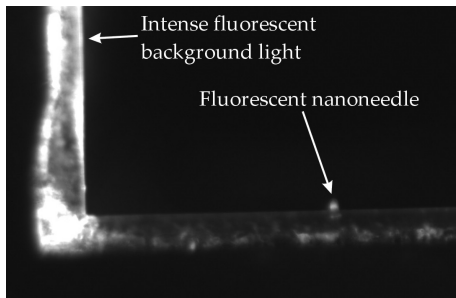   Further experiments were performed without stained needles. Cells remained

Figure 6.7: *Microscope photograph of the emitted fluorescence by Tur-boGFP stained needle and edge of the through hole.*
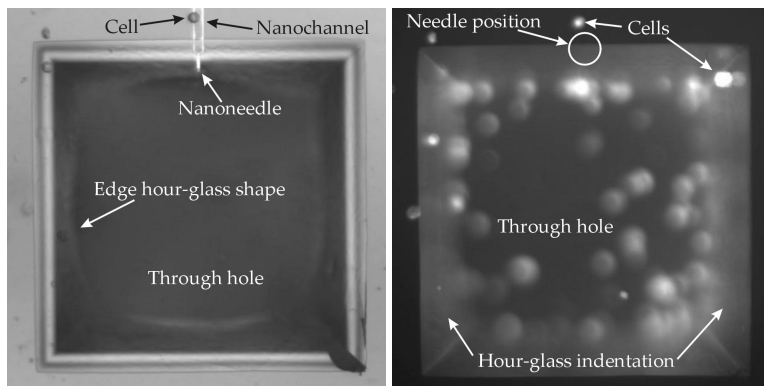

Figure 6.8: *Left: photograph of chip with cells with bright light, cells are hardly visible; Right: same picture under fluorescent light, stained cells are clearly visible, unstained needle is not.*

stained for possible use of a confocal microscope for imaging a successful cell membrane penetration. Figure 6.8 shows the visibility problem with two microscope photographs of the same picture: in the left picture the needle is clearly visible (bright field illumination) and in the right picture the cells are clearly visible (fluorescent light), but not both in the same picture. No bottom illumination is used in this picture.

Successful repeatable cell membrane penetrations have been achieved using the cell grab method, see Figure 6.9. During the experiment, no obvious cell membrane indentation was observed through the microscope, and therefore we estimate the indentation depth is less than 1 µm and no severe damage to the cell is expected. Obataya reported indentation depths of 610 nm for 200 nm diameter cylinder and 1.9 µm for a 800 nm prism [8]. Based on these numbers we expect deeper indentation than 610 nm, but far less than 1.9 µm because of the 300 nm thick tongue that penetrates the cell membrane as first. We assume that once the cell membrane has been penetrated, it will be cut open to a larger hole with ease to make it possible that the larger part of the nanoneedle enters
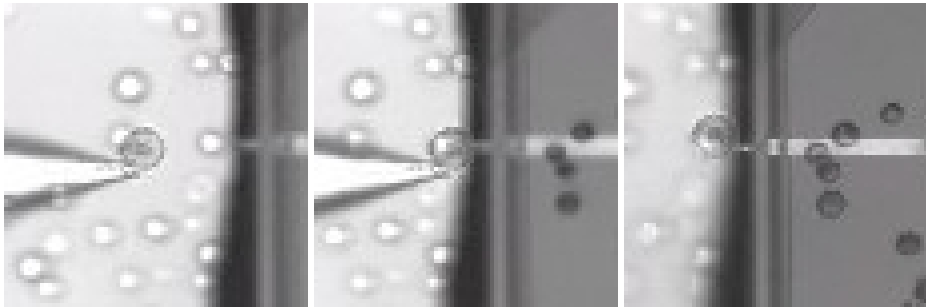
Figure 6.9: *Photo series of a successful placement of K562 cell at the needle tip, using the cell grab method. During cell membrane penetration indentation is hardly visible and therefore assumed to be less than 1 μm. Cell seems to be undamaged.*

the cell. This resulted in an indentation depth that was not noticeable.

During and after the penetration the cell maintained its shape. After the penetration the cell appeared to be fixed at the needle and it could rotate slightly around the needle/cell membrane interface, indicating successful penetration. Cells could be removed from the tip easily using the cell grab method.

The tips of the micropipettes break very easy when touching the chip. These broken tips can damage the grabbed cells. Although the viability of the cells has not been investigated, we can state that using micropipettes with broken tips, the viability of the grabbed cells can decrease dramatically, as sometimes cell destruction could be observed. When cells were grabbed gently with a good tip, no destruction was observed, and the cell kept the original shape. However, using optical tweezers for placing the cells at the needle tip could be a more gentle option. Successful experiments where cells were pushed by trapped 2 μm latex microbeads have been reported [11]. As the optical trapping force of microbeads is higher than of cells [12; 13], and the cell is less affected by the laser light due to the fact the cell is not situated in the optical trap, more force and higher laser power can be applied for transporting the cell. The maximum forces with which these beads could be transported by the optical tweezers are in the range of several pN [12]. Trapping multiple beads could supply the required cell membrane penetration force using our nanoneedles, what is expected to be in the sub-nN range based on literature [7]. Therefore, optical tweezers might me a successful alternative for placing the cells at the needle tip.

Measurements where a cell was placed at a needle tip for more than 30 minutes showed no changes in cell shape, indicating that no severe damage was done to the cell and the cell remained viable for at least 30 minutes. Successful cell penetration was confirmed by the rotation of the cell around the penetration site. However, conventional viability experiments were not possible using the current experimental set-up, as during cell transfer from the cell solution into RPMI cell culture medium the cells were released from the micropipette by the meniscus of the droplet covering the chip. Therefore, we have no results on cell viability over periods more than 30 minutes after cell membrane penetration. Since the cell maintained its original shape for more than 30 minutes, no

indentation depths were observed and cell viability after membrane penetration has been reported in literature [9], we believe that the cell membrane penetration of K-562 cells by our needles does not affect the cell viability.

6.4   Conclusions

Successful cell membrane penetrations have been achieved. Based on the low indentation depth (below measurement resolution ∼1 μm) we do not except severe cell damage. Although, cell viability should be thoroughly investigated, based on the observed indentation depth and according to reported cell penetration experiments, maintaining cell viability is expected.

Positioning of a cell at the needle tip remains difficult. Using an external micropipette introduces high risk of cell damage, and therefore decreased viability. The use of optical tweezers may be used to position the cell at the needle tip. The accompanying confocal microscopy could be very useful to image the actual penetration characteristics.

Due to the low refractive index of the cells top-side illumination appears to be insufficient. To increase visibility of the cells close to the needle direct pathway of the down-illumination to the micro/nanoneedles should be guaranteed, which was not the case with the fabricated chips where the through hole had a hour-glass shape. Fabrication of through holes with the use of DRIE (see Section 4.5) removes the shadow close to the needle, caused by the hour-glass shape, and reduces the under-etching of the silicon nitride around the through hole. Reducing this under-etch might reduce the fluorescent background light using fluorescent labeled needles, and therefore it might be possible to combine fluorescent labeled cells with fluorescent needles, increasing the imaging possibilities of a confocal microscope.

Acknowledgments

Bibliography

[1] P.C. Steptoe and R.G. Edwards. Birth after the reimplantation of a human embryo. *Lancet*, 2:366, 1978.

[2] D. Pantarotto, J.P. Briand, M. Prato, and A. Bianco. Translocation of bioactive peptides across cell membranes by carbon nanotubes. *ChemComm*, pages 16–17, 2004.

[3] P.K. Wong, U. Ulmanella, and C.M. Ho. Fabrication of microsurgical tools for single-cell intracytoplasmic injection. In *MEMS2003 conference proceedings*, pages 359–362, 2003.

[4] T. Ichiki, Y. Sugiyama, S. Kase, and Y. Horiike. Surface micromachined hollow microneedle array integrated on a microfluidic chip. In *μTAS2003 conference proceedings*, pages 1025–1028, 2003.

[5] I. Laffafian and M.B. Hallett. Lipid-assisted microinjection: Introducing material into the cytosol and membranes of small cells. *Biophysical journal*, 75:2558–2563, 1998.

[6] R.M. Hochmuth. Micropipette aspiration of living cells. *Journal of Biomechanics*, 33:15–22, 2000.

[7] I. Obataya, C. Nakamura, S.W. Han, N. Nakamura, and J. Miyake. Nanoscale operation of a living cell using an atomic force microscope with a nanoneedle. *Nano Letters*, 5:27–30, 2005.

[8] I. Obataya, C. Nakamura, S.W. Han, N. Nakamura, and J. Miyake. Mechanical sensing of the penetration of various nanoneedles into a living cell using atomic force microscopy. *Biosensors and Bioelectronics*, 20:1652–1655, 2005.

[9] S.W. Han, C. Nakamura, I. Obataya, N. Nakamura, and J. Miyake. Gene expression using an ultrathin needle enabling accurate displacement and low invasiveness. *Biochemical and Biophysical Research Communications*, 332:633–639, 2005.

[10] D. Boal. *Mechanics of the cell*. Cambridge University Press, 1st edition, 2002.

[11] E. Ferrari, V. Emiliani, D. Cojoc, V. Garbin, M. Zahid, C. Dureux, M. Coppey-Moisan, and E. Di Fabrizio. Biological samples micro-manipulation by means of optical tweezers. *Microelectronic Engineering*, 78-79:575–581, 2005.

[12] R.A. Flynn, A.L. Birkbeck, B. Gross, M. Ozkan, B. Shao, M.M. Wang, and S.C. Es-
     ener. Parallel transport of biological cells using individually addressable vcsel ar-
     rays as optical tweezers. *Sensors&Actuators B*, 87:239–243, 2002.

[13] Y.-R. Chang, L. Hsu, and S. Chi. Optical trapping of a spherically symmetric
     rayleigh sphere: a model for optical tweezers upon cells. *Optics communications*,
     246:97–105, 2005.

Chapter 7

The potential of autofluorescence for the detection of single living cells for label-free cell sorting in microfluidic systems

This chapter demonstrates possibility to use the autofluorescence signal of the cells as a sorting criterion. The ultimate goal of the NanoSCAN-project is to develop an automated chip for single cell analysis. In this automated IMBID system detection and sorting of certain cells on chip is a sub-goal.

7.1 Introduction

Several *in vivo* and *in vitro* studies have evaluated the use of light-induced autofluorescence (AF) spectroscopy and imaging adjunctively with standard diagnostic techniques, such as endoscopy and bronchoscopy, in order to distinguish normal from diseased human tissues [1]. For a given excitation wavelength, there are inherent differences in intensity and spectral shape between the in vivo AF spectra of normal, preneoplastic and neoplastic tissues [2]. As normal cells undergo pathological transformation, distinct changes occur in both the phenotype and genotype of the cells, and intrinsic changes in cellular AF may be indicative of these changes [3].

The intracellular origins of AF in mammalian cells have been postulated to emanate from two main organelles, the mitochondria and the lysosomes [4; 5]. The AF of these two organelles may provide important information about the cell. For example, the mitochondrial AF may indicate the metabolic status, while lysosomal AF may be indicative of the proliferative activity and cell age. Figure 7.1 shows a pseudo colored micrograph of an unstained and unfixed cultured fibroblast taken by a confocal fluorescence microscope (CFM), in which AF structures are colored green against a transmission image of the cell. This is characteristically restricted to small round organelles clustered tightly around the nonfluorescent nucleus [4].
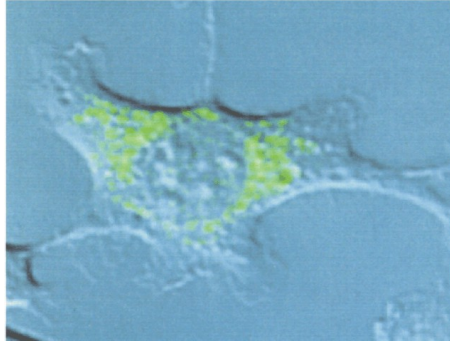
Figure 7.1: *Confocal micrograph of a fibroblast, where the green-colored signal corresponds to AF organelles. Reprinted from [3], with permission.*

Recently, there has been immense interest in the use of microfluidic devices for cell analysis [6; 7; 8]. Microfluidic devices have several advantages compared to conventional systems, such as a very fast heat and mass transfer, small chemical volumes, high electrical fields with low voltages, cells sizes fit very well with microfluidic dimensions (10-100 μm), easy integration of all kinds of analytical operations on a single device, and working with single cells or with large number of cells in parallel. These advantages, combined with the large interest in biochemical experimentation/analysis of living single cells, are compelling for studying microfluidic devices for cell analysis [6].

However, there have been no published reports on cellular AF studies of living cells in such microfluidic systems to date. This chapter demonstrates the potential of using cellular autofluorescence in combination with microfluidic devices for single cell analysis. For example, a microfluidic device that sorts cells (for example normal cells from cancer cells) based on the differences in AF, and for detection of cell lysis or apoptosis. The great advantage with this method is that no labeling with fluorescent probes is required, which will result in reduced sample preparation times. In addition, unlabeled cells avoid potential cell toxicity, proliferation and viability issues that are sometimes associated with fluorescent dyes.

To test the applicability of autofluorescence in combination with microfluidics, preliminary cell differentiating tests have been performed. Several examples of micro-fluorescence-activated cell-sorters (μFACS) have been demonstrated, in which different cell populations are manipulated by either hydrodynamic, electrokinetic, or electroosmotic forces [9; 10; 11] and sorted based on cell-type-specific fluorescent labeling. Microfabricated cell sorting devices offer a number of advantages over conventional FACS, since they are less costly and smaller [9]. In addition, they can preserve the sorted cells in the microdevice by fixation for further investigation.

In this study, a simple microfluidic "three-port"glass microfluidic structure was designed, fabricated and evaluated together using conventional electro-osmotic flow (EOF) to control the sample flow. Human melanoma cells (HTB-67) were first used to verify that the signal-to-noise of the AF signal of individual living cells could be detected by CFM in a microfluidic structure. Thereafter, human blood was used to test the feasibility of AF-based cell differentiation with the microdevice. Using 488 nm wave-

length excitation light, red blood cells have very low AF signal due to the lack of cellular organelles. By contrast, granulocytes contain many autofluorescent mitochondria and thus are highly autofluorescent at this wavelength [3]. This allows these two cell types to be easily differentiated by their AF, and provides a simple means to show the potential use of autofluorescence of single cells in microfluidic devices.
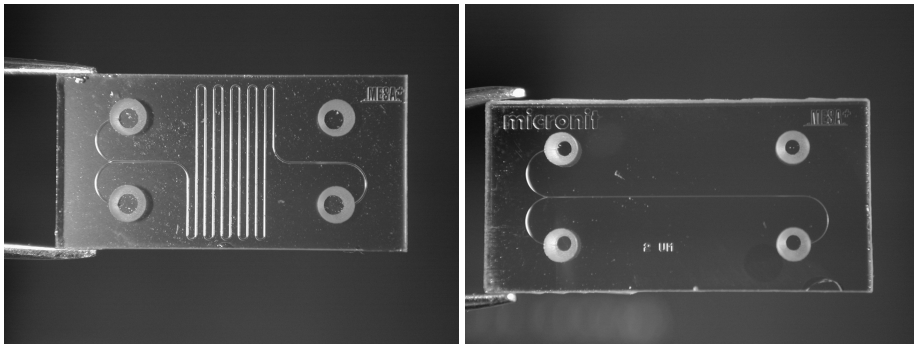
7.2 Materials and methods

7.2.1 Microfluidic chips

Figure 7.2: *Left: photograph of chip 1 showing the inlet on the right and both outlets on the left side of the chip; channel width: 110 µm; channel depth: 50 µm. Right: photograph of chip 2; channel width: 32 µm; channel depth 15 µm.*
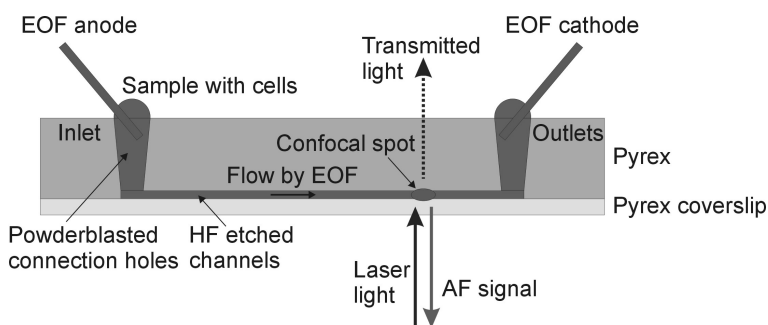
Figure 7.3: *Schematic side view of the detection setup. The confocal detection spot is located just before the channel divides into the two outlets.*

A simple microfluidic three-port glass microstructure was fabricated. The channels were etched with hydrofluoric acid (HF) in Borofloat (Schott, Mainz, Germany) glass substrates. A Pyrex (7740, Corning, New York, NY, USA) cover plate of the chip was back-etched by HF to a thickness of 167 µm. To obtain a low cost sealed connection

between the exterior and the inner channels powder blasting was used to produce the connection holes [12]. Two different microfluidic chips have been used, called Chip1 and Chip2. Chip1 was manufactured in the clean room of the Mesa$^+$ Institute and has channels of 50 μm depth and 110 μm width. Chip2 was manufactured commercially by Micronit (Enschede, The Netherlands) with channels of 15 μm depth and 32 μm width. Figure 7.2 show photos of these devices. No attention should be given to the different shapes of the used channels in Figure 7.2. Figure 7.3 shows a schematic of the experimental set-up.

7.2.2 Cells

In this study, cultured living human melanoma (HTB-67) cells were used to demonstrate the autofluorescence microscopy of single cells in microfluidic devices. In addition, granulocytes and red blood cells (RBCs), separated from fresh whole blood obtained from consenting volunteers and collected using standard methods at the Department of Laboratories, Medical Spectrum Twente Hospital (Enschede, The Netherlands), were used to demonstrate the cell detection and differentiation in the microfluidic device. A mixture of granulocytes and RBCs were isolated from fresh human blood using the Ficoll separation method [13]. Briefly, fresh human blood (25 mL) was diluted in RPMI-1640 medium (Gibco, Canada), supplemented with 2% fetal calf serum (Invitrogen Corporation, Carlsbad, California, USA), 100 IU/ml penicillin (Invitrogen Corporation, Carlsbad, California, USA) and 100 mg/ml streptomycin (Invitrogen Corporation, Carlsbad, California, USA). Ficoll (Amersham Biosciences, Sunnyvale, California, USA) in phosphate buffered saline (PBS) (2.5 mL) was gently added to the cell suspension and, after centrifugation (Allegra 64R, Beckman Coulter Canada Inc, Ontario, Canada) (10,000g for 5 min), granulocytes and RBCs were collected by pipet and re-suspended in PBS before being added to the input chamber of the microfluidic device for CFM imaging. The remainder of the whole blood constituents was discarded. Cells were cultured in a RPMI solution and maintained in a 5% CO_2 humidified atmosphere at 37 °C for less than a week. For CFM imaging, cells were diluted in PBS.

7.2.3 Confocal autofluorescence microscopy

A confocal fluorescence microscope with integrated camera (Zeiss LSM 510, Carl Zeiss, Oberkochen, Germany) was used to collect the cellular AF with a C-Achroplan 63x water immersion objective (N.A. 1.2) (Zeiss, Oberkochen, Germany), The excitation wavelength was 488 nm (power set to 3.0 mW) from an argon laser (LGK 7812 ML4, Lasos Lasertechnik, Jena, Germany) and the AF emission was collected with a long pass 505 nm filter (Zeiss LSM 510, Carl Zeiss, Oberkochen, Germany). AF images (512x512 pixels, 8 bit) were overlaid with light transmission images of the same cells using commercial software (Zeiss LSM 510).

RBCs were distinguished from granulocytes based on differences in AF intensity. These results correlate very well with visual detected RBCs and granulocytes. For all CFM imaging, microfluidic chips were filled with either a cell suspension of HTB-67 cells or the RBC and granulocyte mixture by capillary pressure and the flow rate of the cell suspensions was controlled using EOF. To do this, platinum electrodes were placed in the connection holes connected to an EOF microfluidics apparatus (IBIS μFluidics CU

411, IBIS Technologies, Hengelo, The Netherlands), controlled by a computer using IBIS µFluidics CU 411 software.

To perform high flow speed measurements, pressure-driven flow measurements were performed with a syringe pump (CMA 102, CMA/Microdialisis, Solna, Sweden) containing the cell solution and connected to the chip inlet. The chip outlets were connected to external minivalves (Vici C6W, Valco Instruments, Houston, Texas, USA) to control the direction of fluid flow.

In this study, three different experiments were performed:

1. CFM imaging of free-flowing living HTB-67 cells in Chip1 to demonstrate that AF measurements of single cells,

2. differentiation of granulocytes out of a mixed population of RBCs and granulocytes in Chip1,

3. CFM detection of single granulocytes in the smaller channels of Chip2.

All experiments were performed with the same optical set-up, as shown in Figure 7.4. The AF intensity was measured automatically when cells passed through the optical detection point by the Zeiss LSM software.
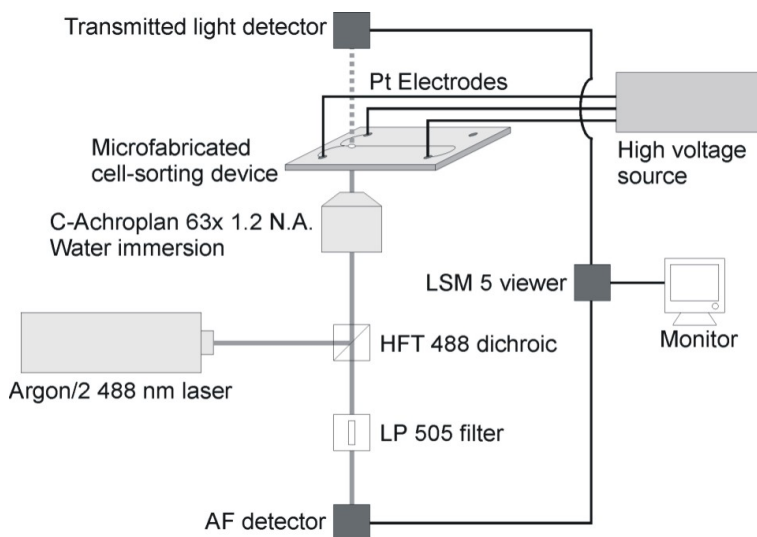

Figure 7.4: *Schematic view of the optical setup.*

7.3   Results and discussion

In the first experiment, using Chip1, Human melanoma cells (HTB-67) were used to verify that adequate the signal-to-noise of cellular AF was possible when imaging single cells in the microfluidic device. Figure 7.5 shows a transmitted light micrograph of a

single free flowing HTB-67 cell in a microfluidic channel, and the corresponding AF micrograph of the same cell, respectively. In Figure 7.6, a higher magnification micrograph of two HTB-67 cells is shown. Similar to the autofluorescent pattern of the fibroblast in Figure 7.1, HTB-67 cells were easily distinguished with their cytoplasmic autofluorescence and non-fluorescent nuclei. To our knowledge, this is the first time that cellular AF is used together with microfluidic structures in order to study living cells.
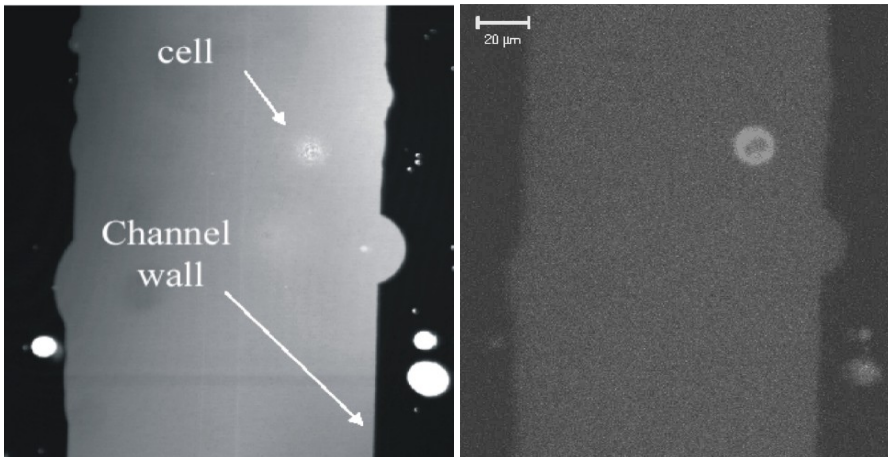
Figure 7.5: Left: photo showing a free-flowing cell in a microfluidic channel. Right: corresponding AF signal of the cell shown in the left photo.
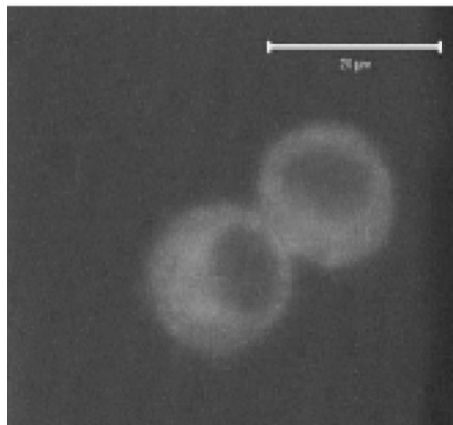
Figure 7.6: Higher magnification of two cells. The AF signal is mainly originating mainly from the cytosol while the nuclei are nonfluorescent.

In the second experiment, with Chip1, shown in Figure 7.7, RBCs had very low autofluorescence signal due to the lack of organelles, whereas granulocytes were highly
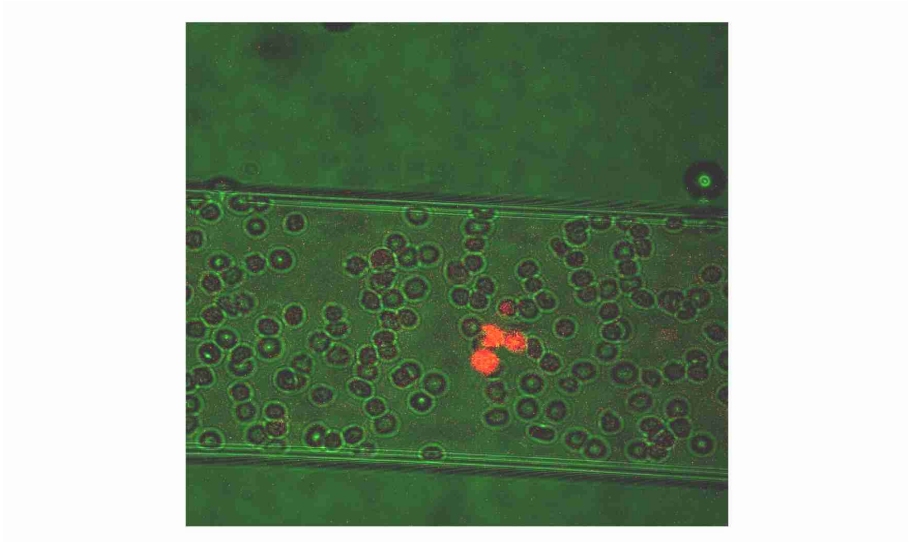
Figure 7.7: *Combined picture from three human granulocytes amongst RBCs. The AF signal (false-colored red) is combined with the transmitted light (false-colored green).*
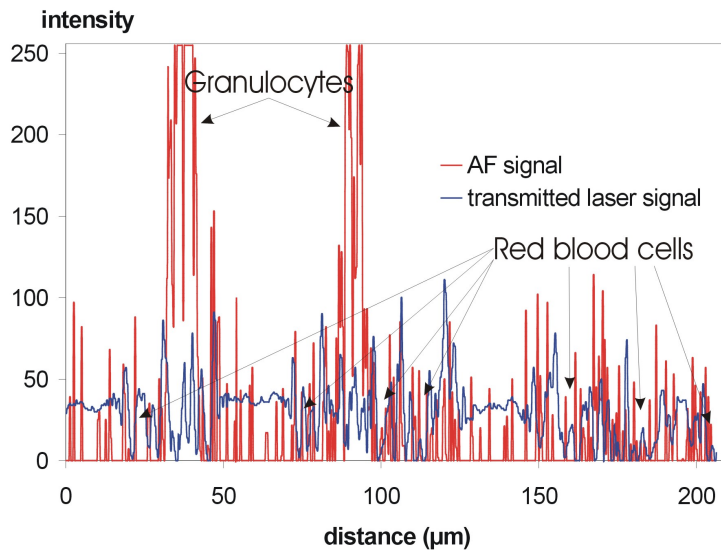

Figure 7.8: *Intensity line scan of the AF signal (> 505 nm) of two granulocytes and several RBCs and the transmitted laser light (=488 nm).*

autofluorescent when excited with 488 nm due to the presence of a large number of mitochondria and lysosomes [14]. This AF difference allowed these two cell types to be easily differentiated. Single granulocytes were successfully detected in a mixture of red and granulocytes in this microfluidic structure. However, the suboptimal imaging quality of the CFM images was a result of the movement of the suspended cells in the flow channel. Line intensity scans of both the AF signal (> 505 nm) and the transmitted light (488 nm) across two granulocytes and several red blood cells are shown in Figure 7.8. Image analysis software was used to determine the AF and transmitted light signals over a single line scan across a distance of 206 μm in the middle of the microfluidic channel along the flow direction. The intensity range was set to 0 – 255 (8bit).

In the scan in Figure 7.8, two granulocytes have a relative high AF signal (255 units) compared to RBCs at a distance of about 40 and 90 μm along the length of the channel. The line scan covers several red blood cells at about approximately 30, 80, 110, 160, 180 and 205 μm positions. These can be seen as the intensity of the transmitted light drops and the fluctuation of the transmitted signal increases. However, the AF signal did not increase and remained at the noise level of about 40 units.

The third experiment demonstrates the use of smaller microfluidic channels as in Chip2. The results are shown in Figure 7.9. To show the advantages of smaller channels in Chip2, Figures 7.9, taken from the third experiment, have been added. In these figures CFM micrographs are shown of individual human granulocytes flowing within the microfluidic channel. Both micrographs are single frames taken 1 sec apart using a time-lapsed measurement. The figures show that less cell-to-cell aggregation took place, as the dimensions of these channels (maximum depth of 15 μm) prevent larger clusters of cells. Only a little cell-to-wall aggregation took place, and the use of biocompatible coating should completely solve this problem. Another advantage of smaller channels is that the size of the detection spot can be decreased, which decreases the risk of having more cells in the detection spot at the same time, and that can increases the efficiency of the detection.

In order for this device to be useful for high-throughput cell-sorting, it is important that the time for detecting single cell AF is fast enough with a sufficient AF signal-to-noise ratio (SNR) is sufficient. The CFM used here performs a single 512x512 pixels scan in 1 sec (4 μs/pixel). Since the single-pixel SNR (20:1) was large enough to detect the AF-signal properly, this implies that a single-pixel detector may be used with a detection time of 4 μs. With equal on-off detection times, this would give us a maximum detection rate of 125 kHz. This short detection time together with a detector size of 10 μm (equal to a moderate cell size) would allow flow rates up to 2.5 m/s. However, this flow rate cannot be realized "on chip"with the devices used due to the microfluidic flow speed limitations. EOF can easily be discarded as being too slow, since it typically permits maximum flow rates up to only several mm/s. Additionally, the large electric fields (> 1 kV/cm) associated with these flow rates can result in cell lysis [11].

By contrast, pressure-driven flow can produce much higher flow speeds, but are associated with high pressures in the channels. These high pressures can result in leakage of the microfluidic devices, or possibly to cell destruction. To achieve a flow speed of 2.5 m/s through a channel with a cross-sectional plane of a half circle, Equation 7.1 shows that a pressure difference (Δp) of 50 bar would be needed to obtain a flow rate of 2.5 mL/s:
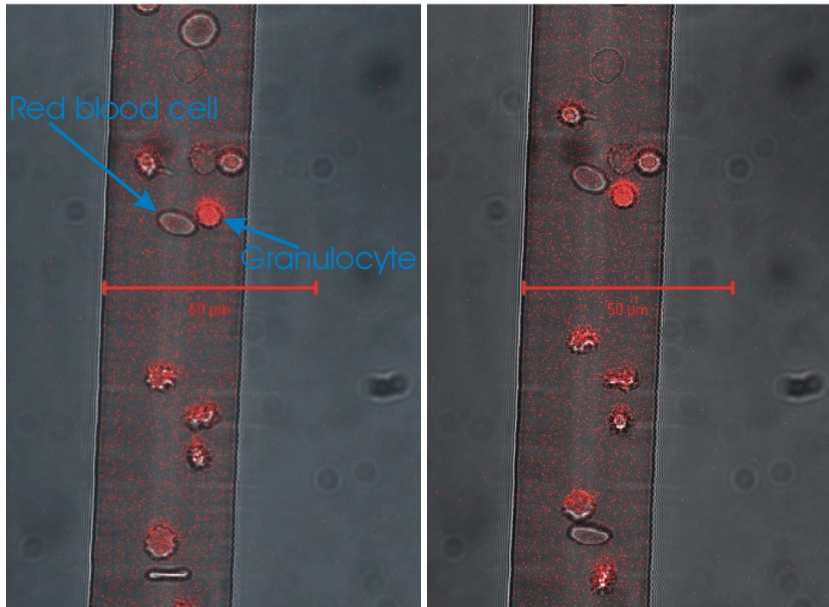
Figure 7.9: *Left: frame picture of free-flowing RBCs (not colored) together with granulocytes (artificially red colored). Right: Next frame picture, taken 1 s later. Note the color difference between the granulocyte and the RBC, indicated by blue the arrows.*

$$\Delta p = \frac{128\mu \cdot L}{3\pi d^4} \cdot \phi \tag{7.1}$$

where $\mu = 1.00 \cdot 10^{-3}$ Pa $\cdot$ s (viscosity of that of water), and L = 2.1 cm (channel length) and d = 15 μm (channel depth) and ϕ = 2.5 m/s (effective flow speed). The constant of 128 is a geometrical constant for a half circular cross-sectional plane [15]. This high pressure-difference is much more than commonly used for microfluidic devices, but with an optimized chip design this value could drop to the more common values of a few bars. The bottleneck will be the valve system. Commercially available external valves from Valco (Valco Instruments, Houston, Texas, USA) give switching times down to 8 ms, limiting sorting frequencies up to 62.5 Hz. Faster valve systems (externally or on-chip) could possibly raise this frequency. For this we conclude that the detection and sorting speeds will be more likely limited by the switching speeds than by the AF detection times. We understand that the maximal frequency of the proposed system with externally connected valves is much lower than the common used frequencies of 300 events per second in classical FACS. Thus, single-pixel AF detection could be a fast detection technique that offers fluorescent label-free sorting of single cells on a chip.

Future studies will include single-cell sorting of normal, pre-cancerous and cancerous cells based on the difference in autofluorescence AF in microfluidic devices. Using

this set-up coupled to an intensity detector an automated system for sorting granulo-cytes from red blood cells will be very easy to obtain. In parallel with the experiments for differentiating cell populations based on their intrinsic autofluorescence we are eval-uating the use of autofluorescence for detection of apoptosis.

7.4 Conclusions

We have demonstrated that two different populations of living cells (i.e., granulocytes and RBCs) can be discriminated from each other based on their autofluorescence char-acteristics using a novel microfluidic device and a confocal fluorescence microscope. This discrimination can be potentially used for cell sorting on chip. Imaging of single cells produced sufficient SNR and fast scan times. In addition, by sorting cells based on their intrinsic fluorescence patterns the use of fluorescent dyes is avoided. This mini-mizes the potential risk of damaging cells due to the affects of fluorescent labels, and reduces the sample preparation time and cost. We conclude that detection and dis-crimination of several cells in a microfluidic device is possible using only the inherent differences in cellular autofluorescence, and that this has a potential for cell sorting and flow-cytometry.

Acknowledgments

Bibliography

[1] A.M.K. Nilson, D. Heinrich, J. Olajos, and S. Andersson-Engels. Near infrared diffuse reflection and laser-induced fluorescence spectroscopy for myocardial tissue characterisation. *Spectrochimica Acta A: Molecular and Biomolecular Spectroscopy*, 53:1901–1912, 1997.

[2] R.S. DaCosta. Master's thesis, University of Toronto, 1999.

[3] R.S. DaCosta, B.C. Wilson, and N.E. Marcon. New optical technologies for earlier endoscopic diagnosis of premalignant gastrointestinal lesions. *Journal of Gastroenterology and Hepatology*, 17:S85–104, 2002.

[4] H. Andersson, T. Baechi, M. Hoechl, and C. Richter. Autofluorescence of living cells. *Journal of Microscopy*, 191:1–7, 1998.

[5] M. Nishimura, J. Ito, and B. Chance. Studies on bacterial photophosphorylation iii. a sensitive and rapid method of determination of photophosphorylation. *Biochimica et Biophysica Acta*, 59:177–182, 1962.

[6] H. Andersson and A. van den Berg. Microfluidic devices for cellomics: a review. 92:315–325, 2003.

[7] P.S. Dittrich and P. Schwille. An integrated microfluidic system for reaction, high-sensitivity detection, and sorting of fluorescent cells and particles. *Analytical Chemistry*, 74:4472–4479, 2002.

[8] S. Gawad, L. Schild, and P. Renaud. Micromachined impedance spectroscopy flow cytometer for cell analysis and particle sizing. *Lab on a Chip*, 1:76–82, 2001.

[9] P. Telleman, U.D. Larsen, J. Philip, G. Blankenstein, and A. Wolff. Cell sorting in microfluidic systems. In *μTAS98 conference proceedings*, pages 39–44, 1998.

[10] A.Y. Fu, C. Spence, A. Scherer, F.H. Arnold, and S.R. Quake. A microfabricated fluorescence-activated cell sorter. *Nature Biotechnology*, 17:1109–1111, 1999.

[11] P.C.H. Li and D.J. Harrison. Transport, manipulation, and reaction of biological cells on-chip using electrokinetic effects. *Analytical Chemistry*, 69:1564–1568, 1997.

[12] H. Wensink and M.C. Elwenspoek. Reduction of sidewall inclination and blast lag of powder blasted channels. *Sensors&Actuators A*, 102:157–164, 2002.

[13] D.T. Harris, M.J. Schumacher, S. Rychlik, A. Booth, A. Acevedo, P. Rubinstein, J. Bard, and E.A. Boyse. Collection, separation and cryopreservation of umbilical cord blood for use in transplantation. *Bone Marrow Transplant*, 13:135, 1994.

[14] B. Alberts, A. Johnson, J. Lewis, M. Raff, K. Roberts, and P. Walter. *Molecular biology of the cell*. Garland Science, fourth edition, 2002.

[15] R.E. Oosterbroek. *Modeling, design and realization of microfluidic components*. PhD thesis, University of Twente, 1999.

Chapter 8

Summary&Outlook

This chapter gives a short summary of the results and conclusions of the preceding chapters. This summation will be completed by reflections given on the future of an integrated micro bi-directional dosing system, and important recommendations to achieve this future prospective.

8.1   Summary

Chapter 2 presented a survey of an integrated micro bi-directional dosing system (IM-BID system). The survey is divided in three parts: the needle, the fluidic network and the pump. Due to the small sizes of a normal mammalian cell, developing such a system gives intriguing challenges, including sub-micron sized hollow needle tips with integrated nanochannels, and highly controllable micropumps capable of dosing volumes in the femtoliter range.

Planar SiN or SiO_2 nanoneedles, integrated with 1d-confined nanochannels, fabricated using surface nanomachining and Cr sacrificial layer technique, are suggested. Surface nanomachining is possible since the encapsulation layers of the nanochannel can be used as needle material when it is shaped with reactive ion etching and silicon underneath is removed using TMAH etching. Since large indentation depths cause high stress in the cell membrane, and therefore it is related to cell viability, these should be avoided. Therefore, design and fabrication of the needle tip is difficult, which has to have dimensions and penetration properties so it penetrates with minimal indentation depth.

Finding an easy integratable and accurate bi-directional micropump system able to dose volume samples lower than 25 fL, is difficult, as no reported micropump system satisfies. Because of requirements dealing with precise control, including closed-loop systems if necessary, good down scaling possibilities and easy integration and fabrication, bubble based electrochemical phase-change micropumping is chosen. Developments in electrochemical micropumping were reviewed, showing combined electrochemical bubble evolution with capillary valve structures is usable to direct flow when the bubble is generated directly inside the nanochannel. Bi-directional pumping in the femtoliter range is expected to be possible.

Chapter 3 described electrolysis and bubble formation in nanochannels, based upon

conventional electrolysis theory valid in bulk dimensions. We showed that nanochannels strongly influence the electrochemical pumping process, especially the growth of bubbles caused by electrolysis. This already starts before electrolysis occurs: the charging of the electrodes. As the electrical currents are very small to generate very small bubble sizes, the charging of the double layers at the electrode surface takes time. Depending on the electrical current and the size of the electrodes the charging time ~1 s. Reducing the parasitic and double layer capacitances will reduce the charging times. Furthermore, produced gases are dissolved and diffuse away from the electrodes into the nanochannel. This slow 1d-diffusion eases bubble nucleation, however, due to the very small gas production rate, the time before bubble nucleation can be in the order of seconds. Also, 1d-diffusion gives good bubble volume stability due to slow diffusion and limited gas/liquid interface.

Bubbles will experience capillary effects in hydrophilic channels due to the small curvature of the bubble meniscus. In contrast with conventional sized channels this can not be neglected, since it easily can be over 10 bar, resulting in decreased bubble volume and higher saturation rates. Liquid drag still had a very small effect on the bubble size, but is increasing exponentially when decreasing channel height.

All these effects influence the electrolysis process and gas bubble behavior in nanochannels, with capillary pressure and 1d-diffusion as prominent effects, causing electrolysis and electrochemical bubble formation in nanochannels to appear very different from the conventional theory. However, more modeling on gas and water diffusion should be performed. Current density at the electrode surface should also be further investigated.

Chapter 4 described the design and fabrication of an IMBID system using conventional micromachining. The IMBID system has been fabricated combining surface nanomachining and silicon bulk wet-etching. Surface nanomachining has been used for the easy integration of the nanochannels, needles and micropump, and it gives the possibility to go to very small dimensions. The micropump in the IMBID system consists of a pair of platinum electrodes for electrochemical actuated hydrogen bubble formation inside a microfluidic network. Hydrogen bubbles evolve at the cathode, placed directly inside a nanochannel, oxygen bubble evolution at the anode is suppressed. An electrical by-pass channel provides electrical current after bubble nucleation. A capillary valve directs the bubble growth towards the hollow nanoneedle, resulting in pumping.

Hollow micro/nanoneedles could be fabricated combining the sacrificial layer technique and PECVD silicon nitride deposition with RIE to structure the planar needles. For fabricating free-hanging planar needles, wet-chemical TMAH etching is used to remove the silicon under the needles. Since the through holes, to contain the cell suspension and for enabling top and down illumination, were etched using this TMAH etching step, the selectivity between the needle material and silicon was tremendously important, low temperature (60°C) and low concentration (10 %) TMAH etching was necessary. Deep reactive ion etching should be considered to etch the bulk material during the through hole fabrication process, and finishing the through hole fabrication with TMAH etching. This reduces the TMAH etching time, and therefore, reduces the impact of TMAH on the needles, enabling thinner needle walls and smaller needle dimensions. This can effentially reduce indentation depth and, therefore, reduce cell mortality.

Chromium appeared to be a very successful sacrificial material for nanochannel fabrication, giving fast etching rates and no attack to the SiN or Pt. Conventionally LPCVD

poly silicon can not be used due to the metal electrode structures. Aluminum has been considered, but due to high viscosity or attacks to the Pt electrodes, it was not useful.

The SiN capping layers appeared to have intrinsic stress, resulting in cracks at places where stress concentrates, i.e. at the ends of the anti-collapse pillars in the anode chamber. Cracks in the capping layer result in incorrect dosing volumes. Low stress silicon nitride has to be considered to avoid this problem.

Platinum is needed for the electrode material, as it gives efficient hydrogen production. Conventional lift-off technique to structure platinum appeared not to be useful due to an effect called 'ears', generating leak currents through the SiN capping layer. Instead, wet-chemical Pt etching is used with oxidized platinum as mask material.

Chapter 5 showed the characterization results of the femtoliter dosing system integrated in the IMBID system. The characterization was divided into characterization of the bubble nucleation, pump rate using continuous dc-current, dosing of discrete volumes using pulsed dc-current, reversed dosing using the electrochemical back-reaction and flow characterization. Main goal was to dose volumes smaller than 25 fL, accurately and repeatable.

The nucleation fits well to the theory. The nucleation position was mainly at the designed position and in most cases the bubble folded nicely around the cathode and stopped at the height step, as designed. The total time needed for nucleation was longer than expected, due to an increase in charging time of the electrical double layers at the electrodes and the parasitic capacity with the silicon substrate. This increase in charging time is assumed to be caused by the increase in solution resistance, due to long ion migration times, and the higher measured capacitance. The nucleation time depends very much on the required level of supersaturation. From the measured nucleation time the calculated supersaturation fitted very well with published data, and therefore the nucleation time fits very well with the theory.

The constant gas evolution experiments showed constant and linear gas volume increases. The measured values for bubble growth rates were approximately 9% lower than the theoretical expected values. Best results were measured with an applied current of 2 nA, where the measured growth rate is 26.8 fL/nC, compared to the theoretical value of 28.8 fL/nC. These small errors are within the expected error range, and therefore the linear bubble growth fits very well with the theory.

The experiments with pulsed currents to dose small volumes is the most important section of this chapter as it shows the possibility of this femtoliter dosing system for dosing very small samples into cells. We have achieved repeatable dosing volumes around 16 fL, so below the limit of 25 fL stated in the goal of this research. Therefore, this important goal has been achieved. Although the dosed volumes are very repeatable, the correlation of the measured dosing volumes with the expected volumes starts at 72% for the 16 fL volumes, but goes down to 40% for volumes just over 80 fL. The reason for this large error is not known.

In order to extract a volume sample from a cell, gas volume reduction is needed. This is achieved by the back-reaction of the electrolysis reaction: the current is reversed and hydrogen and hydroxide react back to water. Free back-reaction, where the electrodes are simply shorted, gave unsatisfactory results due to an inconstant volume reduction rate. Forced back-reaction, where the rate is controlled by an applied reversed current, showed very accurate and linear results. The measured shrinking rates of 15.3 fL/nC correlated with the growth rates of this chip, but not with the theory (28.8 fL/nC)

and the measured growth rates in the dc-measurements (26.8 fL/nC), performed with another chip. It is assumed that these errors are caused by some unknown faults in this chip.

Fluid flow experiments have profen the concept of an electrochemical femtoliter dosing system in nanochannels, where expanding hydrogen bubbles transported other hydrogen bubbles through the channel with a constant distance between the bubbles. The fluid flow through the channels towards the needle exit has been shown and functions even better than theoretically expected. Finally, actual visible dosing from the needle exit has been achieved by dosing a hydrogen bubble of 127 fmol gas into the bulk solution on top of the chip. The measured dosed amount of gas compares very well with the theoretical expected value of 128 fmol. Therefore, we can state that the characterizing experiments achieved very satisfactory results with good theoretical correlation, and the goal of dosing volumes smaller than 25 fL has been achieved with dosing volumes of $\sim$16 fL.

Chapter 6 showed successful cell membrane penetrations using the IMBID-systems nanoneedle. Based on the low indentation depth (below measurement resolution $\sim$1 μm) we do not except severe cell damage. Preliminary results based on optical inspection have not indicated severe cell damage within 30 minutes after penetration. Although cell viability should be thoroughly investigated, based on reported experiments in literature, we expect maintaining cell viability. Nanoneedle integrity was confirmed during all cell penetration experiments. Positioning of a cell at the needle tip remains difficult. Using an external micropipette introduces high risk of cell damage, and therefore decreased viability.

Top-side illumination appears to be insufficient. For proper visibility of cells in direct vicinity of the needle direct pathway of the down-side illumination to the nanoneedle is needed. This was not always the case due to hour-glass shaped through holes, resulting in poor visibility of a penetrated cell, and increased penetration difficulties.

Chapter 7 demonstrated a cell detection principle potentially useful for cell sorting on-chip, and therefore useful for a complete finished IMBID system, containing automated cell detection, sorting and trapping at the needle tips. This detection is able to discriminate two different populations of living cells (i.e., granulocytes and RBCs) based on their autofluorescence characteristics using a novel microfluidic device and a confocal fluorescence microscope. Imaging of single cells produced sufficient SNR and fast scan times. In addition, by sorting cells based on their intrinsic fluorescence patterns, the use of fluorescent dyes is avoided. This minimizes the potential risk of damaging cells due to the affects of fluorescent labels, and reduces the sample preparation time and costs. We conclude that detection and discrimination of several cells in a microfluidic device is possible using only the inherent differences in cellular autofluorescence.

8.2 Outlook

Based on the results shown in this thesis, it can be concluded that an IMBID system might become a very useful tool for studying single cells by performing bi-directional intracellular mass transport. The proposed IMBID system can be improved at several issues, which are discussed below.

Visibility of cells in direct vicinity of the needle may be improved using DRIE for

etching the silicon bulk material during fabrication of the through holes. TMAH etching can be used to finish the through holes, reducing the TMAH etching time. This will solve the problem and reduces the attack to the SiN, which enables to go to smaller dimensions, thus reducing indentation depth during penetration.

The use of optical tweezers may be used to position the cell at the needle tip, being much more gentle to the cell than an external micropipette. In order to achieve the required penetration force, several trapped microbeads will be necessary to push the cell. The accompanying confocal microscopy could be very useful to image the actual penetration characteristics.

Now the limit of the dosed volume was ∼16 fL, and going to smaller volumes is very well possible. The capacitances need to be decreased as they are getting more important due to smaller applied current. Therefore, the areas of the electrode connections (parasitic capacitance) and the anode (double layer capacitance) need to be reduced. An optimized anode still avoids bubble formation, but has minimal double layer capacitance. The channel structure can easily be scaled down to a width of 2—3 μm and a height of <100 nm, resulting in a system that intrinsically can dose volumes of ∼2—3 fL. For increasing the accuracy, a closed-loop system can easily be integrated by using impedance spectroscopy. Only one or several electrodes have to be added in the bubble channel, and with ac-measurements the bubble volume can be estimated.

Such a closed-loop system opens the way to an automated IMBID system. For a successful IMBID system, the detected and sorted cells need to be trapped at the needle tips. Therefore, an extra microfluidic network transporting the cells needs to be integrated. After the detection by autofluorescence the cells can be sorted using electroosmotic flow (EOF) and transported to a cell trap, where the needle tips are located in. In this way, the cell is automatically positioned at the needle tips and now external cell handling system is necessary.

Although it will take some years to present a completely automated and highly functional IMBID system, we expect that these systems will gain significant importance in single cell research. Possible use could be in gene therapy, protein research, drug discovery, and early discovery of cancer cells in the blood stream. In the last possibility, you can think of an implanted automated IMBID system, automatically detecting samples in the blood stream, and alarming when cancer cells have been discovered. Therefore, we think there is a huge future for these new developed IMBID systems.

Appendices

Appendix A

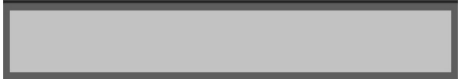# Process Document Femtoliter dosing system

A.1 Masks

All mask layout designs were produced in the CleWin 3.0 software (Wieweb b.v., Hengelo (Ov), The Netherlands). The masks were processed by Delta Mask b.v., Enschede, The Netherlands. All the fabrication has been performed in the MESA$^+$ Cleanroom of the University Twente, Enschede, The Netherlands.
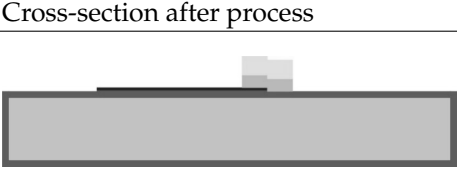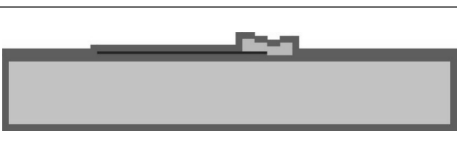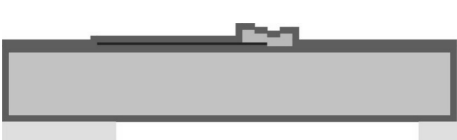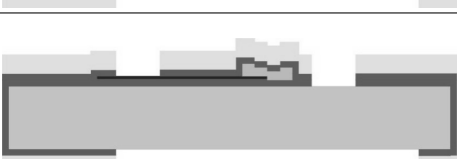
Five masks are needed:

1. ELECTRODE: Electrode structure in platinum, sputtering and wet-etching

2. CHANNEL: Channel structure, sacraficial layer technique with chromium as sacrificial layer

3. HEIGHT STEP: Height step in channels to direct bubble growth, ion beam etching

4. WELL FRONTSIDE: Well openings, needle structure and electrode pad openings, reactive ion etching

5. WELL BACKSIDE: Well openings on backside of the wafer, reactive ion etching

A.2 Process outline

Step	Process	Cross-section after process
1.	Standard cleaning new 4" Silicon wafer, DSP, p-type, <100> orientation	

Step	Process	Cross-section after process
2.	Deposit of 200-500 nm SiN, PECVD, front side Deposit of 500 nm SiN, PECVD, back side	
3.	Sputtering of 10 nm Ti in home-made sputter apparatus	
4.	Sputtering of 40 nm Pt in home-made sputter apparatus	
5.	Patterning of photo resist (Mask 1. ELECTRODE)	
6.	Oxidizing Pt in oxygen plasma	
7.	Resist strip	
8.	Wet etching in Pt-etch	
9.	Measuring electrical surface resistance with 2-point probe to ensure etching is finished	
10.	Sputtering of 160 nm Cr	
11.	Patterning of photo resist (Mask 2. CHANNEL)	
12.	Wet etch Cr	

Step	Process	Cross-section after process
13.	Measuring electrical surface resistance with 2-point probe to ensure etching is finished	
14.	Resist strip	
15.	Patterning of photo resist (Mask 3. HEIGHT STEP)	
16.	Ion beam etching of Cr	
17.	Resist strip	
18.	Deposit of 200-1000 nm SiN, PECVD	
19.	Patterning of photoresist (Mask 5. WELL BACKSIDE)	
20.	Patterning of photoresist (Mask 4. WELL FRONTSIDE)	
21.	RIE of SiN backside	
22.	RIE of SiN frontside	

Step	Process	Cross-section after process
23.	Resist strip	
24.	TMAH etching of through holes and needles	
25.	Dicing of wafers	
26.	Sacrificial layer etching of Cr for creating hollow nanochannels	

A.3   Process parameters

Step	Process	Parameters
1.	Standard cleaning new 4" Silicon wafer, DSP, p-type, <100> orientation	-fuming nitric acid (I), 5 min -fuming nitric acid(II), 5 min -quick dump rinse, DI, <0.1 μS -boiling nitric acid (90 °C), 15 min -quick dump rinse, DI, <0.1 μS -spin drying -store wafers in a cleaned wafer box
2.	Deposit of 200-500 nm SiN, PECVD, front side Deposit of 500 nm SiN, PECVD, back side	Oxford Instruments Plasmalab 80plus -electrode temp.: 400 °C -SiH_4/N_2 flow: 1000 sccm -NH_3 flow: 20sccm -pressure: 650 mTorr -power: 20W LF/HF -deposition rate = 16.7 nm/min -thickness: 200-500 nm -time: 12-30 minutes

Step	Process	Parameters
3.	Sputtering of Ti in Sputterke	Sputterke (home made) -Ti-target -electrode temp.: water-cooled electrode -Ar flow -base pressure: 1.0e-6 mbar -sputter pressure: 6.6e-3 mbar -power: 200 W -deposition rate = 10 nm/min -thickness: 10 nm -time: 1 minute
4.	Sputtering of Pt in Sputterke	Sputterke (home made) -Pt-target -electrode temp.: water-cooled electrode -Ar flow -base pressure: 1.0e-6 mbar -sputter pressure: 6.6e-3 mbar -power: 200 W -deposition rate = 20 nm/min -thickness: 40 nm -time: 2 minutes
5.	Patterning of photo resist (1. ELECTRODE)	Delta 20 -dehydration bake: 120 °C, 10 min. -resist: Olin 907-12, 4000 rpm, 20 sec. -edge beat removal with cotton cud and acetone, 4000 rpm, 20 sec. -prebake: hotplate 95°C, 60 sec. EVG 620 Mask aligner -mask: 1. ELECTRODE -hard/vacuum contact -exposure: 2.8 sec., 12 mW -after exposure bake: 120 °C, 60 sec. -OPD 4262, 60 sec. -quick dump rinse, DI, <0.1 µS -spin drying -visual microscopic inspection
6.	Oxidizing Pt in PT790	Plasmatherm 790 -electrode temp.: 20 °C -O_2 flow: 25 sccm -pressure: 10 mTorr -power: 80 W -time: 2 minutes
7.	Resist strip	HNO_3 (100%) Selectipur: Merck 100453 -beaker: HNO_3 (100%) -quick dump rinse <0.1 µS -spin drying -time: 10 minutes

Step	Process	Parameters
8.	Wet etching in Pt-etch	-H_2O : HCl : HNO_3 = 8 : 7 : 1 -temp.: 90 °C -etchrate: >100 nm/min. -thickness: 40 nm -time: approx. 30 sec. -till colors are bright, not too long, under etch!
9.	Measuring conductance of the surface to ensure etching is finished	Karl Süss probe station and HP 3465A Multimeter -resistance over surface >10MΩ/mm (out of range)
10.	Sputtering of Cr	Sputterke (home made) -Cr-target -electrode temp.: water-cooled electrode -Ar flow -base pressure: 1.0e-6 mbar -sputter pressure: 6.6e-3 mbar -power: 200 W -deposition rate = 13 nm/min -thickness: 169 nm -time: 13 minutes
11.	Patterning of photo resist (2. CHANNEL)	Delta 20 -dehydration bake: 120 °C, 10 min. -resist: Olin 907-12, 4000 rpm, 20 sec. -edge beat removal with cotton cud and acetone, 4000 rpm, 20 sec. -prebake: hotplate 95°C, 60 sec. EVG 620 Mask aligner -mask: 2. CHANNEL -hard/vacuum contact -exposure: 2.8 sec., 12 mW -after exposure bake: 120 °C, 60 sec. -OPD 4262, 60 sec. -quick dump rinse, DI, <0.1 μS -spin drying -visual microscopic inspection
12.	Wet etching in Cr-etch	Chromium etch LSI Selectipur: Merck 111547.2500 -temp.: 55 °C -etchrate: = 100 nm/min. -thickness: 169 nm -time: approx. 1:45 min. -till colors are bright, not longer, under etch!
13.	Measuring conductance of the surface to ensure etching is finished	Karl Süss probe station and HP 3465A Multimeter -resistance over surface >10MΩ/mm (out of range)

Step	Process	Parameters
14.	Resist strip	HNO$_3$ (100%) Selectipur: Merck 100453 -beaker: HNO$_3$ (100%) -quick dump rinse <0.1 µS -spin drying -time: 10 minutes
15.	Patterning of photo resist (3. HEIGHT STEP)	Delta 20 -dehydration bake: 120 °C, 10 min. -resist: Olin 907-17, 4000 rpm, 20 sec. -edge beat removal with cotton cud and acetone, 4000 rpm, 20 sec. -prebake: hotplate 95°C, 60 sec. EVG 620 Mask aligner -mask: 3. HEIGHT STEP -hard/vacuum contact -exposure: 4.2 sec., 12 mW -after exposure bake: 120 °C, 60 sec. -OPD 4262, 60 sec. -quick dump rinse, DI, <0.1 µS -spin drying -visual microscopic inspection -hard bake: 120 °C, 10 min.
16.	Ion beam etching of Cr	Ion beam etcher (home made) -background pressure: 1e-7 mbar -acceleration voltage: 350 V -ion current: 20 mA -ion beam voltage: 500 V -rotation on -ion beam angle: 20° Ar-flow: 300 sccm -etching rate: approx. 2.4 nm/min -thickness: 75 nm -time: approx. 35 min. -etching rate has to be checked in advance!
17.	Resist strip	HNO$_3$ (100%) Selectipur: Merck 100453 -beaker: HNO$_3$ (100%) -quick dump rinse <0.1 µS -spin drying -time: 10 minutes
18.	Deposit of 200-1000 nm SiN, PECVD	Oxford Instruments Plasmalab 80plus -electrode temp.: 300 °C -SiH$_4$/N$_2$ flow: 1000 sccm -NH$_3$ flow: 20sccm -pressure: 650 mTorr -power: 20W LF/HF -deposition rate = 16.7 nm/min -thickness: 200-1000 nm -time: 12-60 minutes

Step	Process	Parameters
19.	Patterning of photo resist (5. WELL BACKSIDE)	Delta 20 -dehydration bake: 120 °C, 10 min. -resist: Olin 907-17, 4000 rpm, 20 sec. -edge beat removal with cotton cud and acetone, 4000 rpm, 20 sec. -prebake: hotplate 95°C, 60 sec. EVG 620 Mask aligner -mask: 5. WELL BACKSIDE -hard contact -exposure: 4.2 sec., 12 mW -after exposure bake: 120 °C, 60 sec. -OPD 4262, 60 sec. -quick dump rinse, DI, <0.1 µS -spin drying -visual microscopic inspection -hard bake: 120 °C, 10 min.
20.	Patterning of photo resist (4. WELL FRONTSIDE)	Delta 20 -dehydration bake: 120 °C, 10 min. -resist: Olin 907-17, 4000 rpm, 20 sec. -edge beat removal with cotton cud and acetone, 4000 rpm, 20 sec. -prebake: hotplate 95°C, 60 sec. EVG 620 Mask aligner -mask: 4. WELL FRONTSIDE -hard contact -exposure: 4.2 sec., 12 mW -after exposure bake: 120 °C, 60 sec. -OPD 4262, 60 sec. -quick dump rinse, DI, <0.1 µS -spin drying -visual microscopic inspection -hard bake: 120 °C, 10 min.
21.	RIE of SiN backside	Plasmatherm 790 -electrode temp.: 20°C -CHF_3 flow: 25 sccm -O_2 flow: 5 sccm -pressure: 20 mTorr -power: 350 W -etch rate: 48 nm/min -thickness: 500 nm -time: 11 minutes

Step	Process	Parameters
22.	RIE of SiN frontside	Plasmatherm 790 -electrode temp.: 20°C -CHF_3 flow: 25 sccm -O_2 flow: 5 sccm -pressure: 20 mTorr -power: 350 W -etch rate: 48 nm/min -thickness: 1500 nm -time: 33 minutes
23.	Resist strip	Plasma System 300-E -50% O_2 -power: 500 W -time: 10 minutes HNO_3 (100%) Selectipur: Merck 100453 -beaker: HNO_3 (100%) -quick dump rinse <0.1 µS -spin drying -time: 10 minutes
24.	TMAH etching of cups and needles	TMAH (25%): Merck 8.14748.1000 -dillute to 10% -temp: 60°C -stirrer -cascade rinse <0.1 µS -no spin drying -etch rate approx. 10 µm/hour -thickness: 2×275 µm (etching from both sides) -time: approx. 28 hours to etch through the wafer
25.	Dicing of wafers	DAD 321 Disco dicing saw -saw disc: NBC-Z -rotation speed: 30.000 rpm -feed: 4 mm/sec. -depth: 550 µm
26.	Sacrificial layer etching of Cr for creating hollow nanochannels	Chromium etch LSI Selctipur: Merck 111547.2500 -etch till channels are open -time: approx. 4 days -put in DI to release etch -time: 4 days

Samenvatting

Hoofdstuk 2 presenteerde een literatuuroverzicht voor het ontwikkelen van een geïntegreerde micro bi-directioneel doseersysteem (IMBID-systeem). Het overzicht is opgedeeld in drie delen: de naald, het fluïdische netwerk en de pomp. Door de zeer kleine afmetingen van een normale zoogdiercel ontstaan intrigerende uitdagingen, zoals holle naaldpunten met sub-micron afmetingen en geïntegreerde nanokanalen en goed bestuurbare micropompen met het vermogen om volumes in het femtoliter gebied te doseren.

Planaire SiN of SiO$_2$ nanonaalden zijn voorgesteld, welke geïntegreerd zijn met 1d-begrensde nanokanalen en gefabriceerd door middel van oppervlakte nanomachinale bewerking en Cr opofferingslaagtechniek. Oppervlakte nanomachinale bewerking is mogelijk aangezien de omhullende lagen van het nanokanaal gebruikt kunnen worden als naaldmateriaal wanneer het gevormd wordt met reactieve ionenets en het silicium onder de naald verwijderd wordt met behulp van TMAH-ets. Aangezien grote inbuigingdieptes veel spanning in de celmembraan veroorzaakt, en daardoor gerelateerd is aan de levensvatbaarheid van de onderzochte cellen, dient deze vermeden te worden. Gevolg hiervan is dat het ontwerp en de fabricage van de naaldpunt wordt bemoeilijkt door de benodigde dimensies om de celmembraaninbuiging tot een minimum te beperken.

Het ontwikkelen van een eenvoudig integreerbare en accurate bi-directioneel micropompsysteem dat volume-eenheden kleiner dan 25 fL dan doseren is lastig, ook aangezien er geen gerapporteerde micropompsystemen zijn die hieraan voldoen. Vanwege de systeemeisen, zoals precieze controle, inclusief terugkoppelingsystemen wanneer nodig, goede mogelijkheden voor verdere miniaturisatie en makkelijke integratie en fabricage, is er gekozen voor op bellen gebaseerde micropompen gebruikmakend van elektrochemische faseverandering. Ontwikkelingen in elektrochemische micropompen zijn onderzocht, wat duidelijk maakte dat gecombineerde elektrochemische belvorming met capillaire klepstructuren bruikbaar is om de vloeistofstroom te sturen wanneer de bel direct in het kanaal wordt gegenereerd. Verwacht wordt dat bi-directioneel pompen in de femtoliterschaal mogelijk is.

Hoofdstuk 3 beschreef elektrolyse en belformatie in nanokanalen, gebaseerd op de gebruikelijke elektrolysetheorie welke geldig is voor bulkdimensies. We lieten zien dat nanokanalen het elektrochemische pompproces sterk beïnvloeden, in het bijzonder de belgroei veroorzaakt door elektrolyse. Dit ontstaat al voordat elektrolyse optreedt: het opladen van de elektrodes. Het opladen van de elektrodes heeft tijd nodig aangezien de elektrische stromen zeer klein zijn aangezien er zeer kleine bellen gegenereerd dienen te worden. Afhankelijk van de elektrische stroom en de grootte van de elektrodes

is de oplaadtijd ~1 s. Het verminderen van de parasitaire en dubbellaagcapacitateiten zal de oplaadtijd verkorten. Daarbij zullen geproduceerde gassen oplossen en van de elektrodes vandaan het nanokanaal in diffunderen. Deze langzame 1d-diffusie vergemakkelijkt de belnucleatie, hoewel door de zeer langzame gasproductie de tijd tot belnucleatie in de ordegrootte van seconden kan zijn. Verder geeft deze 1d-diffusie goede stabiliteit van het belvolume, veroorzaakt door langzame diffusie en beperkt contactoppervlak tussen gas en vloeistof.

Bellen in hydrofiele kanalen zullen capillaire effecten ondervinden veroorzaakt door de kleine kromtestraal van de belmeniscus. In tegenstelling met kanalen met een gebruikelijkere grootte kunnen deze effecten niet verwaarloosd worden aangezien het gemakkelijke een druk van meer dan 10 bar kan bereiken, wat resulteert in verkleinde belvolumes en hogere verzadigingswaardes. Stromingsweerstand had nog een zeer kleine invloed op de belgrootte, maar deze invloed zal exponentieel toenemen wanneer de kanaalhoogte verminderd wordt.

Al deze effecten beïnvloeden het elektrolyseproces en het gedrag van de gasbellen in nanokanalen, met capillaire druk en 1d-diffusie als prominente effecten, wat ervoor zorgt dat elektrolyse en elektrochemische belformatie in nanokanalen zich zeer anders gedraagt dan volgens de conventionele theorie. Echter, meer modelleerwerk van gas- en waterdiffusie dient uitgevoerd te worden. Ook dient de stroomdichtheid aan het elektrodeoppervlak verder onderzocht te worden.

Hoofdstuk 4 beschreef het ontwerp en fabricage van een IMBID-systeem gebruikmakend van conventionele micromachinale bewerking. Het IMBID-systeem is gefabriceerd met oppervlakte nanomachinale bewerking gecombineerd met het nat-etsen van silicium bulk. Oppervlakte nanomachinale bewerking is gebruikt voor de eenvoudige integratie van nanokanalen, naalden en micropomp, en het geeft de mogelijkheid van om tot zeer kleine dimensies te gaan. De micropomp in het IMBID-systeem bestaat uit een platina elektrodepaar voor elektrochemische actuatie van waterstofbellen binnenin een microfluïdisch netwerk. Waterstofbellen ontstaan aan de kathode, direct geplaatst binnenin een nanokanaal; het ontstaan van zuurstofbellen aan de anode wordt onderdrukt. Een elektrisch omleidingkanaal voorziet in de elektrische stroom na de belformatie. Een capillaire klep stuurt de belgroei in de richting van de holle nanonaald, resulterend in pompwerking.

Holle micro/nanonaalden konden gefabriceerd worden door middel van de opofferingslaagtechniek en PECVD (druk verbeterende chemische damp depositie) siliciumnitride depositie gecombineerd met RIE (reactief ion-etsen) om de naalden te vormen. Voor de fabricage van vrijhangende planaire naalden is natchemisch TMAH etsen gebruikt om het silicium onder de naalden te verwijderen. Aangezien de gaten door de wafer, om de celoplossing te bevatten en om boven- en onderbelichting mogelijk te maken, geëtst zijn met behulp van deze TMAH etsstap, is de selectiviteit tussen het naaldmateriaal en het silicium extreem belangrijk, waardoor lage temperaturen (60°C) en lage concentratie (10%) voor het TMAH-etsen noodzakelijk waren. Voor het etsen van de doorgaten dient diep reactief ion-etsen (DRIE) overwogen te worden voor het etsen van het bulkmateriaal alvorens het etsen van de doorgaten afgerond wordt met TMAH-etsen. Dit zal de TMAH-etstijd verminderen, en daardoor ook de impact van de TMAH op de naaldstructuren, waardoor dunnere wanddiktes en kleinere naaldafmetingen mogelijk worden. Dit zal dan uiteindelijk de inbuigingdieptes verminderen, en daarmee de celsterfte verkleinen.

Door de hoge etssnelheden van chroom en de doordat chroomets niet agressief is voor SiN en Pt bleek chroom een erg succesvol opofferingsmateriaal te zijn voor de fabricage van nanokanalen. Polysilicium kon niet als opofferingsmateriaal gebuikt worden aangezien LPCVD (lage druk chemische damp depositie) niet toegepast kan worden vanwege de aanwezigheid van metalen elektrode structuren. Aluminium is ook overwogen, maar door de hoge viscositeit of agressiviteit van de ets ten opzichte van Pt was dit niet succesvol.

De SiN afdichtingslagen bleken over veel inwendige spanningen te beschikken, wat resulteerde in barsten waar deze spanning zich concentreerde, d.w.z. bij de uiteinden van de verstevigingschotten in the anodekamer. Barsten in de afdichtingslagen resulteert in foutieve doseervolumes. De toepassing van lage-spanning siliciumnitride moet overwogen worden om dit probleem op te lossen.

Platina is nodig als elektrodemateriaal, aangezien het een efficiënte waterstofproductie geeft. Gebruikelijke oplichttechnieken ("lift-off") voor de platina structurering bleek niet geschikt aangezien een effect bekend als 'oortjes' optrad, resulterend in lekstromen door de SiN afdichtinglaag. In de plaats hiervan is natchemisch Pt-etsen gebruikt, met geoxideerd platina als maskermateriaal.

Hoofdstuk 5 presenteerde de karakterisatieresultaten van het femtoliter doseersysteem geïntegreerd in het IMBID-systeem. De karakterisatie was opgedeeld in de karakterisatie van de belnucleatie, de pompsnelheid d.m.v. een continue gelijkstroom, dosering van discrete volume-eenheden d.m.v. gepulseerde gelijkstromen, omgekeerde dosering d.m.v. elektrochemische terugreactie en karakterisatie van de vloeistofstroom. Belangrijkste doelstelling was om doseervolumes kleiner dan 25 fL te bereiken, accuraat en reproduceerbaar.

De nucleatie sluit goed aan bij de theorie. De nucleatie ontstond voornamelijk op de ontworpen positie en in de meeste gevallen vouwde de bel zich netjes rond the kathode en stopte tegen de hoogtestap, zoals ontworpen. De totale tijd tot nucleatie was langer dan verwacht, veroorzaakt door een toename van de oplaadtijd van de elektrische dubbellagen aan de elektrodes en de parasitaire capaciteit met het silicium substraat. We veronderstellen dat deze toename van de oplaadtijd veroorzaakt wordt door de toename van de elektrische weerstand van de oplossing ten gevolge van de lange ionmigratietijden en door de hogere gemeten capaciteit. De nucleatietijd hangt erg af van de vereiste supersaturatienivo. De, uit de gemeten nucleatietijd berekende, supersaturatie kwam zeer goed overeen met gepubliceerde data, en zodoende sluit de nucleatietijd erg goed aan bij de theorie.

De experimenten waarbij constant gas ontwikkeld werd gaven een constante en lineaire toename van het gasvolume. De gemeten waarden van de toename van het belvolume lagen ongeveer 9% onder de theoretische verwachtingen. De beste resultaten werden behaald met een toegevoerde stroom van 2 nA, waarbij de gemeten belgroei 26.8 fL/nC bedroeg, dit in vergelijking met de theoretische waarde van 28.8 fL/nC. Deze kleine afwijkingen liggen binnen de verwachte foutmarge, waardoor de lineaire belgroei zodoende zeer goed aansluit met de theorie.

De experimenten met de gepulseerde stromen om kleine volumes te doseren zijn de belangrijkste van dit hoofdstuk, aangezien deze de mogelijkheid van het femtoliter doseersysteem aantonen om zeer kleine volume-eenheden in cellen te injecteren. We hebben reproduceerbare doseervolumes van ongeveer 16 fL bereikt, dus onder de limiet van 25 fL zoals dat is opgesteld in het doel van het onderzoek, zodoende is deze

belangrijke doelstelling ook bereikt. Hoewel de gedoseerde volumes erg reproduceerbaar zijn ligt de correlatie tussen de gemeten doseervolumes met de verwachte volumes lager, beginnend bij 72% voor volumes van 16 fL en afdalend tot 40% voor volumes van iets meer dan 80 fL. De reden voor deze grote afwijking is onbekend.

Om volume-extracties uit een cel uit te kunnen voeren is verkleining van het gasvolume nodig. Dit wordt bereikt door de terugreactie van de elektrolysereactie: de elektrische stroom wordt omgedraaid en waterstof en zuurstof reageren terug naar water. Vrije terugreactie, waarbij de elektrodes simpelweg kortgesloten worden, gaf onbevredigende resultaten veroorzaakt door een niet-constante volumevermindering. Gedwongen terugreactie, waarbij de snelheid bepaald wordt door een omgekeerde toegevoerde elektrische stroom gaf wel zeer nauwkeurige en lineaire resultaten. De gemeten krimpsnelheden van 15.3 fL/nC correleerde met de groeisnelheden van deze chip, maar niet met de theorie (28.8 fL/nC) en gemeten groeisnelheden in de constante gelijkstroommetingen (26.8 fL/nC), welke uitgevoerd waren met een andere chip. We veronderstellen dat deze afwijkingen veroorzaakt worden door enkele onbekende fouten in de gebruikte chip.

Vloeistofstroomexperimenten hebben het concept van een elektrochemisch femtoliter doseersysteem in nanochannels bewezen, waarbij expanderende waterstofbellen andere waterstofbellen door het kanaal transporteerden met gelijkblijvende afstand tussen de bellen. De vloeistofstroom door de kanalen naar de naalduitgang is gevisualiseerd en was zelfs beter dan volgens de theorie verwacht werd. Als laatste is de werkelijke dosering vanuit de naaldtip aangetoond door een waterstofbel van 127 fmol gas in de bulkoplossing bovenop de chip te doseren. De gemeten hoeveelheid gas kwam zeer goed overeen met de theoretische verwachte hoeveelheid van 128 fmol. Zodoende kunnen we stellen dat karakterisatie-experimenten zeer bevredigende resultaten bereikte met goede correlatie met de theorie, en de doelstelling van doseervolumes kleiner dan 25 fL behaald is met doseervolumes van ~16 fL.

Hoofdstuk 6 liet succesvolle celmembraanpenetraties zijn gebruikmakend van de nanonaald van het IMBID-systeem. Gebaseerd op de kleine inbuigingdiepte (kleiner dan de meetresolutie van ~1 μm) verwachten we geen ernstige schade aan de cellen. Vroegtijdige resultaten, gebaseerd op optische inspectie, hebben geen aanwijzingen opgeleverd voor ernstige schade aan de cellen binnen 30 minuten na penetratie. Hoewel de levensvatbaarheid van de cellen grondig onderzocht dient te worden, verwachten we, gebaseerd op gerapporteerde experimenten in de literatuur, handhaving van de levensvatbaarheid van de cellen. Tijdens alle experimenten werd de naaldsterkte bevestigd. De plaatsing van cellen op de naaldpunt bleef zeer lastig. Het gebruik van een externe micropipet gaat gepaard met een hoog risico van schade aan de cellen, en zodoende met een verminderde levensvatbaarheid.

Bovenverlichting bleek onvoldoende te zijn; voor een goede zichtbaarheid van de cellen in de directe nabijheid van de naald is directe lichtinval vanaf de onderkant nodig. Dit was echter niet altijd het geval vanwege het zandlopermodel van de doorgaten, wat resulteerde in een slechte zichtbaarheid van een gepenetreerde cel en zodoende de penetraties bemoeilijkte.

Hoofdstuk 7 demonstreerde een principe voor celdetectie die potentieel bruikbaar is voor celsortering op-chip, en zodoende bruikbaar is voor een totaal afgerond IMBID-systeem, welke cellen automatisch detecteert, sorteert en inklemt aan de naaldpunt. Deze detectie kan twee verschillende populaties van leven cellen van elkaar onderschei-

den (te weten: granulocyten en rode bloedcellen), gebaseerd op de hun autofluorescentie karakteristieken, gebruikmakend van een nieuwe microfluïdische chip en een confocale fluorescentiemicroscoop. Het in beeld brengen van enkele-cellen produceerde voldoende SNR (signaal-ruis verhouding) en snelle scantijden. In aanvulling hierop kan gesteld worden dat door het sorteren van cellen gebaseerd op hun eigen fluorescentiepatronen het gebruik van fluorescente labels vermeden wordt. Dit vermindert het potentiële gevaar van celschade door de invloed van de fluorescente labels, en vermindert de celpreparatietijd en -kosten. We concluderen dat de detectie en discriminatie van verschillende cellen in een microfluïdische chip mogelijk is waarbij enkel gebruik gemaakt wordt van de inherente verschillen in cellulaire autofluorescentie.

Dankwoord

Ben je vier jaar aan het ploeteren, zuchten en kreunen en heb je na zeer veel moeite eindelijk je boekje af, en wat doen al je collega's als eerste? Juist ja, het hele boekje links laten liggen en gelijk naar het dankwoord toe om te kijken of zij ook wel genoemd zijn. Inderdaad, van het hele boekje waar je jaren aan gewerkt hebt is het dankwoord, dat stukje dat je als allerlaatste even in elkaar draait en wat totaal geen enkele wetenschappelijke betekenis heeft, het enige dat ertoe doet...

Mijn ouders hebben me altijd in mijn beslissingen gesteund, de juiste dan wel niet de juiste, van fouten leer je. Maar altijd waren ze daar als het dan soms toch even wat minder goed ging, zoals ook afgelopen jaar, toen ik toch een beetje in de put zat. De resultaten kwamen maar niet en de tijd begon te dringen. Stress kwam om de hoek kijken. Toch hebben ze me weer rustig gekregen en aangespoord om vooral door te gaan. En het resultaat mag er zijn: dus pap&mam: bedankt! Ook Marijke, Henk, Steven en Karina bleven altijd geïnteresseerd in wat ik aan het doen was, al was ik daar niet altijd even duidelijk over, jullie ook daarvoor bedankt! En met dit boekje wordt het wellicht nog een stuk duidelijker. Caya&Isis, jullie hebben er nu nog geen benul van wat ik aan het doen was, maar als jullie dit boekje in, pak 'm beet, 2025 nog 's van het stof ontdoen wordt het misschien wel wat duidelijker. In ieder geval bedankt dat jullie er zijn! Verder nog een speciaal bedankje aan Steven en Karina: bedankt voor de kaft! Hij ziet er weer gelikt uit!

Mijn nieuwe schoonfamilie, Jan&Betty, Ineke&Erik, Ido, Wiebe&Charlotte, Jelle&Gonnie, jullie natuurlijk ook bedankt voor jullie gezelligheid en interesse in mijn bestaan in die verre uithoek: Tukkerland. Ik hoop dat jullie na deze verdediging, en het na het minutieus bestuderen van dit boekje, wat beter weten wat ik nou aan het doen was.

Ik zal nu de mensen bedanken a.d.h.v. een chronologisch schrijven. Zo komen jullie ook nog een beetje beter te weten hoe ik tot dit boekje gekomen ben.

Op de HTS kreeg ik een afstudeeropdracht onder mijn neus geschoven, op de UT, bij ene promovendus genaamd Sebastiaan Böhm, promoverend bij leerstoel Bios (Biosensoren) van Piet Bergveld. Bij gebrek aan UT-afstudeerstudenten was Sebastiaan maar uitgeweken naar de HTS. Het leek me wel wat, een beetje knutselen aan elektrochemische micropompen op-chip. Door Sebastiaan ben ik dus een beetje in dit gebied gerold, en hij heeft mij de eerste beginselen van onderzoek bijgebracht, al was hij meer een vlotte 'autoverkoper' dan verstrooide wetenschapper. Sebastiaan, mocht je dit ooit nog 's lezen: bedankt voor het starten van m'n wetenschappelijke carrière.

Ik vond dat afstuderen op die kleine pompjes best interessant, maar ondanks een verzoek van Piet Bergveld om AIO bij hem te worden, heb ik toen toch maar voor gekozen om de IT-wereld in te duiken. Na verloop van tijd bleek dat toch veel te saai, en ik wou weer leuke, interessante, natuurkundige dingen doen. Na allerlei vacatures en sollicitaties, o.a. bij ESRF (European Synchrotron Radiation Facility) in Grenoble, bleek toch eigenlijk dat promoveren de beste optie was. Met een doctortitel op zak zou ik wel de banen kunnen doen die me het interessants leken: research&development onderzoeker in het bedrijfsleven. Personen die er wezenlijk aan bijgedragen hebben om mij die keuze te laten maken waren mijn 'zusje' Tamara en Mark. Mark&Suske, tige dank foar hjim harkjen, hjimme ried en hjim fertrouwen wat hjim my jûn hawwe!

Terug naar Bios om te vragen of ze daar nog wat leuks hadden. Wouter Olthuis, de rechterhand van Piet Bergveld, had niets, behalve raad om het niet te doen als je niet echt de wetenschap in wou. Als je het puur zou doen als investering voor later, dan zou het niet lukken. Eigenwijs als ik was heb ik het toch maar doorgedrukt, maar toch bedankt voor deze wijze raad. ;-)

Albert van den Berg, hoogleraar bij TST (Transducers&Sensor Technology), maar nog zonder eigen leerstoel, zag wel wat in me. Maar eerst wel even bewijzen, ik was per slot van rekening een softwareschrijvende HTS'er, dus ik kreeg een jaarcontract als technoloog. Na het pensioen van Piet Bergveld volgde Albert hem op als nieuwe leerstoelhouder van Bios, en kwam ik dus toevallig weer terecht bij Bios; het cirkeltje was weer rond. Albert zag me gelukkig wel zitten als AIO en bood me een promotieplaats aan, waarvoor natuurlijk bijzondere dank. Albert, zonder jouw creatieve inbreng, enthousiasme voor het project en scherpe ingevingen was het wellicht helemaal anders gelopen. Ik ben je daarvoor veel dank verschuldigd, al moet ik eerlijkheidswegen ook wel zeggen dat je me soms helemaal tot wanhoop hebt gedreven. Zoals die ene keer dat ik na een overleg met 6 (zes!) verschillende EERSTE PRIORITEITEN de deur uitliep...

Goed, ik dus weer bij Bios aan de slag. Onvoorstelbaar hoe snel zo'n periode van 5 jaar voorbij vliegt, en hoeveel er wel niet gebeurt in zo'n tijd. Natuurlijk met het onderzoek, maar ook met alle mensen die de revue passeren. Ondoenlijk om ze allemaal op te noemen, maar laat ik de belangrijkste toch maar niet vergeten. Mensen, die om wat voor reden, toch aan je ontwikkeling als assistent-in-opleiding hebben bijgedragen.

Naast Albert heb ik verschillende begeleiders gehad, zoveel zelfs dat ik zelf de draad ook een beetje kwijtgeraakt ben. In het begin was daar Albert zelf, maar dat bleek niet haalbaar. Daarna Helene Andersson, een nieuwe parttime postdoc in de groep, maar woonachtig in Stockholm, dit bleek ook niet echt handig. Vervolgens Niels Tas, maar hij ging terug naar z'n oude stek bij TST, wat ook niet echt bevorderlijk was voor de samenwerking. Niels, hoewel onze samenwerking kort was, wil ik je wel bedanken voor de inzichten die je me gegeven hebt en de discussies die we gevoerd hebben. Als vierde persoon was daar Henk Wensink. Henk, bedankt voor je wijze raad en je niet aflatende enthousiasme voor mijn werk! Maar Henk bleef helaas niet erg lang, hij vertrok naar het bedrijfsleven. Han Gardeniers was de volgende in rij, en hij heeft me het langst bijgestaan, tot zijn vertrek als professor van zijn eigen leerstoel. Nog gefeliciteerd, Han! Jij hebt altijd erg goed naar me willen luisteren, en gestuurd waar dat nodig was. Jouw rust heeft me zeker goed gedaan! En dan de laatste, nummer zes: Edwin Carlen. Het meeste wetenschappelijke werk zat er al op toen jij kwam, maar je bijdrage aan dit boek is zeker groot geweest. Herhaaldelijke urenlange, boeiende discussies heb ik met jou gevoerd, waardoor ik 's avonds laat die verloren uren weer in kon halen met

het schrijven... ;-) Ontzettend bedankt voor jouw inzet!

Naast begeleiding krijg je natuurlijk ook ondersteuning in je werkzaamheden. Jan, Daniël en het voltallige cleanroompersoneel, bedankt voor jullie cleanroomondersteuning. Hermine en Ida, bedankt voor het secretariële werk. En Edwin, Willem, Niels en Albert, bedankt voor de wetenschappelijke discussies. Robert-Jan, Foppe en Ramona, jullie bedankt voor de bijdragen als (afstudeer)studenten aan mijn onderzoek.

In de groep ben je natuurlijk niet alleen, gelukkig niet. Gezelligheid alom! Op de tiende was het vaak keten, tot grote frustraties van de andere, wat saaiere, bewoners van die vloer. Met Ana-chica, Egbertina, Floortje (en toch was zij vaker in het ziekenhuis te vinden dan op deze gezellige verdieping) op 1 kamer, de hele periode bij elkaar gebleven! Was altijd erg gezellig, al kon dat wel op je zenuwen werken als er een boekje afgemaakt moest worden. Bijzondere dank voor jullie hoge acceptatieniveau van mijn, soms enigszins aparte, muzieksmaak en mijn keiharde gerammel op het toetsenbord! :-) Floor, jij ook nog bedankt voor het willen vervullen van je zware paranimfentaak. Naast deze gezellige kamergenoten liepen er nog veel meer gezellige mafketels rond op de 10e: Roald (Frits), Patrick, Theo, Henk (Fluffy), Paul (Polletje), Wouter, Steven (met wie je heerlijk maden kunt eten!), Arjan, Wim, Wojtek, Anil, Jacob, Vincent (Kale), Han en Regina. Het was wel duidelijk, dit was de gezellige dependance van Bios, waar een beetje uit het zicht van de grote baas veel malligheid heerste!

Wat meer in het zicht van de grote baas leek de sfeer toch wat serieuzer. Maar de koffiehoek, of het rondje naar de Casper, met Iris, Erika, Polletje, Ana, Roald, Eggiebertie, Erik, Doro, EdwinO, Sebassie, Doro, Wim, Vincent, Céline, Ad, Wouter (bedankt voor de leuke politieke discussies), Wouter, Jan, Jan, Albert, Hermine, Ida, Daniël, Johan, Steven, Arjan, Séverine, Svetlana, Edwin en Ton waren dan natuurlijk weer welkome afwisselingen. En nog wat verder uit beeld droegen Sebassie, Erika, Annet, Doro en Wim natuurlijk ook weer bij aan de feestvreugde tijdens de borrels en filmavondjes in de VB.

Mijn oud-huisgenoten horen hier natuurlijk ook bij te staan: Alessio, Willem en Wim. Jongens, jullie ook bedankt voor het doen van mijn afwas! ;-) Andere mensen die hier thuis horen zijn EdwinO, Pino&Ilona, Willem en Marko vanwege de vele leuke en gezellige etentjes in mijn begintijd.

In de begintijd is er veel overleg en prettige samenwerking geweest met het LACDR/Universiteit Leiden, en met name met Ubbo en Willem. Willem, jij ook bedankt voor de gezellige avondjes! En natuurlijk bedankt dat je paranimf wilt zijn! Trouwens, binnenkort moet je me toch echt maar 's zwoel leren dansen...

Naast de mensen die direct met je werk te maken hebben zijn er nog stapels mensen die gelukkig alleen maar onder de informele sfeer vallen. Agnes en Paidor bijvoorbeeld, omdat jullie precies wisten hoe ik me soms voelde. En dan konden we de ellende met Spaanse wijn (niet bij de Edah?!) weer wegdrinken. Of van de gekken van de MSG zoals Dimitri en Jos, gezellig samenzijn en over motoren lullen, danwel een fijn stukkie trialen/raggen/racen/toeren/tuffen[1]. Sorry jongens, ik ga geen namen[2] meer noemen, mijn tekstruimte was gelimiteerd. En voor de echte sportieve activiteiten kon ik natuurlijk altijd bij Kronos terecht. Om er dan weer achter te komen dat mijn conditie

---

[1]doorhalen wat niet van toepassing is

[2]o.a. Jos, Daniël, Tamara, Albert, Dimitri, Saara-Maarit, Dirk, Jelle, Roger, Anne-Freerk, Ineke, Arvid, Liesbeth, Simon, Vincent, Erik, Robert, Remco, Remko, Frank, Ivo, Arne, Baveld, Vincent, Niels, Ite-Jan, Wel, Arthur, Roel

alweer slechter geworden was. Kronauten[3] zoals Brenda en Agnes, en in het speciaal de meerkampers, jullie ook bedankt voor de gezellige en sportieve afwisseling en de geslaagde wedstrijdjes!

De vrienden van voor mijn AIO-tijd, danwel nieuwe mensen die ik heb leren kennen buiten dit werk om, hebben dan wellicht niet zo veel bijgedragen aan de ontwikkeling of het welzijn in Enschede, ze zijn zeker niet minder belangrijk geweest! Echter, omdat dit boekje toch het hoofdstuk Enschede voor mij zal afsluiten, houdt ik dit dankwoord toch een beetje hierop gericht. Niet dat ik jullie tekort wil doen, maar onze vriendschap zal zeker nog wel langer duren. Ondanks dat ik de laatste tijd wat minder van me hebt laten horen, gaat dat dus weer helemaal goedkomen! We spreken snel weer 's af en an halen we de kano uit 't vet, rollen de motor weer de straat op, pakken een biertje in de kroeg, openen een flesje wijn, hijsen de zeilen, prikken een vorkje of doen gewoon niks. :-)

En heb ik nou niemand meer vergeten? Toch wel! Marieke, maar jij weet best dat ik jou nooit zou vergeten! Ontzettend bedankt voor je liefde, steun en vertrouwen die je me gegeven hebt! En straks kunnen we heel wat vaker samen zijn, dan gaan we ergens samen een huisje betrekken. Ik hâld fan dij, myn leafste.

Lang geleden heb ik in een soort van jeugdige overmoed en naïviteit ooit 's tegen mijn moeder gezegd dat ik wel sneller klaar zou zijn met de universitaire studie dan zij... Zij was toen namelijk net begonnen aan de Open Universiteit en ik zat ergens in de onderbouw van de middelbare school. Tot op de dag vandaag moet ik mijn opmerking nog lijdzaam ondergaan: zij is, als ik het goed heb, in 1995 geslaagd, en ik? Ach, ik hoop dat ik het, weliswaar 12 jaar later, hiermee weer een beetje rechtgezet heb.

Jurjen

---

[3]o.a. Agnes, Ruben, Brenda, Bas, Stijn, René, Trienke, Ronald, Arco, Fredo, Sjoerd, Daniël, Erik, Ewoud, Harmen, Jeroen, Jurgen, Karin, Kirsten, Bianca, Fabian, Maarten, Lourens, Marcel, Rink, Rinke, Monique, Nadia, Carolien, Nelleke, Nienke, Steven, Tom, Annelies en Wout